UCL Université catholique de Louvain

École polytechnique de Louvain (EPL)

# Magnetic and magneto-transport properties of 3D interconnected networks of Ni/Cu and NiCo/Cu multilayered nanowires

Dissertation presented by
**Kyara HALLET**

for obtaining the Master's degree in
**Chemical and Materials Engineering**

Supervisor(s)
**Luc PIRAUX**

Reader(s)
**Benoît HACKENS, Yenni GUADALUPE VELAZQUEZ GALVAN**

Academic year 2017-2018

# Abstract

Since the discovery of the giant magnetoresistance in multilayered thin films, this effect has been extensively studied by the scientific community in other multilayered nanostructures, such as parallel nanowire networks made of iron, nickel, cobalt or their alloys. The advantage of these structures is the possibility to tune their porosity and pore diameter. Recently, interconnected nanowire arrays have generated interest because they are self-standing and their transport properties can easily be measured. In addition, these systems are more isotropic than parallel nanowire networks and therefore increase the GMR ratio.

The objective of this Master's thesis is to investigate the magnetic and magneto-transport properties of 3D interconnected networks of multilayered nanowires. The template-assisted electrodeposition in a single electrolyte bath has been used to grow the multilayered nanowires in track-etched polycarbonate membranes, covered on one side by a metallic cathode. Ni/Cu and NiCo/Cu multilayers with different atomic percentages of Co have been examined. Additionnaly, the pH was fixed to a value of 2 to avoid any magnetocrystalline contribution. Their morphology and composition have been characterised by scanning electron microscopy (SEM) and energy dispersive X-ray spectroscopy (EDX). The magnetic properties of these multilayered structures have been measured using an alternating gradient magnetometer (AGM) and the magneto-transport properties have been assessed at room temperature and at 12 K.

By adjusting the electrodeposition conditions, the difficulty to form Ni/Cu multilayers due to phase separation has been highlighted. Thinner magnetic layers have shown to decrease the anisotropy of the system whereas the impact was lower when changing the thickness of the non-magnetic layers. A GMR ratio of 2% has been obtained on a low porosity template at low temperature. Studying the evolution of the addition of Co in the magnetic layers revealed a stabilisation of the Ni and the formation of multilayers. The positive effect of reducing the amount of crossing zones by using lower porosity templates and increasing the Co content on the GMR has been demonstrated. A more isotropic behaviour coupled with higher GMR has been shown when adjusting the size of the multilayers. 44% and 19% of GMR were found at low temperature for higher and lower contents in Co, respectively.

Keywords: Ferromagnetism, giant magnetoresistance, multilayers, nanowires, nanostructures, electrodeposition, NiCu/Cu, NiCo/Cu.

# Acknowledgements

I would like to thank my supervisor Professeur Luc Piraux of the EPL/BSMA at Université catholique de Louvain for his expertise and advice. The door to Professeur Piraux's office was always open whenever I had a question regarding my research or writing. I also want to thank him for giving me the opportunity to work on an interesting and challenging topic.

I must express my profound gratitude to Yenni Guadalupe Velázquez Gálvan and Tristan da Câmara Santa Clara Gomes for their guidance, their teaching and their valuable time during this whole year. Their meticulous and precious reading of this work considerably helped me improve its quality.

Moreover, I would like to thank Joesphine Lebrun for her collaboration during this year. I am grateful to my family for their constant motivation and particularly to my father and Marine Carpentier for proofreading this Master's thesis. Finally, I am enormously thankful to Victor Hamer for his invaluable support.

# Contents

# List of Symbols

| | |
|---|---|
| $\uparrow$ | Majority spin carrier |
| $\downarrow$ | Minority spin carrier |
| $\cdot$ | Scalar product operator |
| $\parallel$ | Parallel |
| $\perp$ | Perpendicular |
| $\alpha$ | Spin asymmetry coefficient |
| $\beta$ | Bulk spin asymmetry coefficient |
| $\delta$ | Wall width |
| $\Delta$ | Difference operator |
| $\epsilon_F$ | Energy at the Fermi level |
| $\eta$ | Overpotential |
| $\theta$ | Angle between magnetisation and easy axis |
| $\phi$ | Angle between magnetic field and magnetisation |
| $\rho$ | Resistivity |
| $\rho_\perp$ | Resistivity when magnetisation perpendicular to current |
| $\rho_\parallel$ | Resistivity when magnetisation parallel to current |
| $\rho_\uparrow$ | Resistivity in majority spin current channel |
| $\rho_\downarrow$ | Resistivity in minority spin current channel |
| $\rho_{av}$ | Average resistivity |
| $\mu_0$ | Vacuum permeability |
| $\mu_B$ | Bohr magneton |
| $\chi$ | Susceptibility |
| $a$ | Lattice parameter |
| $a$ | Activity |
| $\underline{B}$ | Magnetic induction |
| $d_\uparrow$ | d-up band |
| $d_\downarrow$ | d-down band |
| $E^0$ | Normal electrode potential |
| $E_a$ | Anisotropy energy |
| $E_D$ | Energy associated to the demagnetising field |
| $E^{dep}$ | Deposition potential |
| $E^{eq}$ | Equilibrium potential |
| $F$ | Faraday constant |
| $GMR_{IP}$ | In-plane giant magnetoresistance |
| $GMR_{OOP}$ | Out-of-plane giant magnetoresistance |
| $\underline{H}$ | Magnetic field |
| $H$ | Magnetic field strength |
| $H_a$ | Anistropy field |
| $H_A$ | Applied external field |
| $H_c$ | Coercivity |
| $H_D$ | Demagnetising field |
| $H_{eff}$ | Effective field |
| $H_{eff}^{Co/Cu}$ | Effective field of Co/Cu multilayers |

| | |
|---|---|
| $H_i$ | Internal field |
| $H_{max}$ | Maximum applied field |
| $I$ | Current |
| $J$ | Exchange coupling constant |
| $K_u$ | Anisotropy constant |
| $I(t)$ | Cathodic current |
| $l_{OF}$ | Length of a nanowire |
| $l_{bl}$ | Thickness of a bilayer |
| $m$ | Mass |
| $\underline{m}$ | Magnetic moment |
| $\underline{M}$ | Magnetisation |
| $M$ | Magnetisation intensity |
| $M$ | Metal |
| $M_c$ | Critical number of bilayers |
| $M_r$ | Remanence |
| $M_s$ | Saturation magnetisation |
| $M_M$ | Molar mass of metal atoms |
| $M^{n+}$ | Metal ion with charge $n+$ |
| $n_\uparrow$ | Number of spin-up electrons |
| $n_\downarrow$ | Number of spin-down electrons |
| $n_{bl}$ | Number of bilayers |
| $\underline{N}$ | Demagnetising tensor |
| $P$ | Porosity |
| $R$ | Ideal gas constant |
| $R_{cath}$ | Resistance of the residual cathode |
| $R_{CNWs}$ | Resistance of the crossed nanowire array |
| $R_{ext}$ | External resistance |
| $R_{max}$ | Maximum resistance |
| $R_{min}$ | Minimum resistance |
| $R_{min,OOP}$ | Minimum resistance when field applied out-of-plane |
| $R_{min,IP}$ | Minimum resistance when field applied in-plane |
| $R^{OOP}$ | Resistance when field applied out-of-plane |
| $R_sple$ | Sample resistance |
| $\underline{S}$ | Total spin angular momentum |
| $S$ | Spin quantum number |
| $t$ | Time |
| $t_{bl}$ | Bilayer thickness |
| $t_N$ | Electrodeposition time of nonmagnetic layer |
| $t_{Ni}$ | Electrodeposition time of Ni layers |
| $t_{NiCo}$ | Electrodeposition time of NiCo layers |
| $t_{Cu}$ | Electrodeposition time of Cu layers |
| $t_{OF}$ | Overfil time |
| $T$ | Temperature |
| $T_c$ | Curie temperature |
| $U$ | Interaction energy |
| $V$ | Volume |
| $V_{lock-in}$ | Lock-in potential |
| $V_{meas}$ | Measured potential |

# List of Acronyms

| | |
|---|---|
| 3D | Three-dimensional |
| Ω | Ohm (unit) |
| $\mu$m | Micrometer (unit) |
| A | Ampere (unit) |
| AC | Alternating current |
| Ag | Silver |
| AgCl | Silver chloride |
| AGM | Alternating gradient magnetometer |
| AMR | Anisotropic magnetoresistance |
| AP | Anti-parallel |
| aq | Aqueous |
| Au | Gold |
| Ar | Argon |
| BCC | Body-centered cubic |
| CIP | Current in the plane |
| Cl | Chloride |
| Co | Cobalt |
| $CoSO_4$ | Cobalt(II) sulphate |
| CPP | Current perpendicular to plane configuration |
| Cr | Chromium |
| CNWs | Crossed nanowires |
| Cu | Copper |
| DC | Direct Current |
| DCD | Direct-current demagnetisation |
| DOS | Density of States |
| EDX | Energy-dispersive X-ray spectroscopy |
| FCC | Face-centered cubic |
| Fe | Iron |
| FE-SEM | Field-emission scanning electron microscope |
| FM | Ferromagnetic |
| FORCs | First-order reversal curves |
| G | Gauss (unit) |
| GMR | Giant magnetoresistance |
| H | Henry (unit) |
| $H_2O$ | Water |
| $H_2SO_4$ | Sulphuric acid |
| $H_3BO_3$ | Boric acid |
| HCNW | Homogeneous crossed nanowire |
| HCP | Hexagonal closed packed |
| He | Helium |
| IP | In the plane |
| J | Joules |

| | |
|---|---|
| K | Kelvin (unit) |
| kΩ | Kilo Ohm (unit) |
| kOe | Kilo Oersted (unit) |
| m | Meter (unit) |
| M | Metal |
| M | Molar (unit) |
| MR | Magnetoresistance |
| ms | Millisecond (unit) |
| NaOH | Sodium hydroxide |
| Ni | Nickel |
| NiCo | Nickel-cobalt alloy |
| NiFe | Permalloy |
| $NiSO_4$ | Nickel(II) sulfate |
| $Ni(SO_3NH_2)_2$ | Nickel-II-sulphamate |
| nm | Nanometer (unit) |
| NM | Non-magnetic |
| NW | Nanowire |
| NWs | Nanowires |
| Oe | Oersted (unit) |
| OOP | Out of the plane |
| P | Parallel |
| PC | Polycarbonate |
| PID | Propportional-integral-derivative |
| PNWs | Parallel nanowires |
| Pt | Platinum |
| s | Second (unit) |
| Sc | Scandium |
| SEM | Scanning Electron Microscopy |
| SI | International unit system |
| T | Tesla (unit) |
| V | Volt (unit) |

# List of Figures

# List of Tables

# Introduction

This Master's thesis studies complex architectures of nanowires (NWs) in the field of nanomagnetism and spintronics. It follows previous studies on three-dimensional (3D) interconnected NW networks performed at Université catholique de Louvain (UCL). The NWs have been synthesised using a bottom-up technique in track-etched polycarbonate (PC) membranes, which method has been developed by the group of Professor L. Piraux. These membranes offer highly ordered NWs with tunable morphology and size. Besides, their fabrication allows the creation of pores of various angles with respect to the normal of the film. As a result, 3D interconnected networks can be fabricated. They are particularly interesting because they offer mechanical robustness and easy measurements. Additionally, electrodeposition is a simple and cheap method that is compatible with different materials such as metals, alloys and composites. By adapting the deposition conditions, NWs, nanotubes, multilayered NWs and core-shell systems can be formed.

Since the discovery of giant magnetoresistance (GMR) in 1988 in alternating layers of iron (Fe) and chromium (Cr) [1], this effect has been extensively studied. Besides the researches on films, scientists have also analysed this effect in magnetic NWs because of their particular geometry, their robustness and their future application in nanotechnologies. Some examples are sensors [2, 3], in energy harvesting and storage systems [4] and solar cells [5]. Recently, crossed nanowires (CNWs) have been studied over parallel nanowires (PNWs) because they are self-supported and show more magnetic isotropy [6]. As a result, macroscopic systems can be fabricated. They find applications in magnetoresistive devices as well as magnetic recording devices [7].

Previous works on Ni/Cu films revealed a GMR ratio of about 3% at room temperature [8, 9] and up to 9% at low temperature [10] whereas measurements on PNWs indicated a low percentage of less than 1% [11]. Therefore, these multilayers were tested on CNW templates to increase the GMR effect. The objective of this work is to study the magnetic and magneto-resistance properties of 3D CNW networks of Ni/Cu. For that purpose, the electrodeposition conditions will be modified and their influence analysed. Indeed, by adjusting the parameters of the synthesis, better conditions can be found in order to observe an isotropic magnetic behaviour as well as high GMR ratio. Furthermore, a high GMR ratio was obtained in a previous study on NiCo/Cu CNWs containing about 50% of Co [12]. That is why the evolution of the GMR will be studied when increasing the content of Co in Ni.

This thesis is divided in three parts. In the first chapter, the theory behind magnetism and spintronics will be reviewed, and more specifically the magnetic properties and magnetoresistance of ferromagnetic materials. Then, in order to make the reader familiar with NWs, the possible fabrication techniques will be presented. Moreover, the principle of track-etching and electrodeposition will be explained. Finally, the properties of NWs intervening in the rest of this work will be investigated.

Secondly, the synthesis and the characterisation of the NWs networks will be explained. The specificity of the PC membranes will be presented, followed by the electrodeposition parameters. After the synthesis, the characterisation devices will be detailed. The morphology and composition of the NWs will be characterised by scanning electron microscopy (SEM) and energy dispersive X-Ray spectroscopy (EDS). Then, the magnetic properties will be investigated by analysing the hysteresis loop of the samples obtained with alternating gradient magnetometer (AGM). Finally, the magneto-transport measurements will focus on current-perpendicular-to-the-plane giant magnetoresistance

(CPP-GMR) by submitting the samples to a magnetic field and measuring their varying resistance.

Finally, the results of the magnetic and magneto-transport measurements will be presented and discussed. The first part is dedicated to Ni/Cu multilayers and investigates the influence of the template porosity and the electrolytic solution on the hysteresis loop and the magnetoresistance. The electrodeposition times and potentials of the magnetic and non-magnetic layers will be optimised to give the most isotropic behaviour as well as a high GMR ratio. After finding the best deposition conditions for Ni/Cu multilayers, the evolution of the results with an increasing content of Co, and so with an increasing total anisotropy, will be analysed for two different solutions. Similarly to Ni/Cu multilayers, the electrodeposition conditions will be optimised and then, the best samples will be measured at low temperature.

# Chapter 1

# State of the art

The first chapter of this Master's thesis aims at giving a theoretical background on magnetism, with further interest on ferromagnetic materials. As will be seen, ferromagnets exhibit interesting properties allowing to study spin electronic effects. That is why the basics of spintronics will be explained. Afterwards, the fabrication of NWs will be reviewed as well as the properties linked to magnetic NWs. Finally, the interest behind 3D interconnected multilayered NWs will be presented.

## 1.1 Magnetic properties

Before talking about the magnetic properties of bulk materials, it is important to understand where magnetism originates from. The atoms constituting the matter are responsible for it. Indeed, they behave like tiny permanent magnets, characterised by a magnetic moment, which is due to the combination of the orbital moment and spin of the electrons. Therefore, if the resultant of the moments of each atom inside a small volume $d\gamma$ of the material is different from zero, the matter is magnetised and this volume carries a magnetic moment

$$d\underline{m} = \underline{M} d\gamma, \tag{1.1}$$

where $\underline{M}$ is the *magnetisation* and represents the magnetic moment per unit volume [13].

Inside the magnetised volume, the *magnetic induction* $\underline{B}$ is given by

$$\underline{B} = \mu_0(\underline{H} + \underline{M}) \tag{1.2}$$

or

$$\underline{B} = \underline{H} + 4\pi\underline{M}, \tag{1.3}$$

where $\underline{H}$ is the external magnetic field and $\mu_0$ is the vacuum permeability which is equal to $4\pi 10^{-7}$. Equation 1.2 is expressed in the international system (SI) whereas Equation 1.3 is provided in the CGS system. The differences between the two systems are gathered in Table 1.1.

| | $\underline{B}$ | $\underline{H}$ | $\underline{M}$ |
|---|---|---|---|
| SI units | Tesla (T) | $\mathrm{A/m}$ | $\mathrm{A/m}$ |
| CGS units | Gauss (G) | Oersted (Oe) | $\mathrm{emu/cm^3}$ |
| Conversion | $1\,\mathrm{T} = 10\,\mathrm{kG}$ | $1\,\mathrm{A/m} = 4\pi 10^{-3}$ Oe | $1\,\mathrm{emu/cm^3}$=$10^3\mathrm{A/m}$ |

Table 1.1: Conversion of the magnetic induction $\underline{B}$, the magnetic field $\underline{H}$ and the magnetisation $\underline{M}$ between SI and CGS units [14].

Outside the matter $\underline{B}$ and $\underline{H}$ are linked by

$$\underline{B} = \mu_0 \underline{H} \qquad (SI), \tag{1.4}$$

$$\underline{B} = \underline{H} \qquad (CGS). \tag{1.5}$$

To determine whether a material is magnetic or not, the *magnetic susceptibility* $\chi$ is defined. It allows to obtain the value of $\underline{M}$ under an external field $\underline{H}$ and is given by

$$\underline{M} = \chi \underline{H} \tag{1.6}$$

and the SI units are $\mathrm{H/m}$. Besides, $\chi$ is temperature dependent and its expression is given by the Curie-Weiss law:

$$\chi = \frac{C}{T - T_c} \tag{1.7}$$

where $T_c$ is the *Curie temperature*, C is a constant and T is the temperature. By combining Equations 1.2 and 1.6, $\underline{B}$ can be rewritten by

$$\underline{B} = \mu_0(1 + \chi)\underline{H}. \tag{1.8}$$

Moreover, depending on the response of a magnetic material to a field $\underline{H}$, this latter can be classified among diamagnetic, paramagnetic, ferromagnetic, ferrimagnetic or antiferromagnetic materials [13].

The first category is diamagnetism, which is present in all materials. It comes from the induced modifications of the orbital motion of electrons under a field $\underline{H}$. Hence, any atom exhibits a magnetic moment in the opposite direction of $\underline{H}$, which contributes for a temperature independent and negative value of $\chi$ (Fig. 1.1). However, this form of magnetism is very weak and $\chi$ has an order of magnitude of $10^{-5}$ [13].

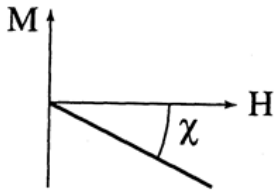


Figure 1.1: Characteristic of a diamagnetic material: variation of the magnetisation $\underline{M}$ as a function of the magnetic field $\underline{H}$ [13].

In paramagnetic materials, permanent and freely oriented magnetic moments are present (Fig. 1.2a). Under a field $\underline{H}$, the moments align and therefore, a weak induced magnetisation is generated parallel to the field. Consequently, the magnetic susceptibility is positive and its value lays between $10^{-3}$ and $10^{-5}$ at room temperature [15]. Moreover, $\chi$ is inversely proportional to the temperature (1.2c). As a result, $\underline{M}$ is stronger when the temperature is decreased (Fig. 1.2b).

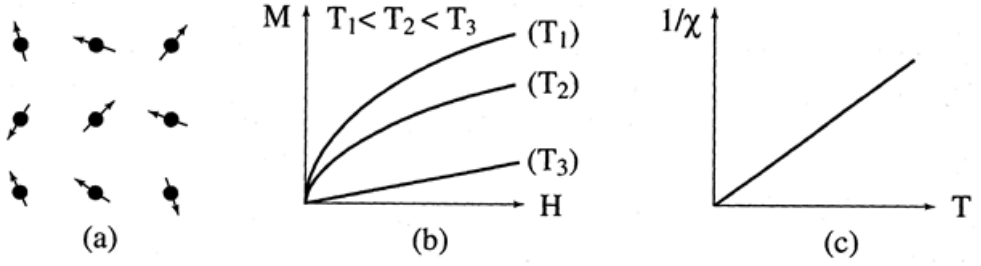


Figure 1.2: Characteristics of a paramagnetic material: a) atomic moments, b) variation of the magnetisation $\underline{M}$ as a function of the magnetic field $\underline{H}$ for different temperatures $T_1 < T_2 < T_3$, c) variation of the opposite of the susceptibility $\chi$ as a function of temperature T [13].

The third category is composed of ferromagnetic materials. Ferromagnets have aligned moments (Fig. 1.3a) with constant magnetisation even in the absence of an external field $\underline{H}$. This possibility of spontaneous magnetisation makes ferromagnetism the strongest form of magnetism and $\chi$ is of

the order of $10^6$. The reason for that behaviour has been introduced by Pierre Weiss in 1910 with the theory of ferromagnetism. It says that the applied field is helped by another stronger magnetic field generated by the solid itself, called *molecular field* or *mean field*. The existence of this mean field is due to the fact that neighbouring atoms starts to orient themselves in the direction of the applied field. As a consequence, Weiss made the assumption that the molecular field, which is parallel to $\underline{H}$, is proportional to $M$. Therefore, the effective field acting inside the solid becomes $\underline{H} + \lambda\underline{M}$ [13]. At high temperature, thermal agitation is significant and the action of the effective field is given by Equation 1.7. As is depicted on Figures 1.3c and 1.3d, the behaviour of ferromagnets changes with the temperature:

- $T < T_c$: the magnetic moments are aligned and a spontaneous magnetisation is present,
- $T > T_c$: the moments are disoriented because of thermal agitation. There is no more spontaneous magnetisation and ferromagnets behave as paramagnetic materials. When the temperature is decreased, the magnetisation decreases, and is equal to zero at $T_c$,
- $T = T_c$ : $\chi$ is infinite, which means that the magnetisation can be different from zero when an external field goes to zero.

For instance, the Curie temperature of nickel is $631\,\mathrm{K}$, whereas it is $1388\,\mathrm{K}$ for cobalt [16].

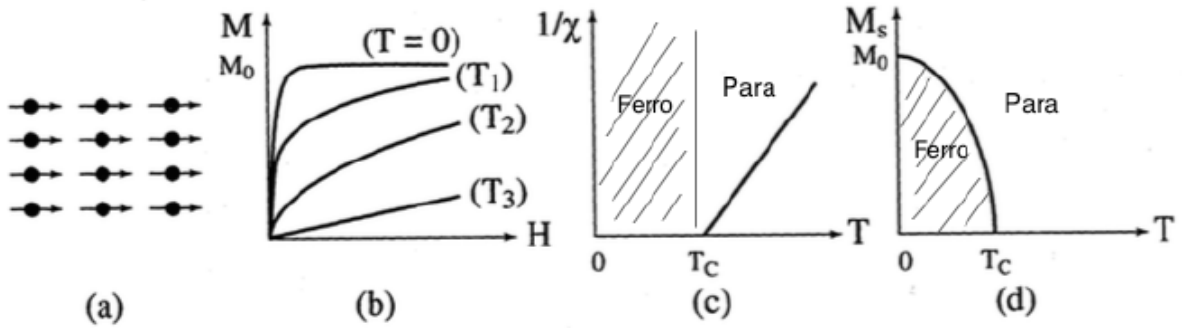


Figure 1.3: Characteristics of a ferromagnetic material: a) atomic moments, b) variation of the magnetisation $\underline{M}$ as a function of the magnetic field $\underline{H}$ for different temperatures $T_1 < T_c < T_2 < T_3$, c) variation of the opposite of the susceptibility $\chi$ as a function of temperature T and d) thermal variation of the spontaneous magnetisation $\underline{M}_s$ [13].

The molecular field takes its origin from the Pauli exclusion principle that states that two electrons can not occupy the same quantum state. Indeed, a consequence of this principle is that the bonding energy of the atoms in a molecule depend on the spin of the bonding electrons. This is the origin of the so-called *exchange forces* that are responsible for the coupling of the magnetic moments of the atoms and thus also for the molecular order. In order to describe this phenomenon, Heisenberg's model can be used under the assumption that magnetic moments are associated to pure intrinsic kinetic moment. This constitute a good approximation in transition metals. The interaction energy between two atoms of spins $\underline{S}_i$ and $\underline{S}_j$ can be written by

$$U_{ij} = -2J\underline{S}_i \cdot \underline{S}_j \tag{1.9}$$

where J is an energy called *exchange integral*. If the two spins are aligned, the value of J is positive and the energy is minimum. Otherwise, an anti-parallel alignment gives a negative value of J [13, 15]. For a solid composed of a large number of atoms, the total interaction energy of the magnetic moments is given by

$$U = -\sum_{i,j} J_{ij} S_i S_j \tag{1.10}$$

In the solid, the mix of orbitals leads to the loss of atomic magnetic moment. There exists two categories of elements for which magnetism remains in solids. The first one is the rare earth, with gadolinium, terbium and dysprosium and the second one is the transition metals. The last category is composed of the well-known Fe, Co and Ni. These two last materials were used during this thesis and that is why their magnetic properties will examined in more details.

### 1.1.1 Ferromagnetism of transition metals

Transition metals form an important family with interesting magnetic properties. For the ten first transition metals, the 4s and 3d energy states have close energies. The 4s state accepts two electrons whereas the 3d states accepts ten electrons. When a solid is formed, these two states behave differently. While the 3d levels are close to the atomic nucleus, the 4s levels have a larger scope. As a result, the s-band is larger than the d-band with a width of $5\,\mathrm{eV}$. Then, the density of state of a d-band is two states per eV and per atom whereas it is 0.3 states per eV and per atom of a s-band [13]. In transition metals, the 4s and 3d bands overlap. This is illustrated on Figure 1.4. Nevertheless, the only ferromagnetic materials are Fe, Co and Ni and this is due to their instability of the d-band, which comes from exchange phenomena.

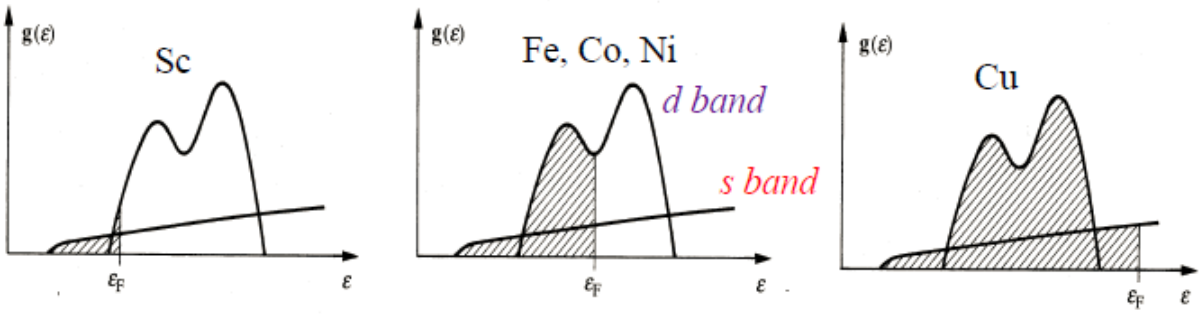


Figure 1.4: Illustration of the band filling of Scandium (Sc), ferromagnetic transition metals and Cu [17].

At high temperature, ferromagnetic materials have no magnetic moment because the d-band of the spin-up ($d\uparrow$) and spin-down ($d\downarrow$) electrons are equally filled (Figs. 1.5a and 1.5b). As a consequence, the total number of spin-up ($n\uparrow$) and spin-down ($n\downarrow$) electrons is the same. When $T < T_c$, the $d\uparrow$ and $d\downarrow$ bands spontaneously shift as is shown on Figure 1.5c, which confers to the system a magnetisation $\underline{M}$ given by

$$\underline{M} = \Delta n \mu_B, \tag{1.11}$$

where $\Delta n = n\uparrow - n\downarrow$ and $\mu_B = e\hbar/2m_e$ is the Bohr magneton and a magnetic moment m given by

$$m = \frac{n\uparrow - n\downarrow}{N}\mu_B, \tag{1.12}$$

where N is the total number of atoms per unit volume. For instance, $n = 2.2\,\mu_\mathrm{B}$ for Fe, $m = 1.7\,\mu_\mathrm{B}$ for Co and $m = 0.6\,\mu_\mathrm{B}$ for Ni at $0\,\mathrm{K}$ [13].

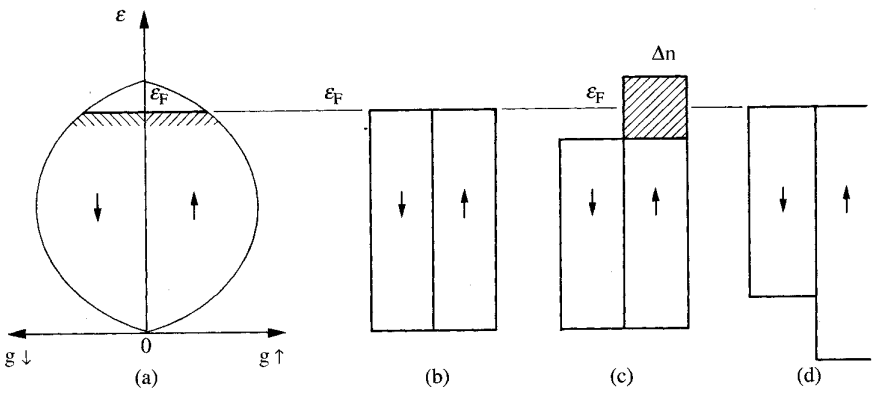


Figure 1.5: Population of the d bands in the paramagnetic state [13].

When the shift occurs, $\Delta n$ is not equal to zero anymore. Consequently, $\underline{M}$ induces an exchange field $\mu_0\lambda\underline{M}$ and the energy $+\mu_B$ or $-\mu_B$ of each electron goes down or up. As a result, the $d\uparrow$ and $d\downarrow$ bands shift so that both Fermi levels are the same (Fig. 1.5d). This energy difference comes from two contributions:

- Firstly, $\Delta n/2$ electrons have their energy transferred above $\epsilon_F$. This variation of energy is given by

$$\Delta E_1 = \frac{\Delta n}{2}\delta\epsilon, \tag{1.13}$$

where $\delta_\epsilon$ is the gain for each electron and is given by $\delta\epsilon\frac{g(\epsilon_F)}{2} = \Delta_n/2$ with $\frac{g(\epsilon_F)}{2}$ the density of state in each sub-band. Therefore, Equation 1.13 becomes

$$\Delta E_1 = \frac{(\Delta n/2)^2}{g(\epsilon_F)/2} = \frac{(\Delta n)^2}{2g(\epsilon_F)}. \tag{1.14}$$

- Secondly, the dissymmetry of the spin-up and spin-down electrons creates an exchange field, with which they interact. The total energy variation during this process is given by

$$\Delta E_2 = \frac{1}{2}(n\uparrow\delta\epsilon\uparrow + n\downarrow\delta\epsilon\downarrow)\Delta E_2 = -\frac{1}{2}(\Delta n)^2\mu_B^2\mu_0\lambda, \tag{1.15}$$

where $\delta\epsilon\uparrow = -\mu_B\mu_0\lambda M = -\mu_B^2\mu_0\lambda\delta n$ and $\delta\epsilon\downarrow = \mu_B\mu_0\lambda M = \mu_B^2\mu_0\lambda\delta n$.

The instability of the d-band will spontaneously happen if $\Delta E_1 + \delta E_2 < 0$, which means that

$$\mu_B^2\mu_0\lambda g(\epsilon_F) > 1. \tag{1.16}$$

This is the Stoner criterion. It applies for Fe, Co and Ni because the density of state at the Fermi level is high for the d-band.

Figure 1.6 illustrates the energy bands of the three transition metal. A big difference can be noticed between Fe, Co and Ni when looking at the filling of the $d\uparrow$ band. As can be seen, the $d\uparrow$ bands of Co and Ni are completely filled. That is why they are called strong ferromagnets.

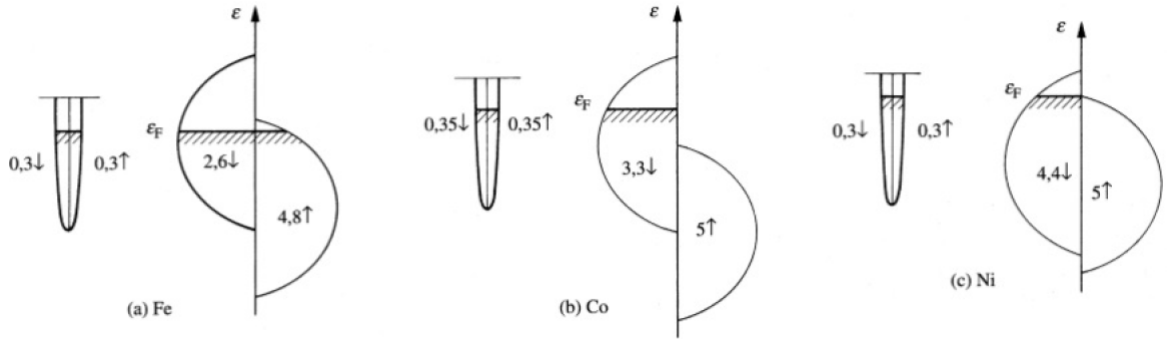


Figure 1.6: Filling of the 3d and 4s bands in a) Fe, b) Co and c) Ni [13].

The average magnetic moment of ferromagnetic metal is depicted by the Slater-Pauling curve on Figure 1.7. It shows the evolution of the average magnetic moment per atom as a function of the average number of conduction electrons. As can be seen, the moment is decreasing with the number of electrons for NiCu and NiCo alloys.

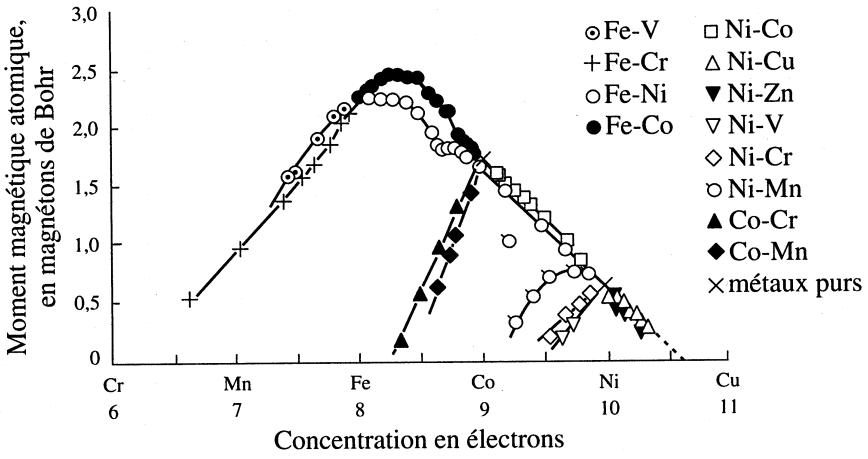


Figure 1.7: Evolution of the average magnetic moment per atom as a function of the average number of conduction electrons [13].

### 1.1.2 Ferromagnetic domains

For lower temperatures than $T_c$, the electronic magnetic moments of a ferromagnet are parallel due to the exchange coupling. Besides, at microscopic scale, ferromagnets have spontaneous magnetised magnetic domains, called *Weiss domains*, in which the individual moments are parallel. However, from one domain to another, the magnetisation orientation is usually different. The formation of these domains is due to the minimisation of the total energy of the system, which is given by

$$E = E_{exchange} + E_{magnetostatic} + E_{Zeeman} + E_{magnetocrystalline} + E_{magnetoelastic} + E_{wall}, \tag{1.17}$$

and that has different contributions [13, 15]:

- $E_{exchange}$ (Exchange interaction): it is due to the coupling between magnetic moments. Its expression is given by
- $E_{Zeeman}$ (Zeeman energy): it describes the reaction of the system under an applied magnetic field. The magnetisation tends to align parallel to the external field and the energy is given by Equation 1.18

  $$E_{Zeeman} = -\mu_0 \underline{M} \cdot \underline{H} = -\mu_0 M H cos\phi, \tag{1.18}$$

  where $\phi$ is the angle between $\underline{H}$ and $\underline{M}$.
- $E_{magnetostatic}$ (Magnetostatic anisotropy): it is due to the internal energy of the system as well as the shape of the material, that favours certain magnetisation orientation.
- $E_{magnetocrystalline}$ (Magnetocrystalline anisotropy): it comes from the symmetry of the crystal that favours the magnetisation orientation.
- $E_{magnetoelastic}$ (Magnetoelastic anisotropy): it results from mechanical deformation.
- $E_{wall}$ (Wall energy): magnetic walls have an energy per unit volume that increases the exchange energy. Besides, this energy is the highest, close to the wall.

It has been explained that the exchange energy $E_{exchange}$ tends to align the magnetic moments in parallel. Nevertheless, the parallel alignment generates an increase of the magnetostatic energy $E_{magnetostatic}$. As can be seen on Figure 1.8, when only one domain is present, large external magnetic fields are induced and the magnetic energy is high. Then, to decrease the spatial extension of the field outside the material, domains are formed. This results in an increase of the exchange energy and a decrease of the magnetostatic energy. The more domains are present, the smaller the induced external field.

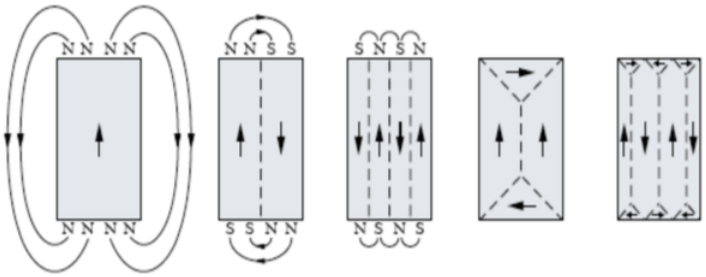

Figure 1.8: Monodomain and multidomain structures of a ferromagnet [13].

It must be stressed that the transition from one domain wall to another is not abrupt but happens on a given wall width $\delta$, given by

$$\delta = \pi\sqrt{\frac{JS^2}{Ka}}, \tag{1.19}$$

with J the exchange coupling constant, S the spin quantum number, K the magnetic anistropy constant and $a$ the lattice parameter [15]. For instance, $\delta$ is equal to $82\,\mathrm{nm}$ for Ni and $14\,\mathrm{nm}$ for Co [18].

The walls can be classified depending on the angle between the magnetisation of two neighbouring domains. The most common type is a Bloch wall, for which the magnetisation is anti-parallel, as is shown on Figure 1.9a. In thin films, the Néel wall is present and the rotation of the magnetisation takes place in a plane perpendicular to the plane of the wall (Fig. 1.9b). These two types of walls are commonly encountered in face-centred cubic (FCC) or body-centred cubic (BCC) structures.

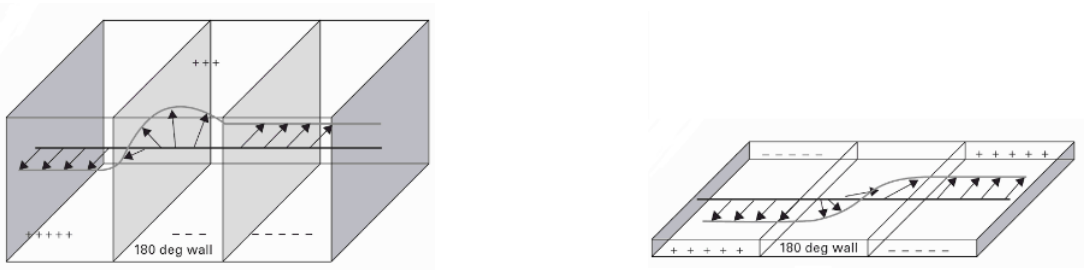


(a) Bloch wall

(b) Néel wall

Figure 1.9: Representation of a) a Bloch and b) a Néel wall [19].

### 1.1.3 Magnetic anisotropy

In order to understand the magnetic hysteresis loop that will be presented in this thesis, magnetic anisotropy is important. If there is only one privileged axis, which is called an uniaxial anisotropy, the *anisotropy energy* $E_a$ can be written by

$$E_a = K_U sin^2\theta\ [\mathrm{J/m^2}], \tag{1.20}$$

with $K_U = [\mathrm{J/m^2}]$ is the anisotropy constant and $\theta$ the angle between the magnetisation and the easy axis [13]. When no magnetic field is applied to a material, its magnetisation is oriented along a certain direction, called *easy axis*. Then, increasing the field makes the magnetisation move away from the easy direction and align with the field. If the field is applied perpendicularly to the easy axis, this direction is called the *hard axis*. This concepts is presented on Figure 1.10. The field required to saturate the magnetisation in one hard axis is called the *anisotropy field* and is given by

$$\underline{H_a} = \frac{2K_U}{\mu_0 \underline{M_s}}, \tag{1.21}$$

where $\underline{M_s}$ is the saturation magnetisation.

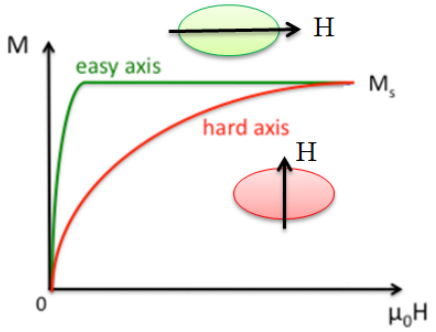


Figure 1.10: Illustration of a magnetisation curve along the easy and hard axis when a magnetic field is applied. Figure adapted from [13].

The magnetostatic, magnetocrystalline and magnetoelastic anisotropy are three contribution to the magnetic anisotropy. However, as magnetostriction is not present for this work, only magnetostatic and magnetocrystalline anisotropy will be developed.

**Magnetostatic and shape anisotropy** Magnetostatic anisotropy is governed by the existence of a demagnetising field $\underline{H_D}$, which is, for a ferromagnetic material, the field that counteracts the magnetisation. The energy $E_D$ associated to the demagnetising field is given by

$$E_D = -\frac{1}{2}\mu_0 \int_V \underline{M} \cdot \underline{H_D}\, dV, \tag{1.22}$$

with $\underline{M}$ the local magnetisation and V the volume of the magnetic matter. The field $\underline{H_D}$ is a linear function of the magnetisation $\underline{M}$ and they are oppositely oriented, which writes

$$\underline{H_D} = -\underline{\underline{N}}\, \underline{M}, \tag{1.23}$$

where $\underline{\underline{N}}$ is the tensor of the demagnetising field coefficients. Therefore, the internal field $H_i$ can be written by

$$\underline{H_i} = \underline{H_A} + \underline{H_D}, \tag{1.24}$$

where $H_A$ is the applied external field [13, 20].

If the coordinates of the system are parallel to the axis of an ellipsoidal object, the only non-zero entries of the tensor N are on the diagonal. These three components are called the *demagnetising factors* and they must satisfy $N_x + N_y + N_z = 1$ (for SI units, and $4\pi$ for CGS). The values of the demagnetising factors can be found for different geometries (Fig. 1.11):

- Sphere: $N_x = N_y = N_z = 1/3$
- Cylinder in z: $N_x = N_y = 1/2$ and $N_z = 0$. $\underline{H_D}$ is very weak if the magnetisation is oriented along z.
- Thin film: $N_x = N_y = 0$ and $N_z = 1$. $\underline{H_D}$ is maximum when it is perpendicular to the surface.

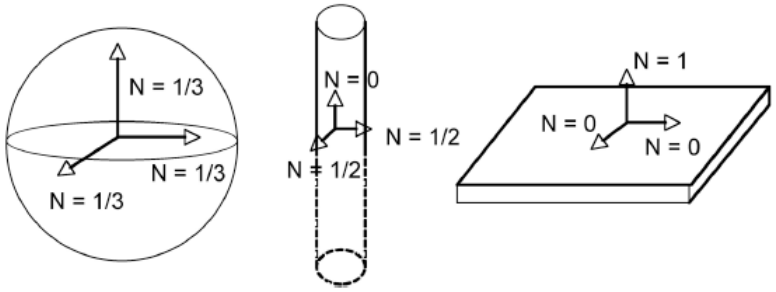


Figure 1.11: Influence of the solid geometry on the demagnetising factors on a sphere, cylinder and thin film (from left to right) [13].

As was mentioned, shape anisotropy influences the magnetostatic energy. This contribution tends to preferentially orient the magnetisation along the larger dimension of the sample. As a consequence, it emerges for thin films and elongated objects. For a wire that has a very small diameter compared to its length, the coefficient of the demagnetising field is equal to zero in the axial direction and the magnetisation is preferentially oriented along the axis of the wire. This is illustrated on Figure 1.12.

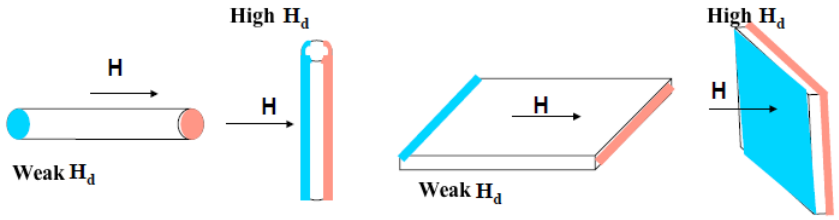


Figure 1.12: Preferential orientation of the magnetisation due to shape anisotropy for a cylinder and a thin film [13].

For instance, in a uniformly magnetised object, which is the case for an ellipsoid, the demagnetising field is uniform. Therefore, by combining Equations 1.22 and 1.23, the energy density can be written by [21]

$$E_D = \frac{1}{2}\mu_0 V N M_s^2. \tag{1.25}$$

**Magnetocrystalline anisotropy** For a spherical monocrystalline sample, the magnetisation depends on the crystallographic directions. For instance, for FCC Ni, the easy directions are the $< 111 >$ directions whereas the hard axis are oriented along $< 100 >$ (Fig. 1.13a). As far as Co is concerned, it has a hexagonal closed packed (HCP) structure and the easy axis is oriented along the c-axis whereas the hard directions are in the plane of the base (Fig. 1.13b).

This magnetocrystalline energy is due to the spin-orbit coupling, which is the coupling that links the spin of the electron to its orbital movement. Regarding transition metals, the electrons responsible for the magnetism are the 3d electrons. Their orbitals are strongly coupled to the crystal lattice, and therefore, the orbital motion is significantly reduced.

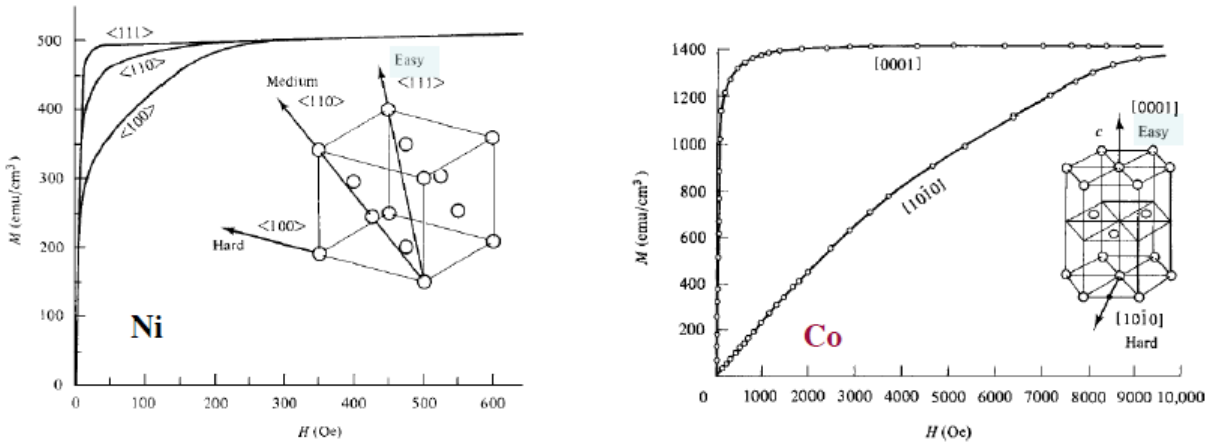


(a) (b)

Figure 1.13: Magnetisation curve of a) Ni and b) Co monocrystals [13].

If the field is applied in the easy direction, the walls separating the domains move so that a monodomain structure is obtained. If the field is applied in the hard axis, the saturation magnetisation is reached for higher external fields. That is because a work is required to rotate the magnetisation away from the crystallographic directions. This is illustrated on Figure 1.13.

### 1.1.4 Magnetic hysteresis measurements

A hysteresis loop is a closed magnetisation curve that provides information about the response of a material subjected to a magnetic field $\underline{H}$. The hysteresis loop of a ferromagnetic material is presented on Figure 1.14. As can be seen, for high values of $H$, the magnetisation is aligned with $\underline{H}$ and reaches a value called *saturation magnetisation* $M_s$. Then, decreasing $H$, the magnetisation $\underline{M}$ rotates to align with easy directions. However, $\underline{M}$ does not go back to zero but reaches a positive value when $H$ is equal to 0, called the *remanent magnetisation* or *remanence* $M_r$. It gives information on how much magnetic flux is kept inside the material once no more field is applied and after magnetic saturation has been reached. The retaining of the magnetisation indicates the ability of a material to be permanently magnetised. Then, further decreasing the magnetic field until $M$ goes to zero corresponds to the material *coercive field* or *coercivity*. The material coercivity is a very important parameter as it is related to the total anisotropic of the material and it is an indicator of the resistance of the material to be demagnetised. For instance ferromagnets can be hard (high $H_c$) or soft (low $H_c$). For instance, Fe and Ni alloys, amorphous alloys and soft ferrites are soft ferromagnetic materials and are easily magnetised and demagnetised [13].

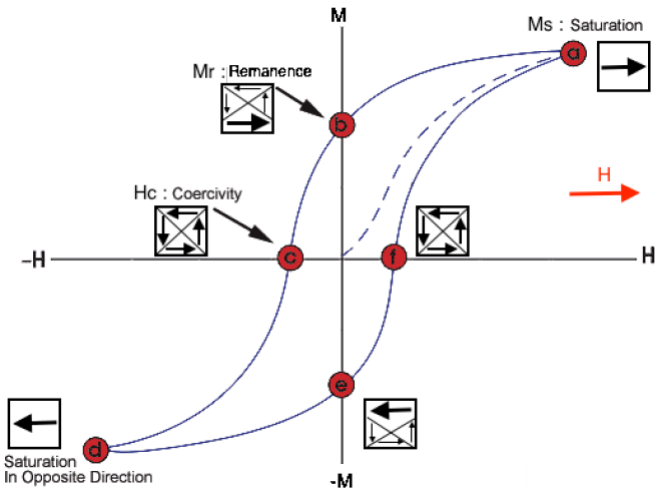


Figure 1.14: Hysteresis loop of a ferromagnetic material (plain line) and its first magnetisation curve in dashed lines. Figure adapted from [13].

To measure the hysteresis loop of a material, this latter is first demagnetised, which means that its magnetisation is reduced to zero. Then, by applying a constant increasing external magnetic field, the first magnetisation curve can be obtained. As is shown on Figure 1.15, the domain walls inside the ferromagnet start to move so that energetically favoured domains start to grow and the others disappear. After that, when there is only one domain left, the magnetic moment rotates and aligns in the direction of the field to finally reach the saturation magnetisation $M_s$. The next step is to lower

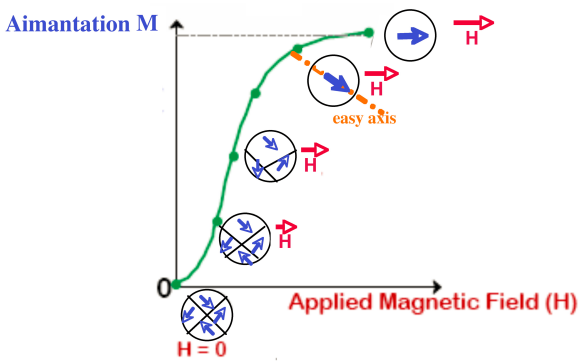


Figure 1.15: First magnetisation curve of a ferromagnetic material [13].

$H$ to zero and then reverse it until reaching a negative field with a magnitude equal to the initial maximum value of $H$. Finally, the same procedure is repeated by sweeping the magnetic field from its largest negative to positive values. When looking at the hysteresis loop of a material, the isotropic or anisotropic behaviour of the system can be determined. In the first case, the obtained hysteresis loops are the same whatever the orientation of the applied field whereas for the second, they change with respect to the orientation of the field.

## 1.2 Magneto-transport properties

This section is dedicated to the magneto-transport properties that will be studied in this thesis. A theoretical background on spin transport will be first reviewed. Then, two types of magnetoresistance, the anisotropic magnetoresistance (AMR) and the giant magnetoresistance (GMR) will be presented.

### 1.2.1 Theoretical background on spin transport

As mentioned in section 1.1, Fe, Co, Ni and their alloys have a different band structure in comparison to other metals because their 3d and 4s energy bands are the last bands to be filled. For ferromagnetic transition metals, the energy bands are split into two subbands that corresponds to each spin configuration. The 4s band is filled by the same number of spin-up and spin-down electrons whereas the 3d bands are shifted (Fig. 1.16). As a result, the density of sates (DOS) of the 3d band is split into majority and minority spin electrons [1].

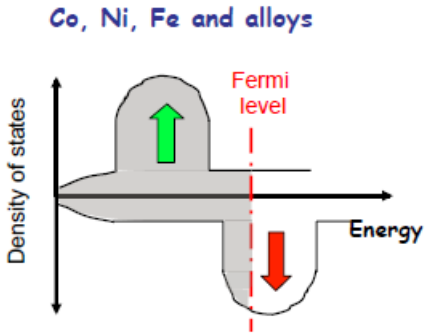


Figure 1.16: Density of states of ferromagnetic transition metals and their alloys [17].

The Mott's two current model states that the length at which an electron travels with a fixed spin,

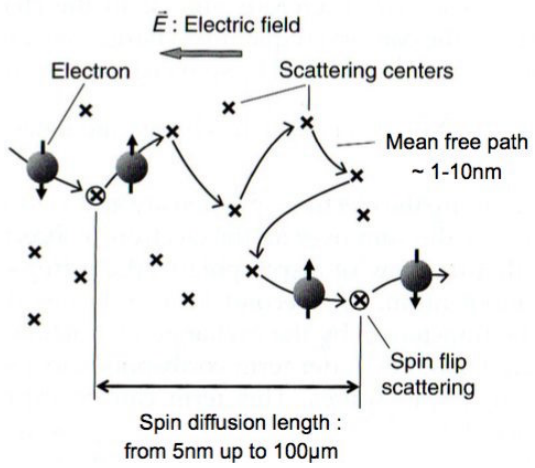


(a)

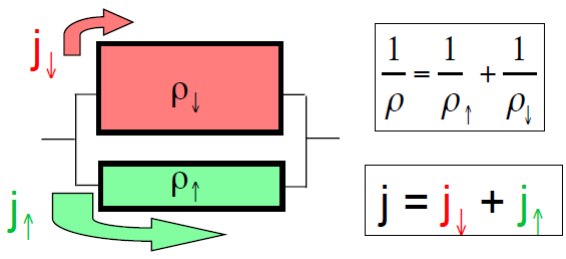


(b)

Figure 1.17: a) Difference between the mean free path and the spin diffusion length at low temperature. b) Representation of the two independent conduction channels with a resistivity $\rho\uparrow$ or $\rho\downarrow$. Figures from [17].

which is called the *spin diffusion length*, is usually much larger than the mean free path (Fig. 1.17a). Then, it can be assumed that the spin is preserved during most scattering in the low-temperature limit. At high temperatures, spin flip can happen, which induce a mixing of the two conduction channels. However, up to room temperature, the mixing can be ignored in first approximation [17].
Therefore, the transport properties of the spin-up and spin-down electrons can be represented by two independent conduction channels as illustrated on Figure 1.17b. Furthermore, each channel has a different resisitivity $\rho\uparrow$ or $\rho\downarrow$ and their interaction is considered negligible. Thus, the total resistivity is given by

$$\rho = \frac{\rho\uparrow\rho\downarrow}{\rho\uparrow+\rho\downarrow}. \tag{1.26}$$

At first approximation, it can be considered that the 4s electrons carry most of the current because they belong to the outer electronic shell. By contrast, the 3d electrons are more localised and responsible for the magnetic properties. Since the two bands are overlapped, the 4s electrons can be scattered on 3d states if they have the same spin and the same energy. The scattering probability at the Fermi level is different for 4s spin-up and spin-down electrons. Indeed, in the case of Co and Ni, for which the Fermi level lies above the $3d\uparrow$ subband, s to d scattering is only possible for spin-down electrons while spin-up electrons can only go from s to s. Consequently, the diffusion rate of the spin-down electrons is larger, and so is their resistivity: $\rho\uparrow < \rho\downarrow$ [1, 17]. This is illustrate on Figure 1.18.

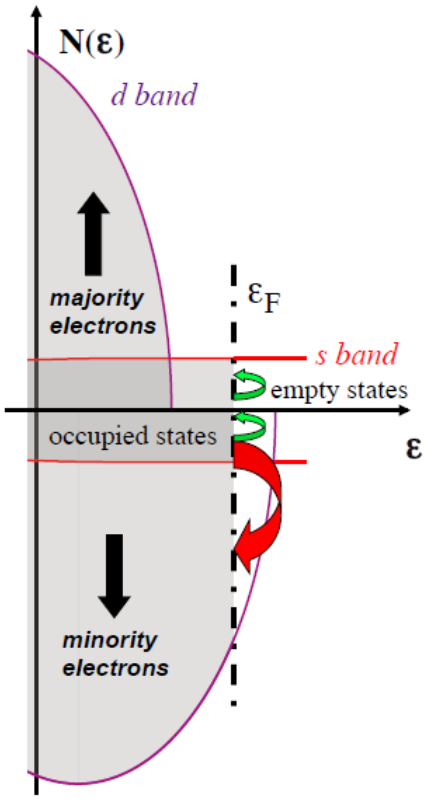


Figure 1.18: Band structure of a ferromagnetic material and representation of the spin-up and spin-down electrons scattering. The spin-up electrons can only go from s to s band whereas the spin-down electrons can go from s to s band and from s to d band [17].

As the resistivity is different between the two channels, the current flows through the lower resistivity channel and then, the current densities become asymmetric. Two spin asymmetry coefficients can be defined by

$$\alpha = \frac{\rho\downarrow}{\rho\uparrow} \neq 1 \tag{1.27}$$

$$\beta = \frac{\rho\downarrow - \rho\uparrow}{\rho\downarrow + \rho\uparrow} = \frac{\alpha - 1}{\alpha + 1} \tag{1.28}$$

Usually, for 3d-ferromagnets, $\rho\uparrow < \rho\downarrow$ and therefore, $\alpha > 1$ and $\beta > 0$. The values are typically $2 < \alpha < 10$ and $0.3 < |\beta| < 0.8$ [17].

### 1.2.2 Magnetoresistance (MR)

The magnetoresistance (MR) is the evolution of the resistance as a function of an external magnetic field and is given by

$$MR = \frac{R_{max} - R_{min}}{R_{max}}. \tag{1.29}$$

Different forms exist, such as the AMR, GMR and the tunneling magnetoresistance (TMR). But for this study, the last form will not be analysed.

#### Anisotropic magnetoresistance (AMR)

The anisotropic magnetoresistance (AMR) defines the evolution of the electrical resistivity as a function of the relative angle between the current ($\underline{I}$) and the magnetisation ($\underline{M}$). As can be seen on Figure 1.19, the resistance oscillates when the angle $\theta$ between $\underline{I}$ and $\underline{M}$ is changed. Its expression is given by

$$\rho(\theta) = \rho_\perp + (\rho_\parallel - \rho_\perp) cos^2\theta, \tag{1.30}$$

where $\rho_\perp$ and $\rho_\parallel$ are the resistivities when $\underline{I}$ and $\underline{M}$ are perpendicular and parallel respectively [17].

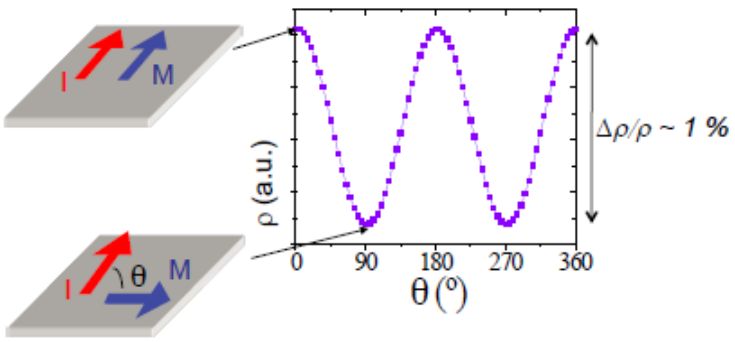


Figure 1.19: Evolution of the resistivity as a function of the angle $\theta$ between the current $\underline{I}$ and the magnetisation $\underline{M}$ [17].

When the field is applied parallel or perpendicularly to the current, the resistivity increases or decreases, respectively. This is related to the larger probability of scattering from s-d when the electrons move in parallel to the magnetisation rather than perpendicularly and it is observed on Figure 1.20. Therefore, the maximum resistance is obtained when the current is parallel to the magnetisation, $\rho_\parallel > \rho_\perp$ [17].

The AMR ratio is defined by

$$AMR = \frac{\Delta\rho}{\rho_{av}}, \tag{1.31}$$

with $\Delta\rho = \rho_\parallel - \rho_\perp$ and the average of the resistance $\rho_{av} = \frac{\rho_\parallel + 2\rho_\perp}{3}$ [22]. $\rho_{av}$ is the resisitivity of a bulk non-magnetic material, for which there exists three equivalent magnetisation directions. Its order of magnitude is about 1% [17].

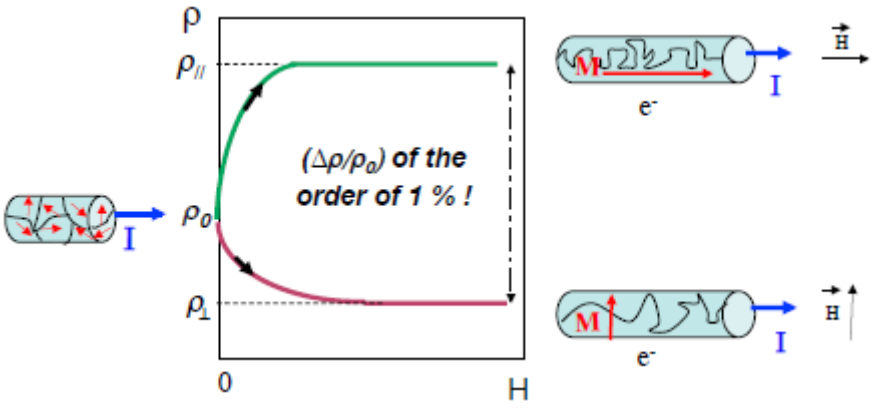


Figure 1.20: Evolution of the resistivity as a function of the magnetic field $\underline{H}$ when the the current $\underline{I}$ and the magnetisation $\underline{M}$ are parallel $\rho\|$ and perpendicular $\rho_\perp$ [17].

### Giant magnetoresistance (GMR)

The first GMR results were obtained on Fe/Cr multilayers in 1986 by the team of Albert Fert. They discovered an exchange coupling that was due to the indirect exchange interaction through the non magnetic layer due to conduction electrons. Consequently, a parallel or anti-parallel alignment of the ferromagnetic layers was generated. As is shown on Figure 1.21, a sudden plummet of the resistance was observed when a strong enough magnetic field to counter the antiferromagnetic coupling was applied. By changing the thickness and the number of layers, a drop from 80% at $4\,\mathrm{K}$ (Fig. 1.21) to 50% at $300\,\mathrm{K}$ between the AP and P configurations was obtained, as well as the alignment of the successive layers [1].

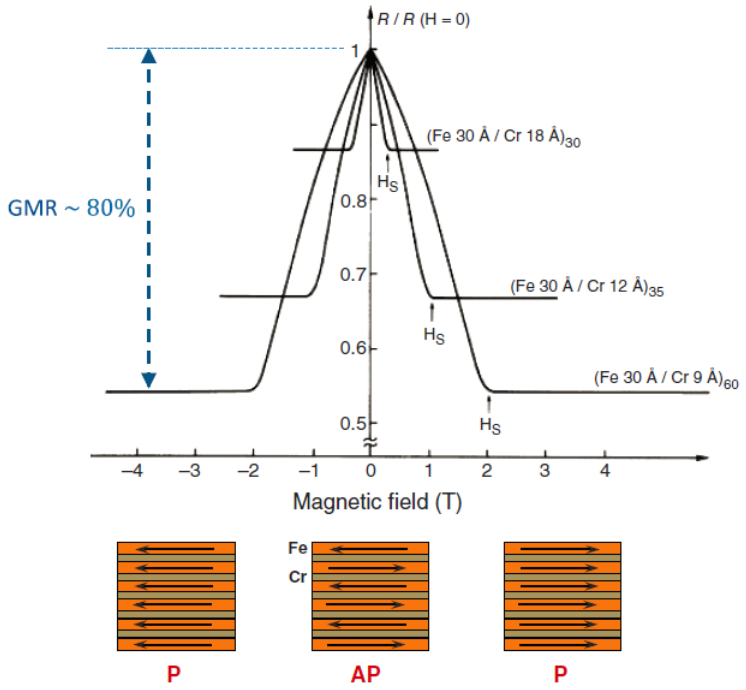


Figure 1.21: Normalised resistance as a function of the external magnetic field for Fe/Cr multilayers [1].

To describe the GMR effect, the two-current model will be used and a multilayer of alternating ferromagnetic (FM) metals and nonmagnetic (NM) metals will be assumed. It will be considered that the magnetisation is uniform in the magnetic layers and that the relative orientation of the magnetisation can be parallel (P) or anti-parallel (AP). Besides, the system will be modelled by a circuit in parallel [1, 17].

Furthermore, two geometries are evaluated in order to analyse the resistance of the multilayered structure: either the current flows parallel to the plane of the layers, which is called current in the plane (CIP) or the current flows perpendicularly to the plane (CPP). This is presented on Figure 1.22. In the first case, the characteristic length is the mean free path whereas it is the spin diffusion length for the second. Although the CIP geometry is easy to implement, the layers must be thin enough compared to the mean free path of the electrons. Besides, the relative orientation of the magnetic moments in the layers must be controlled [1]. Because of theses challenges, Valet and Fert proposed the CPP geometry, which facilitates the measurements along the wire axis and allows a perpendicular transport of the electrons through the interfaces [23].

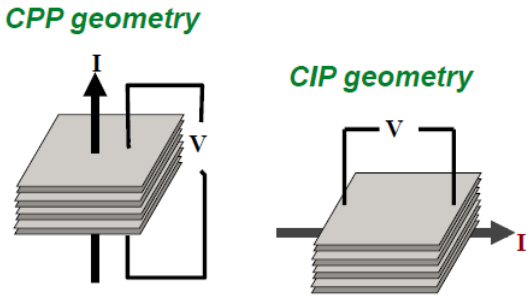


Figure 1.22: Illustration of the different geometries to measure the resistance of a multilayered structure. The current can either flow perpendicularly to the plane of the layers (CPP) or in the plane of the layers (CIP) [17].

As is shown on Figure 1.23, the electrons cross successive FM layers during their Brownian motion through the structure. For the P configuration, the resistance associated with the flowing through the FM layer for majority electrons is defined as r/2 and R/2 for minority electrons, with usually $r < R$. Besides, it is considered that the resistance associated to NM layers is negligible compared to r and R. In this configuration, the spin-up and spin-down electrons are respectively majority and minority electrons so that $r\uparrow = r$ and $r\downarrow = R$. The two channels being parallel, a parallel circuit can be used to model the system. Therefore, the equivalent resistance of the structure can be written by

$$r_P = \frac{rR}{r+R} \approx r. \tag{1.32}$$

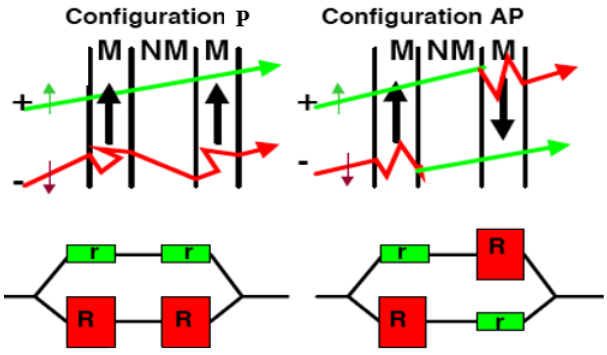


Figure 1.23: Illustration of the flowing of electrons through a multilayer made of magnetic (M) and non-magnetic (NM) layers when the magnetisation of the magnetic layers is parallel (P) or anti-parallel (AP). The path of the spin-up and spin-down electrons are respectively shown in green and red [17].

For the AP configuration, the electrons are successively majority and minority electrons. Therefore, they are alternatively weakly and strongly scattered and the two channels have the same resistance (R+r)/2. Thus, the resistance in the AP configuration is given

$$r_{AP} = \frac{R+r}{4}. \tag{1.33}$$

So, because $R_P < R_{AP}$ for this model, the GMR ratio can be expressed by

$$GMR = \frac{r_{AP} - r_P}{r_P} \tag{1.34}$$

$$= \frac{(R-r)^2}{4Rr} = \frac{(\alpha-1)^2}{4\alpha} = \frac{\beta^2}{1-\beta^2}. \tag{1.35}$$

It is important to point out these explanations are a simplified model of the CPP-GMR helping to understand the origin of GMR. In reality, spin-flip scattering occurs and can not be neglected. Valet and Fert (1999) considered these scatterings and the accumulation of the spins at the interface to model the CPP-GMR geometry. In their paper [24], they started with the Boltzmann transport equation in order to calculate the transport properties of magnetic multilayers and took the volume and interface spin-dependent scattering into account. Then, they showed that if the spin diffusion length is much longer than the mean free path, the Boltzmann equation model could be reduced to a macroscopic model, in which the current densities are linked to the electrochemical potentials. Besides, other more complex models exist and take additional features into account. For instance a thin intermixed layer can be present at the interfaces of the layers and electrons may be reflected, causing a voltage drop. They can both cause an additional spin-dependent interfacial resistance [23].

## 1.3 Fabrication of nanowires

Currently, several techniques have been used to grow magnetic NWs. They can be classified between top-down or bottom-up techniques. The most used top-down approaches are the different lithography techniques, which happen to be more expensive when used at smaller dimensions. Among the bottom-up techniques, self-assembly, chemical vapour deposition, solvothermal and hydrothermal techniques exist. Besides, the NWs are grown on solid surfaces by means of molecular beam epitaxy, electron beam evaporation, phase-shift optical lithography and sputtering. Or, the synthesis of the NWs can be template-assisted. In this case, anodic alumina membranes, nanochannels array glass and track-etched membranes are used, followed by the pore filling in solution by a chemical method, such as electrochemical deposition [25, 26].

Whereas templateless techniques produce highly ordered NWs, the use of a template is an efficient way of controlling the morphology and the size. That is the reason why this type of technique has been used. Moreover, the growth of NWs has been performed by electrodeposition. The reasons are the following: a large number of materials, such as metals, alloys and composites can be deposited, the initial capital investment is low and high production rates can be obtained [27].

During this thesis, track-etching and electrodeposition have both been used. That is why they will be detailed in further details in thi section.

### 1.3.1 Track-etched membranes

The track-etch method is a two-step process presented on Figure 1.24a allowing to obtain porous membranes. First, a nonporous sheet is bombarded with heavy ions parallel to the film surface. These ions damage the sheet as tracks. Then, the tracks are removed using chemical etching to form pores [28].

The three commercially sold sheets are polycarbonate (PC), polyethylene terephtalate (PET) or polyimide (PI) membranes. But other materials such as PVDF, PP, polyethylene naphthalate can be used. The first advantage of this method is that a large range of porosity can be obtained, depending on the ion beam intensity and the rewinding speed of the polymer film. Indeed, commercial templates offer a flexible pore density, going from $10^3$ to $6.10^9$ pores per square centimeter [31]. In addition, adapting the etching conditions, such as the time, the temperature and the strength of the solutions

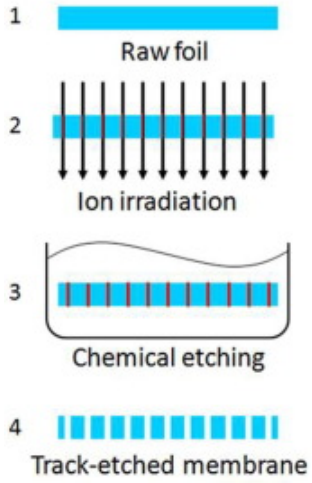


(a)

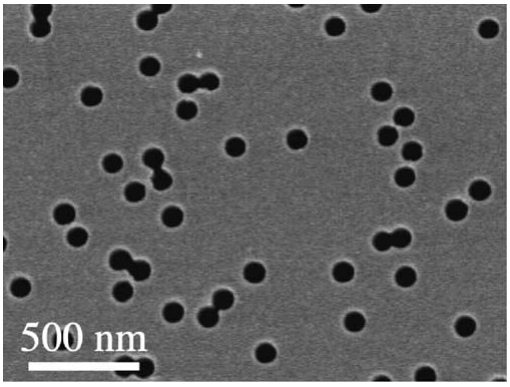


(b)

Figure 1.24: a) Principle of the track-etch method in order to produce nanoporous templates [29]. b) SEM picture of a track-etched polyimide membrane [30].

allows to control the pore shape, size and nanostructuration. It allows the fabrication of multilayered NWs as studied in this thesis. The diameter can be as small as $10\,\mathrm{nm}$, up to 30 $\mu\mathrm{m}$ [31]. Finally, the impact angle can easily be controlled in order to produce parallel arrays or produce particular angles, which prevents the merging of pores [28]. However, the drawback of this technique is that the pores are randomly distributed, as can be observed on Figure 1.24b.

In order to grow CNWs, the track-etched technique can also be used and the same procedure as for PNWs applied, except that the irradiation is performed with given angles. The process is illustrated on Figure 1.25. As can be seen, the advantage is that a template in which 3D interconnected NWs can be grown is obtained. After the electrodeposition, the polymer membrane can be removed and a freestanding macroscopic network of NWs can be obtained.

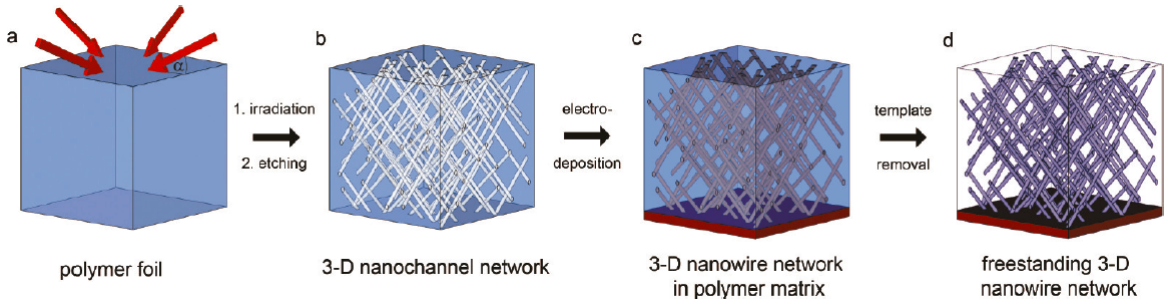


Figure 1.25: Schema of the fabrication of a 3D NW network. a) Irradiation of the polymer foil from different angles. b) After the etching, a 3D nanochannel network is obtained. c) The NWs can be grown in track-etched template by means of electrodeposition. d) By removing the template, a freestanding 3D NW network is obtained [32].

### 1.3.2 Electrodeposition in track-etched membranes

Electrodeposition is a simple method for growing NWs. As is shown on Figure 1.26, the membrane is closed on one side, in this case by a gold (Au) layer and submerged by an electrolytic solution on the other side. Then, the flow of a current through the three electrodes allows the deposition of the specie contained in the solution in the pores of the membranes. The electrodes used are the following: a reference electrode (Ag/AgCl), a counter electrode (anode Pt) and a working electrode (cathode). The cathode can be made of Cr/Au, Cr/Cu or Cr/Cu/Au. The use of separated counter and reference electrodes allows the measurement of the working electrode without interference from the other electrodes.

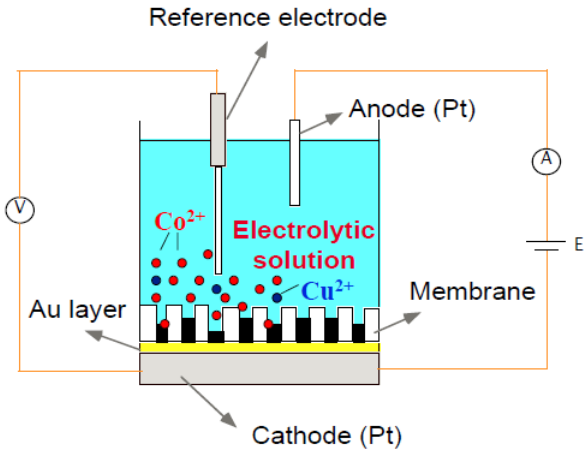


Figure 1.26: Schema of the electrodeposition. The track-etched membrane is covered by an Au layer and placed on a cathode made of Pt. Two other electrodes are used: an anode made of Pt and a reference electrode. [33]

The deposition process consists in the reduction reaction of the desirable materials inside the pores until their complete filling. The general equation of the reduction is given by

$$M^{n+} + ne^{-} \leftrightarrow M, \tag{1.36}$$

where n is the number of electrons. This reversible reaction is characterised by the equilibrium potential $E^{eq}$ that writes

$$E^{eq} = E^{0} + \frac{RT}{nF} ln \frac{a_{M^{n+}}}{a_{M}}, \tag{1.37}$$

where $a_{M^{n+}}$ is the activities of the ions and $a_M$ the activities of the metallic atoms, R is the ideal gas constant ($R = 8.314\,\mathrm{J/Kmol}$), T is the temperature expressed in Kelvin, F is the Faraday constant ($F = 96\,485.339\,\mathrm{C/mol}$) and $E^0$ is the normal electrode potential, measured under standard conditions. For instance, $E^0$ is equal to $0.34\,\mathrm{V}$, $-0.026\,\mathrm{V}$ and $-0.028\,\mathrm{V}$ for the following metal/ion couples $Cu/Cu^{2+}$, $Ni/Ni^{2+}$ and $Co/Co^{2+}$ [27]. The effective electrodeposition is carried out by applying an overpotential $\eta$, which implies a modification of Equation 1.37, expressed by

$$E^{dep} = E^{eq} + \eta. \tag{1.38}$$

Furthermore, the mass of the deposited material is given by

$$m = \frac{M_M}{nF} \int_0^T I(t)dt, \tag{1.39}$$

where $M_M$ is the molar mass of the metal M, T is the duration of the electroposition, I is the cathodic current flowing through the electrochemical cell. This is valid for the perfect case of an efficiency of the electrodeposition equal to 100%. However, in reality, the efficiency is lower, because of side reactions, such as the hydrogen evolution [34].

In addition, a template electrodeposition can be performed by three different techniques: direct current (DC), alternating current (AC) and pulse current deposition. The last technique has been used during this thesis because it offers a better control over the deposition parameters than the other methods. Furthermore, two kinds of methods can be used to induce a current through the solution: a galvanostatic method that applies a constant current to the electrodes or a potentiostatic method applying a constant DC voltage [34].

For this work, a potentiostatic electrodeposition is used. With this method, the potential of the working electrode is kept constant by using a potentiostat. A potentiostat has two purposes: to measure the current between the working and the counter electrodes and to measure and control the

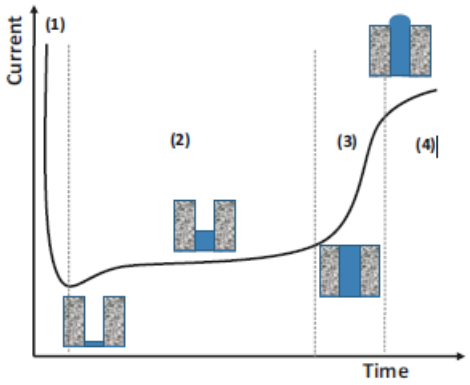


Figure 1.27: Schema of the growth of NWs during electrodeposition [35]

potential difference between the working and the reference electrodes [34]. In other words, the cathodic current density is measured simultaneously in order to monitor the deposition. The advantage of this technique is the precise control of the composition of the deposit, as well the its tunabilitiy allowing to adjust the electrodeposition voltage from the same bath.

The filling of the pores under a constant potential is illustrated on Figure 1.27. As can be seen, different stages exist. The first one is the pre-growth, taking place as soon as the potential is applied through the cell. During this stage, the nucleation starts at the bottom of the pores and the current declines because of the mass transport limitation. After the nucleations, stage 2 takes place and the NWs grow inside the pores, which is marked by a slow increase of the current. When the growing NWs reach the top of the pores, they form hemispherical caps and the current skyrockets (stage 3). When all these caps coalesce, a film covering the template is formed, which induces a increase of the effective cathode area and so, a surge of the current (stage 4) [35].

The form multilayered NWs, the deposition potential has to be switch between the corresponding values of the metals of interest. For that purpose, dual or single bath methods exist. The first one, consists in the deposition of each layer in separated bath, each of them containing the corresponding electrolyte to be reduced. The second method consists in using a single electrolyte, in which the metals to be reduced are present. For this work, a single bath has been used because of its convenience. However, contaminated layers and non-smooth interfaces can be formed. The reason is that, one of the specie is more noble than the other and therefore, is reduced at a higher potential. Supposing A/B multilayers, for which B is the more noble specie. If the reduction potential of B is applied pure layer of B will be formed, whereas at the potential of A, both species are reduced. To limit the contamination as much as possible, the solution has to contain the lowest concentration possible of B in order to obtain a layer rich in A [35].

An example of potential and current versus time during an electrodeposition is shown on Figure 1.28. As can be seen, Ni layers are deposited at a lower potential and for a shorter time than Cu layers. On the corresponding current curve, a sharp rise is observed when the electrodeposition is switched from Ni to Cu, going from a negative to a positive value of the current. This is due either to the depletion of Cu ions or to the dissolution of Ni film at the bottom. Then, it plummets until a plateau is reached, which corresponds to the limiting current of diffusion of Cu. The current corresponding to the Ni layers indicates a minimum followed by a rise, which corresponds to the nucleation and growth process .

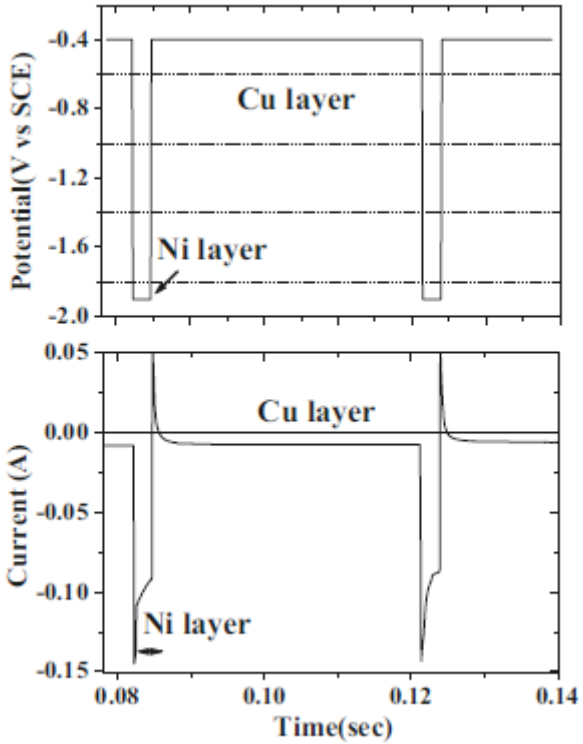


Figure 1.28: Applied potential during electrodeposition of Ni/Cu multilayered NWs and associated current recoreded [35].

## 1.4 Properties of magnetic nanowires

After having seen what techniques can be used to grow NWs, their magnetic and magneto-transport properties will be presented. First, the behaviour of PNWs will be looked at. Then, the way these properties are influenced when multilayers are formed will be looked at. Finally, the influence of switching to CNWs will be presented.

### 1.4.1 Magnetic properties in magnetic nanowires

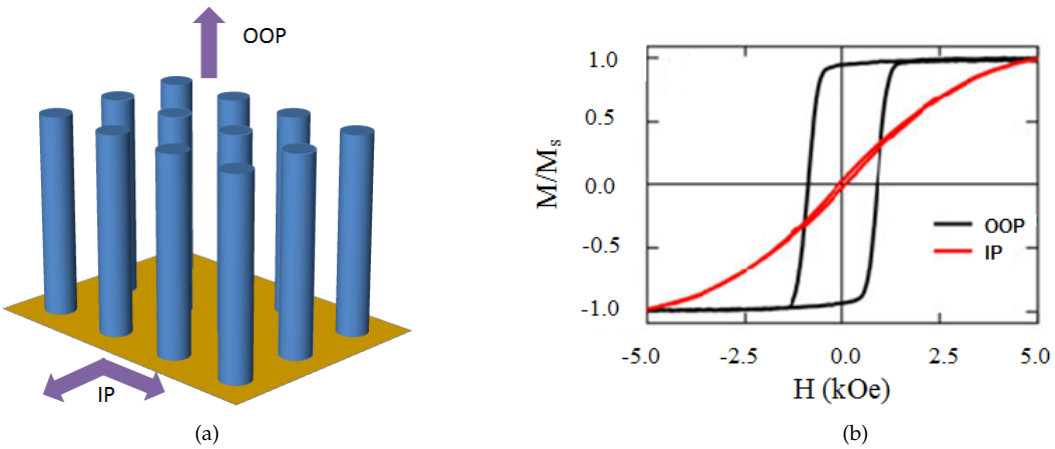


Figure 1.29: a) Definition of the IP in OOP direction of the magnetic field. b) Difference of hysteresis loops when the magnetic field is applied in the IP or the OOP directions [36].

When a PNW array is submitted to a magnetic field, different orientations of the field relative to the wires are possible. Either, the field can be applied in the plane (IP) or out of the plane (OOP) of the film (see Fig. 1.29a). The hysteresis loops of a PNW network is presented on Figure 1.29b. It can be observed that the curve in the OOP direction has higher coercivity and remanence with comparison to

the IP direction. This is due to shape anisotropy associated with the elongated design of the NWs. Indeed, the IP direction corresponds to the application of the field perpendicularly to the axis of the wires, whereas the OOP direction means that the field is parallel to the wires, and thus, oriented along the easy axis. It has to be pointed out that the easy axis is well defined whereas the IP direction can take any orientation perpendicularly to the wire axis.

By contrast to homogeneous PNWs, the formation of multilayers changes the magnetic properties. Indeed, the magnetostatic anisotropy has different contributions: the shape anisotropy and dipolar interactions between the multilayers. The influence of the shape will be first explained. As can be seen on Figure 1.30a, at high aspect ratio, which means the wire is longer than wide, the magnetic layers have the shape of a cylindrical rods. This means that the easy axis is oriented along the cylinder axis, which is similar to a homogeneous NW. Then, when the size of the magnetic layers is reduced, their shape becomes a cylindrical disks, in which case the easy direction is perpendicular to the NW axis. When the magnetic and non-magnetic layers have the same size, the magnetisation can be oriented parallel or perpendicular to the wire axis.

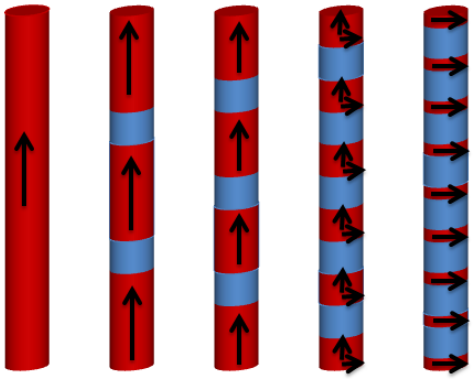

Figure 1.30: Schema of an homogeneous NW as well as multilayered NWs of different thicknesses of the magnetic layers but constant non-magnetic layers. The magnetic material is in red and the non-magnetic spacer is presented in blue. The arrows represent the magnetisation orientation.

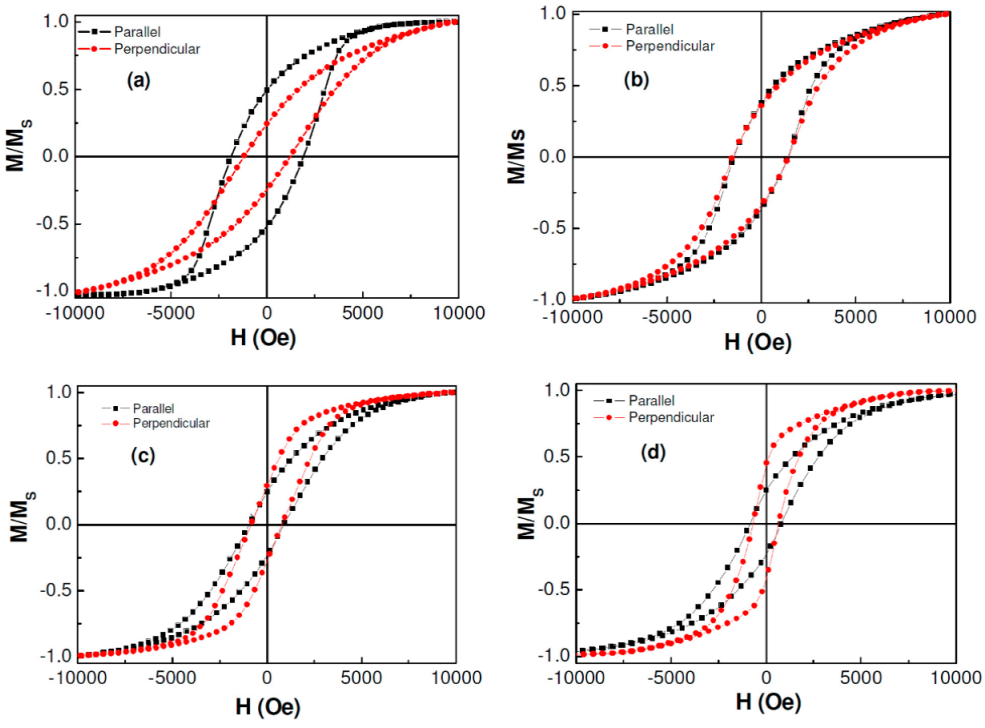


Figure 1.31: Illustration of the influence of changing the size of the magnetic layers on the hysteresis loops [37].

From a hysteresis loop, it can be observed on Figure 1.31 that decreasing the thickness of the magnetic layer while keeping the non-magnetic layers of the same size is translated by the curve in OOP direction becoming thinner and the one in IP direction becoming thicker. First, for large magnetic layers, the magnetisation is parallel to the wire axis and the OOP direction is the easy direction, as presented on Figure 1.31a. Then, when the magnetic and non-magnetic layers are of same size, the systems becomes isotropic, and both curves fit (Fig. 1.31b). If the thickness of the magnetic layer is further decreased, so that the magnetic layer is thinner than the spacer, the easy direction switched to the IP direction, which is marked by the hysteresis loop in the IP direction becoming wider than the one in the other direction (Figs. 1.31c and 1.31d).

De la Torre Medina *et al.* have modelled the effect of layering on magnetostatic interactions [38]. They worked on arrays of parallel multilayers $Co_{0.96}Cu_{0.04}/Cu$ NWs and used a solution with a pH of 2 to ensure that no magnetocrystalline anisotropy is present. Then, they used low density arrays so as to minimise the interactions between the NWs. First, they considered the case of homogeneous NWs, for which the magnetic contributions are purely magnetostatic. The effective field $H_{eff}$ can be written as a function of the self-demagnetising field for an isolated infinite cylinder with a saturation magnetisation $M_s$ and the dipolar interactions between wires and is given by

$$H_{eff} = 2\pi M_s(1 - 3P), \tag{1.40}$$

where P is the porosity. Secondly, when an array of multilayered NWs are considered, many interfaces are created. As a result each magnetic layer interacts with other layers of the same NW as well as other NWs. To simplify the model, low porosity arrays are considered so that the only interactions taken into account are layer to layer inside a single NW. This is valid when the wires are saturated along the cylinder axis (see Figure 1.32). The total demagnetising field along the wire axis is the sum of the subfields at the interfaces. For an array of multilayers, the dipolar field experienced in a single multilayered wire interacting with the whole array can be viewed as the dipolar field generated by an array of homogeneous NWs. This means that the effective field of an array of multilayered NWs is equal to the demagnetising field of an isolated multilayered NW multiplied by the factor $1 - 3P$. Therefore the expression of the effective field for an array of multilayered NWs writes

$$H_{eff}^{Co/Cu} = 2\pi M_s(1 - 3P)\left(1 - 3\left|\sum_{k=0}^{j}(N_{2k} - N_{2k+1}\right|\right). \tag{1.41}$$

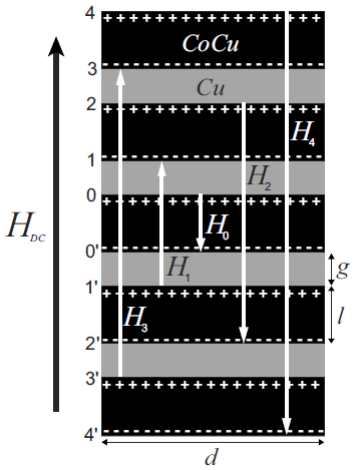


Figure 1.32: Lateral representation of a multilayered NW with diameter d as well as the demagnetising field $H_n$ appearing as a result of the polarisation of the Co layers when a magnetic field $D_{DC}$ is applied. The thickness of CoCu is l and the one of Cu is g [38].

De la Torre Medina *et al.* have shown that the magnetic anisotropy is reduced when reducing the thickness of the magnetic layers [38]. In OOP, they found that the field at which magnetic saturation

is attained increases when the magnetic layers decreases. In IP, thinner magnetic layers showed lower fields to reach saturation. Furthermore, the magnetostatic coupling between the magnetic layers influences the magnetic behaviour. This dipolar coupling depends on the thickness of the non-magnetic layer. Indeed, for large non-magnetic layers, the magnetic layers are isolated and almost decoupled whereas for a thin spacer, the magnetic layers interact and the dipolar coupling leads to a decrease of the rate at which the aspect ratio forces the switch in easy axis. Therefore, similar hysteresis loops as presented on Figure 1.31 can be obtained when the size of the layers are reduced.

The evolution of the anisotropy of a single multilayered NW is depicted on Figure 1.33. The line corresponds to the evolution of the effective magnetostatic field $H_{eff}$ being equal to zero for the pair of aspect ratios for both magnetic ($r_l$) and non-magnetic layers ($r_g$). When $H_{eff} > 0$, the magnetostatic anisotropy favours the orientation of the easy axis along the wire axis whereas a negative value favours a perpendicular orientation. $H_{eff}$ being equal to zero corresponds to an isotropic behaviour.

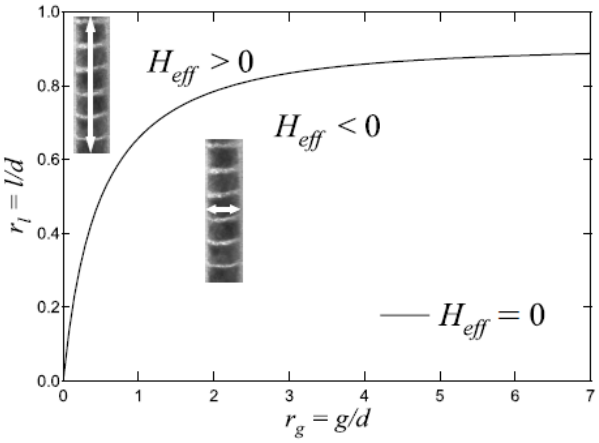


Figure 1.33: Anisotropy diagram as a function of the aspect ratios of the magnetic $r_l = l/d$ and the nonmagnetic $r_g = g/d$ layers. The line shows the values of $r_l$ and $r_g$ for which the effective anisotropy $H_{eff}$ is equal to zero. Above this curve, $H_{eff}$ is positive, while it is negative below . The white arrows on the wires represents the easy axis [38].

When switching to crossed NWs, Araujo *et al.* (2014) have shown that the magnetic anisotropy is significantly reduced when the external field is applied in IP and OOP directions. This reduction is caused by the fact that the demagnetising fields are at an angle of the IP and OOP directions. As can be seen on Figure 1.34, due to a reduction of the magnetic anisotropy, the hysteresis loop of CNW array are more isotropic than the curve of PNW array.

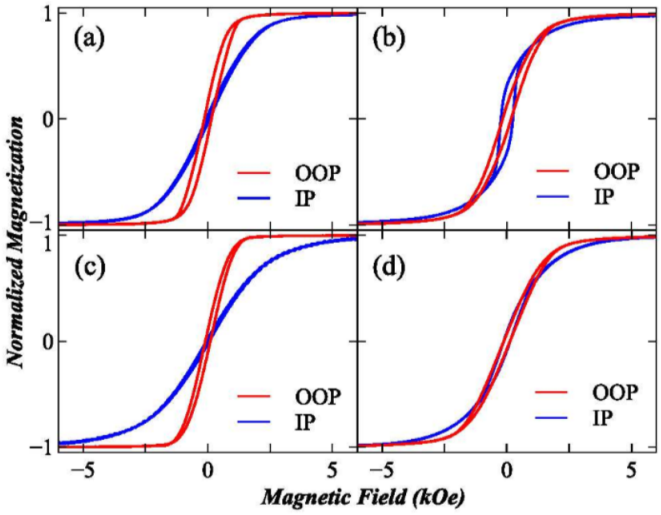


Figure 1.34: Hysteresis loops measured with the external field in the plane (IP) and out of the plane (OOP) directions for a) Ni PNWs, b) Ni CNWs, c) Ni/Fe PNWs and d) Ni/Fe CNWs [6].

### 1.4.2 Magneto-transport properties of magnetic nanowires

The magneto-transport properties of NW arrays will now be looked at. For a parallel array of NWs, a typical MR curve is presented on Figure 1.35b. As can be seen, a maximum and a minimum of resistance occur around $+H_c$ and $-H_c$ in IP and in OOP directions, respectively. This different behaviour between both directions can be understood by the AMR effect in a single NW.

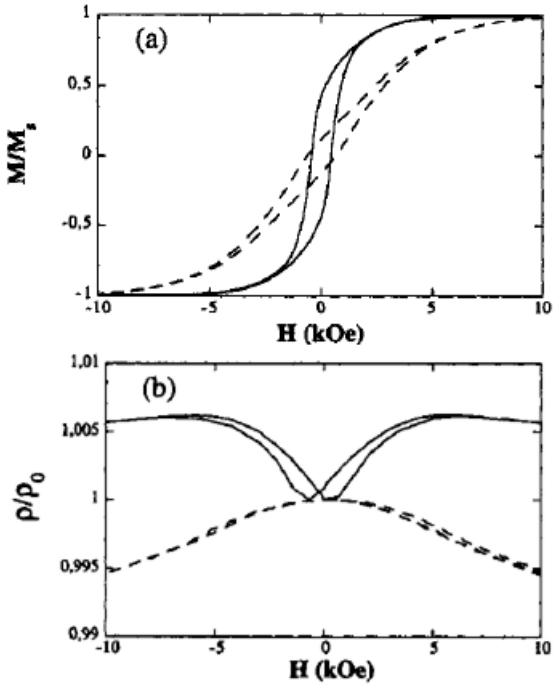


Figure 1.35: Hysteresis loop at room temperature and magnetoresistance at $4.2\,\mathrm{K}$ for an array of $90\,\mathrm{nm}$-diameter Co. The field was applied in the IP (dashed lines) and the OOP (continuous line) directions [39].

If the MR curve of a single NW is looked at on Figure 1.36, it can be seen that the shape of the curves in the OOP and IP directions is different. Besides, a hysteresis of the MR occurs because the shape anisotropy influences the rotation of the magnetisation from the easy axis to the hard axis. When the magnetic field is applied perpendicularly to the wire axis and is decreased, the shape anisotropy of the NW helps the magnetisation to rotate from its hard axis to its easy axis. Therefore, the resistance increases, until reaching a maximum when the magnetisation is parallel to the easy direction, which happens in $-H_c$. If the field is further decreased, the magnetisation is first prevented from rotating because it has to go from the easy to the hard axis. Then, for a field high enough to counteract the anisotropy, the magnetisation rotates and the resistance decreases. In contrast, for the OOP direction,

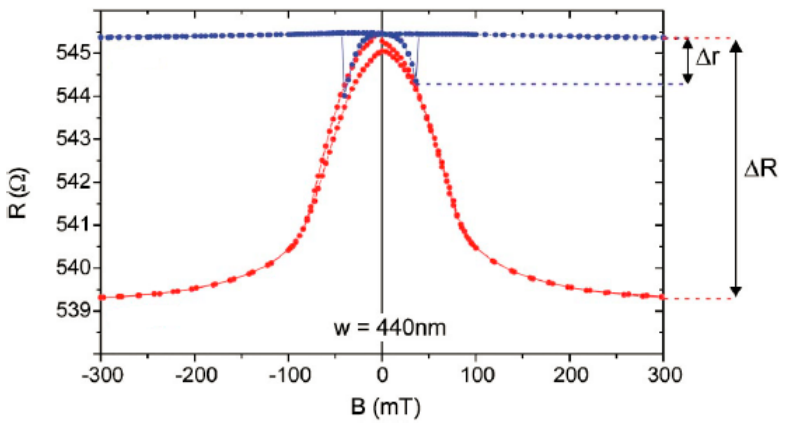


Figure 1.36: Resistance curve of a single $40\,\mathrm{nm}$ wide Co NW with the field applied along the wire axis (blue) and perpendicular (red). The resistance was measured at $4.2\,\mathrm{K}$ [40].

at a higher magnetic field, the resistance is almost constant. Then, if the field is decreased, the spins inside the NW become less aligned with the axis of the current. Therefore, the resistance declines. When the magnetisation switches in the other direction, the spins become more aligned, parallel to the field, which accounts for an abrupt irreversible jump of the resistance in $H_c$. This is due to the fact that the edge of the NW is magnetically weak and that the magnetic domains start to rotate until becoming perpendicular to the wire axis. This generates a wall that propagates nearly instantly, which causes the abrupt jump of resistance up to saturation [40, 41]. This is depicted on Figure 1.37.

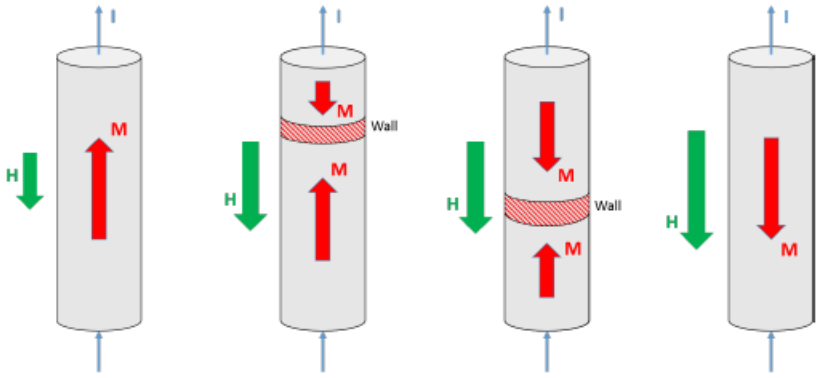


Figure 1.37: Magnetisation reversal of a single monodomain ferromagnetic NW [42].

For multilayered NWs, the GMR effect can be observed because of the relative alignment of the magnetisation of the layers. When no magnetic field is applied, the magnetisation of the different magnetic layers is not aligned and the resistance is high. Then, increasing the field, the magnetisation of the magnetic layers is aligned, which translates into a low resistance state. If the field is again reduced, the alignment of the magnetisation starts to disappear because of the magnetic interactions, and the resistance increases. An hysteresis effect can be observed increasing and decreasing the magnetic field between $8\,\mathrm{kOe}$ and $-8\,\mathrm{kOe}$ as is shown in Figure 1.38. Besides, the curves of CPP-GMR measured at low temperature are also presented. As is seen, the effect is higher at low temperature. That is the increase of the temperature that leads to an enhancement of the spin-flip scattering and a mixing of both channels, which reduces the GMR.

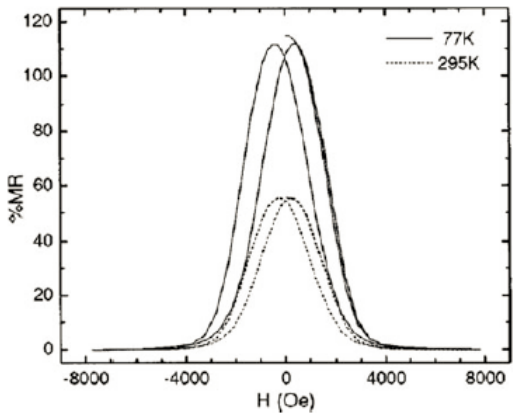


Figure 1.38: CPP-GMR measure for multilayered NW of CoNiCu/Cu at room temperature (dashes line) and at $77\,\mathrm{K}$ (continuous line) [43].

However, it has been reported for Ni/Cu multilayers PNW network that the GMR effect was only observed when the thickness of the magnetic multilayers is lower than the spin diffusion length of Ni, which is approximately $5\,\mathrm{nm}$ [44]. In the opposite case, AMR is observed accounts for most of the MR.

For CNWs, a few number of studies have been realised. In previous works, considerable AMR

effects could be measured in NiFe and Co crossed arrays [45]. Moreover, the study of Co/Cu multilayers CNW network indicated a GMR ratio close to the values obtained for Co/Cu multilayered PNWs [46]. Finally, last year, a thesis showed that NiCo/Cu CNW arrays present very high GMR when adjusting the concentration of Cu in the electrolyte [12].

## 1.5 Interest of nanowires in nanomagnetism and spintronics

A recent interest has been given by the scientific community to 3D interconnected NWs deposited by electrodeposition due to their good mechanical properties, as well as their self-standing network. As a result, a macroscopic array can be obtained, as is shown on Figure 1.39. Besides, the synthesis method offers tunable physico-chemical properties and controlled topologies [46]. 3D NW networks has a broad range of applications in various fields such as in electronics with sensors [2, 3], actuators [2], data storage systems [47] and resistive switching memory [48], or in biology with biosensors [49] and bio-analytical devices [50]. They can also be used in harvesting and storage systems [4], solar cells [5], catalysts [32], microwave absorption [51], electrochromic elements [52] and magneto-optical properties [53].

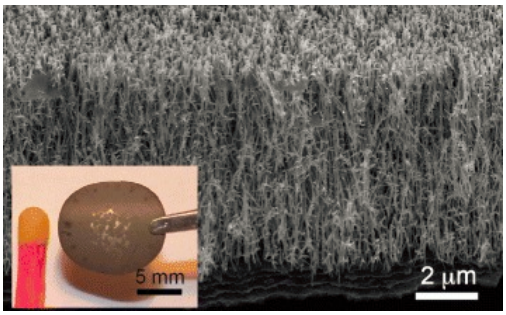


Figure 1.39: SEM images of an interconnected network of electrodepositied 3D Ni crossed NWs with a diameter of 40 nm obtained after dissolution of the membrane [45].

Besides, multilayered NWs are interesting because they exhibit the GMR effect and are then appealing for applications such as magnetoresistive sensors and magnetic recording devices [7]. Previous work on multilayered films have shown promising results. For instance, Sato *et al.*(1994) obtained a magnetoresistance of 9.3% for multilayered Ni/Cu films at 4.2K [10], Bakonyi *et al.* (2004) found about 7% at 4.2K [54], Jafari Fesharaki *et al.* (2012) and Tóth *et al.* (1999) found about 3% for electrodeposited Ni/Cu multilayers [8, 9].

A lot of work has already been done on the analysis of PNW arrays with different combinations of the following materials Co/Cu, NiFe/Cu and NiCo/Cu. Regarding Ni/Cu multilayered NWs, only one study was performed by Serrano-Guisan *et al.* (2006) who found about 0.6% of GMR [11]. However, a few studies have been realised with those materials on 3D interconnected crossed multilayered NWs. Araujo *et al.* (2015) started to work on Ni crossed magnetic NWs and Ni/Fe bilayered NWs [6]. Then, some work has been done on 3D crossed NW networks made of Ni, Co, NiFe and NiCo as well as multilayers of Co/Cu [45, 46, 55]. Two current Master's thesis were also dedicated to those materials as well as multilayers of NiCo/Cu [12, 42], with which a GMR ratio of about 40% at room temperature and 80% at low temperature were obtained.

Because of the good results with Ni/Cu multilayers, multilayered CNWs were investigated, since their shape favours a higher GMR ratio. This thesis first focuses on the analysis of Ni/Cu multilayered CNWs, which had never been investigated before. Moreover, the previous study on NiCo/Cu CNW networks focused on composition of about 50% of Co. Therefore, it has been decided to study the evolution of the GMR with two lower amounts of Co in the magnetic layers. The investigation of the impacts of adding a large quantity of Co will be part of another Master's thesis [56].

# Chapter 2

# Synthesis and characterisation of nanowire arrays

This chapter is dedicated to the fabrication and the characterisation of the NWs. Firstly, the synthesis of the NWs will be presented, by explaining the templates used and their characteristics as well as the parameters of the electrodeposition process. Secondly, the structural characterisation of the NWs will be determined and the results presented. Finally, a description of the characterisation of the magnetic and magneto-transport properties will be described.

## 2.1 Synthesis of the nanowires

### 2.1.1 Template fabrication

The fabrication of the membranes is a two-step exposure process of films to energetic heavy ions. As depicted on Figure 2.1, they were subjected to a first irradiation step with angles of $25°$ and $-25°$ with respect to the membrane surface. Then, the templates were rotated by $90°$ and again bombarded from the same angles to create a complex 3D interconnected network. This procedure is depicted on Figure 2.1b. After the bombardment, the irradiated tracks inside the PC film were chemically etched at $70°C$ with an aqueous solution of $0.5\,\mathrm{M}$ NaOH in order to create pores of the desired diameter and volumetric porosity [6, 45, 46, 55]. Indeed, as was mentioned in Section 1.3.2, the successive track-etching process allows to control the angles, obtain well-defined pore diameters and adjustable porosity.

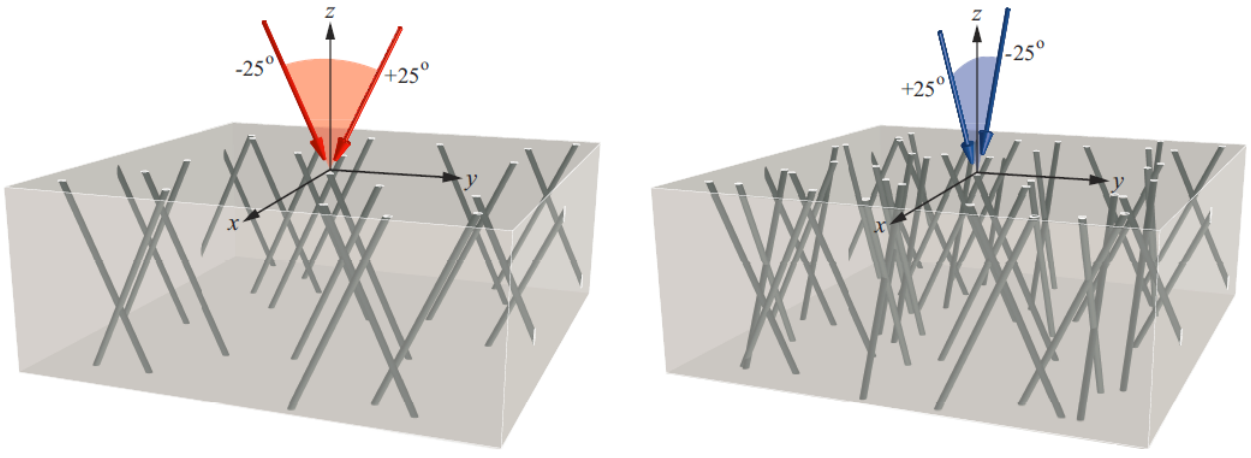


(a) (b)

Figure 2.1: Schema of the track-etched method. a) First, the template is bombarded by ions with angles of $25° \pm 5°$ with respect to the membrane surface. b) Second, the template is rotated by $90°$ and again bombarded by the same angles. Figure from [55].

The PC templates were then coated using a e-beam evaporator with a metallic bilayer, generally Cr/Au or Cr/Cu, to serve as a cathode during the electrochemical deposition. The Cr layer is used as a thin adhesion layer. Besides, the cathode has to be at least three times thicker than the nanopores diameters, in order to close the pores, which eases the growth of the NWs.

During this thesis, different polycarbonate (PC) films of $22\,\mu\mathrm{m}$ thick have been used. They were primarily track-etched from the company *it4ip* SA. Their characteristics as well as the composition of the metallic cathode that was deposited on each membrane is presented in Table 2.1.

| Template label | Type | Cathode | $\phi[\mathrm{nm}]$ | Porosity |
|---|---|---|---|---|
| P 10.1% | Parallel | Cr(15 nm)/Au(330 nm) | 80 | 10.1% |
| C 20% | Crossed | Cr(10 nm)/Cu(150 nm) | 40 | 20% |
| C 3% | Crossed | Cr(3 nm)/Au(400 nm) | 80 | 3% |
| C 0.75% | Crossed | Cr(10 nm)/Cu(100 nm) + Cr(10 nm)/Cu(150 nm) | 40 | 0.75% |

Table 2.1: List of the templates.

The first template has got parallel pores with a diameter of $80\,\mathrm{nm}$ and a porosity of 10.1%. The calibration of the potentials to apply and the composition was first tried on a parallel template. Once those parameters were determined, they were tried and adjusted on most expensive and complex CNW networks. To start with crossed networks, a high packing template with a porosity of 20% and a diameter of $40\,\mathrm{nm}$ has been used. This latter is more robust because of its high interconnectivity. Then, after the adjustment of the parameters, a second crossed template, which has a low porosity of 3% and a pore diameter of $80\,\mathrm{nm}$, has been used and the same optimisation procedure has been repeated to study the influence of the NWs segment interconnections. The last step was to utilise a template with a very low porosity of 0.75%. However, the deposition of multilayers makes the network extremely fragile so that no sample could be measured.

The reason why different templates with a decreasing porosity have been used is linked to the purpose of finding the highest GMR ratio possible. Indeed, higher GMR is expected when the number of crossing zones is lowered. However, the fragility of the template that goes together with lower porosity prevents a direct use of these templates.

### 2.1.2 Electrodeposition

After the fabrication of the templates, different electrolytes were prepared. The first part of this work is focused on Ni/Cu multilayers and therefore, seven different solutions were prepared in order to study their influence on the magnetic and magneto-transport properties. Secondly, Co was added in the NiCu alloy to study the expected enhancement of the GMR ratio.

The details of all the electrolytes used during this work are gathered in Table 2.2. As can be seen, they all contain $0.5\,\mathrm{M}$ of boric acid ($H_3BO_3$) used as buffer solution to ensure a good conductivity.

First, $2.3\,\mathrm{M}$ Nickel Sulfamate tetrahydrated ($Ni(SO_3NH_2)_2 \cdot 4H_2O$) was used based on previous work on NiCu/Cu multilayered NWs and NiCu alloy NWs by Kazeminezhad and Schwarzacker [57, 58]. However, this concentration was really close to the limit of solubility of the electrolyte, which caused stability issues, noticeable by the appearance of precipitates after a few days. As a result, its molarity was diminished from $2.3\,\mathrm{M}$ to $1\,\mathrm{M}$, which resolved the problem.

Secondly, due to the probability of growing core-shell systems with Nickel Sulfamate, Nickel Sulfate hexahydrated ($NiSO_4 \cdot 6H_2O$) was utilised, while keeping the same concentration. They were first compared to analyse their influence on phase separation. Then, Nickel Sulfate was chosen for the rest of the experiments.

Along with these changes, the amount of Copper Sulfate pentahydrated ($CuSO_4 \cdot 5H_2O$) was varies between $2.5\,\mathrm{mM}$ and $15\,\mathrm{mM}$ to improve the multilayers growth. Each solution was given a label detailing the quantity of each specie. As most experiments were realised with the use of $1\,\mathrm{M}$ of $NiSO_4 \cdot 6H_2O$, this latter is not indicated in the label, whereas $Ni(SO_3NH_2)_2 \cdot 4H_2O$ is referred to as NiSfmt followed by its molarity. Besides, the amount of Cu varying for most electrolytes, its molarity is detailed too.

Regarding the second part of the work, two solutions were prepared in order to analyse the evolution of the magnetic and magneto-transport properties of $Ni_xCo_{1-x}/Cu$ multilyered CNWs in which x is equal to minimum 70%. Therefore, Cobalt sulfate heptahydrate $CoSO_4 \cdot 7H_2O$ was added to the previous NiCu solution and the amount of Nickel Sulfate and Copper Sulfate were fixed to $1\,\mathrm{M}$ and $2.5\,\mathrm{mM}$ respectively.

| Electrolyte label | Salts | | | | | pH |
|---|---|---|---|---|---|---|
| | $Ni(SO_3NH_2)_2 \cdot 4H_2O$ | $NiSO_4 \cdot 6H_2O$ | $CoSo_4 \cdot 7H_2O$ | $CuSO_4 \cdot 5H_2O$ | $H_3BO_3$ | |
| NiCu(NiSfmt $2.3\,\mathrm{M}$ Cu $25\,\mathrm{mM}$) | $2.3\,\mathrm{M}$ | / | / | $25\,\mathrm{mM}$ | $0.5\,\mathrm{M}$ | 2.05 |
| NiCu(NiSfmt $2.3\,\mathrm{M}$ Cu $50\,\mathrm{mM}$) | $2.3\,\mathrm{M}$ | / | / | $50\,\mathrm{mM}$ | $0.5\,\mathrm{M}$ | 1.98 |
| NiCu(NiSfmt $2.3\,\mathrm{M}$ Cu $2.5\,\mathrm{mM}$) | $2.3\,\mathrm{M}$ | / | / | $2.5\,\mathrm{mM}$ | $0.5\,\mathrm{M}$ | 2.04 |
| NiCu(NiSfmt $1\,\mathrm{M}$ Cu $2.5\,\mathrm{mM}$) | $1\,\mathrm{M}$ | / | / | $2.5\,\mathrm{mM}$ | $0.5\,\mathrm{M}$ | 2.03 |
| NiCu(Cu$2.5\,\mathrm{mM}$) | / | $1\,\mathrm{M}$ | / | $2.5\,\mathrm{mM}$ | $0.5\,\mathrm{M}$ | 2.06 |
| NiCu(Cu$7.5\,\mathrm{mM}$) | / | $1\,\mathrm{M}$ | / | $7.5\,\mathrm{mM}$ | $0.5\,\mathrm{M}$ | 2.01 |
| NiCu(Cu$15\,\mathrm{mM}$) | / | $1\,\mathrm{M}$ | / | $15\,\mathrm{mM}$ | $0.5\,\mathrm{M}$ | 2 |
| NiCoCu(Co$25\,\mathrm{mM}$) | / | $1\,\mathrm{M}$ | $25\,\mathrm{mM}$ | $2.5\,\mathrm{mM}$ | $0.5\,\mathrm{M}$ | 2.05 |
| NiCoCu(Co$50\,\mathrm{mM}$) | / | $1\,\mathrm{M}$ | $50\,\mathrm{mM}$ | $2.5\,\mathrm{mM}$ | $0.5\,\mathrm{M}$ | 2.08 |

Table 2.2: List of the compositions and pH of the electrolytes used.

After the preparation of each solution, sulfuric acid $2.5\,\mathrm{M}$ ($H_2SO_4$) was added in the electrolytes in order to set the pH around a value of 2. The reason for this is the polycrystalline growth of Ni and Co in a FCC crystal structure. Consequently, no magnetoelastic anisotropy has to be taken into account when analysing the magnetic properties of the samples.

Secondly, circular samples of about $8\,\mathrm{mm}$ were cut from the membrane and placed below an electrodeposition cell, in which the electrolyte were poured, and the reference electrode and the anode were dipped. In this work, a three electrodes system was used at room temperature, which means that a working, a reference and a counter electrodes constitutes the potentiostatic system. The anode was made in Platinum (Pt) whereas the reference electrode was in Silver (Ag)/Silver chloride (AgCl). Then, the pulses were generated and controlled by a EG&G Princeeton Applied Research Potentiostat/Galvanostat Model 263 A at room temperature. The adjustable parameters were the electrodeposition time and the applied potentials.

The chosen potentials are indicated in Table 2.3, as well as the solution used and the electrodeposition times for Ni ($t_{Ni}$), NiCo ($t_{NiCo}$) and Cu ($t_{Cu}$) of the different species. For each composition study, an homogeneous CNWs array was fabricated as a reference sample. Furthermore, only one parameter at a time was changed, whether it is the solution, the electrodeposition potentials or the pulse times, in order to observe their influence on the creation of multilayers. Therefore for each serie, different parameters have been changed and their magnetic and magneto-transport properties were studied. The purpose was to optimise the electrodeposition conditions and then, find the higher GMR ratio.

For the first part, Nickel Sulfamate was used with a first aim of finding around 90% of atomic composition of Ni in the NiCu alloy and the amount of Cu was changed to observe its influence on the multilayers. For the first solution NiCu(NiSfmt$2.3\,\mathrm{M}$ Cu$25\,\mathrm{mM}$), three different potentials for Ni

were tested before growing multilayered PNWs. These potentials were analysed based on previous work with Ni and NiCu: $-1\,\mathrm{V}$ [59], $-1.1\,\mathrm{V}$ [6, 46] and $-1.9\,\mathrm{V}$ [57, 58]. Eventually, the potentials of $-1\,\mathrm{V}$ and $-0.5\,\mathrm{V}$ [46] were respectively chosen to deposit Ni and Cu in multilayered PNWs. Then, two times more Cu was added and the potential was adjusted. This time the potentials $-1\,\mathrm{V}$ and $-1.1\,\mathrm{V}$ were tested on the template P 10.1% and their composition analysed. Based on the results, a potential of $-1\,\mathrm{V}$ was applied to multilayered CNWs with different sizes of FM layers. However, a larger amount of Cu was found, along with GMR results indicating no multilayers. This is the reason why the amount of Cu was reduced to $2.5\,\mathrm{mM}$ and the potential was switched to $-1.1\,\mathrm{V}$, which is the usual potential to deposit Ni [6, 46]. The amount of Cu was also targeted to a lower percentage than 10%. Afterwards, the potentials were adjusted and only CNWs template were employed. Regarding the NiCo/Cu multilayers, a previous study calibrated the potentials of $-1\,\mathrm{V}$ and $-0.4\,\mathrm{V}$ for NiCo and Cu [12].

| Solution | Template | Potentials | $t_{Ni}$ or $t_{Co}$ | $t_{Cu}$ |
|---|---|---|---|---|
| NiCu(NiSfmt2.3 M Cu25 mM) | P 10,1% | $-1\,\mathrm{V}/-0.5\,\mathrm{V}$ | 100 ms-500 ms | 10 s |
| NiCu(NiSfmt2.3 M Cu50 mM) | C 20% | $-1\,\mathrm{V}/-0.5\,\mathrm{V}$ | 100 ms-300 ms | 10 s |
| NiCu(NiSfmt2.3 M Cu2.5 mM) | C 20% | $-1.1\,\mathrm{V}/-0.5\,\mathrm{V}$ | 300 ms | 20 s-30 s |
| NiCu (NiSfmt 1 M Cu 2.5 mM) | C 20% | $-1.1\,\mathrm{V}/-0.5\,\mathrm{V}$ | 75 ms-300 ms | 30 s |
| NiCu(Cu2.5 mM) | C 20% | $-1.1\,\mathrm{V}/-0.5\,\mathrm{V}$ | 150 ms | 6 s-30 ms |
| | C 3% | $-1.1\,\mathrm{V}/-0.5\,\mathrm{V}$ | 150 ms | 30 s |
| | C 3% | $-1.1\,\mathrm{V}/-0.5\,\mathrm{V}$ | 200 ms | 40 s |
| NiCu(Cu7.5 mM) | C 3% | $-1.1\,\mathrm{V}/-0.5\,\mathrm{V}$ | 150 ms | 1 s-16 ms |
| | C 3% | $-1.1\,\mathrm{V}/-0.5\,\mathrm{V}$ | 100 ms | 6 s |
| NiCu(Cu15 mM) | C 3% | $-1.1\,\mathrm{V}/-0.5\,\mathrm{V}$ | 136 ms | 1 s-3 ms |
| | C 3% | $-1.1\,\mathrm{V}/-0.5\,\mathrm{V}$ | 150 ms | 30 s |
| | C 3% | $-1.1\,\mathrm{V}/-0.5\,\mathrm{V}$ | 200 ms | 40 s |
| NiCoCu(Co25 mM) | C 20% | $-1\,\mathrm{V}/-0.4\,\mathrm{V}$ | 350 ms-1 s | 30 s |
| | C 20% | $-1\,\mathrm{V}/-0.4\,\mathrm{V}$ | 700 ms | 10 s-30 s |
| | C 3% | $-1\,\mathrm{V}/-0.4\,\mathrm{V}$ | 700 ms-1.2 s | 30 s |
| NiCoCu(Co50 mM) | C 20% | $-1\,\mathrm{V}/-0.4\,\mathrm{V}$ | 300 ms-1 s | 30 s |
| | C 20% | $-1\,\mathrm{V}/-0.4\,\mathrm{V}$ | 600 ms | 10 s-40 s |
| | C 3% | $-1\,\mathrm{V}/-0.4\,\mathrm{V}$ | 600 ms-1.2 s | 30 s |
| | C 3% | $-1\,\mathrm{V}/-0.4\,\mathrm{V}$ | 1 s | 20 s-40 s |

Table 2.3: Table of the different electrodeposition parameters used for the fabrication of each series of NWs.

When fabricating multilayers, it is important to determine the right thickness of each layer and try to obtain the same thickness for both the NM and the magnetic layers as was explained in Section 1.4. Since the layer thickness must be shorter than the spin diffusion length to avoid any spin flip, and then any loss of information, a thickness of $10\,\mathrm{nm}$ was targeted. For that purpose, homogeneous NWs of NiCu, NiCo or Cu have been first overfilled. By determining the overfill time of both the magnetic and NM layers, the right electrodepositions times for the desired thickness can be estimated. Indeed, as was mentioned in Section 1.3.2, the overfill time $t_{OF}$ can be obtained when looking at the early stage of drastic growth of the I(t) curve. The length of one multilayered NW $l_{OF} = \frac{22}{cos25^\circ}[\mu m]$ is given

by

$$l_{tot} = n_{bl} l_{bl} \tag{2.1}$$

and the overfill time of the sample $t_{OF}$ is

$$t_{OF} = n_{bl}(t_{FM} + t_{Cu}), \tag{2.2}$$

where $n_{bl}$ is the number of bilayers, $l_{bl}$ is the thickness of one bilayer, $t_{FM}$ and $t_{Cu}$ are the electrodeposition times of one pulse of FM material and NM material Cu, respectively . Combining Equations 2.1 and 2.2, the thickness of one bilayer can be found:

$$l_{bl} = l_{tot}(\frac{t_F M}{t_{OF}} + \frac{t_{Cu}}{t_{OF}}) \tag{2.3}$$

Using Equation 2.3, it is possible to estimate the bilayer thickness and it was evaluated on different multilayered CNW arrays. For each of them, the electrodeposition times $t_{Ni}$, $t_{Cu}$, $t_{OF}$ are shown in Table 2.4 as well as the estimated thickness of one bilayer $l_{bl}$. As can be observed, $t_{OF}$ differs for two samples prepared with the exact same parameters. Besides, in the case of a fixed magnetic layer, the longer the electrodeposition time of Cu is, the longer it should take to overfill the pores. However, this is not observed. In addition, when looking at Figure 2.2, some points of the electrolyte NiCu(Cu$7.5\,\mathrm{mM}$) seem inconsistent, such as the one deposited for $9\,\mathrm{s}$ of Cu and some of the repeated samples. Leaving them aside, an almost linear trend can be observed. For the solution NiCu(Cu$15\,\mathrm{mM}$), it is found that when the electropisiton time of Cu triples, the thickness of the Ni layers almost triples too. It is important to mention that the computation is purely theoretical and absolutely not exact. Indeed, it is extremely difficult to identify the exact $t_{OF}$ and as is shown, each sample differs from the others.

| Electrolyte label | $t_{Ni}$ [ms] | $t_{Cu}$ [s] | $t_{OF}$ [s] | $l_{bl}$ [nm] |
|---|---|---|---|---|
| NiCu(Cu$7.5\,\mathrm{mM}$) | 150 | 1 | 6825 | 4.1 |
| | 150 | 3 | 5572 | 13.7 |
| | 150 | 6 | 1743.9 | 13.9 |
| | 150 | 6 | 7450 | 22.4 |
| | 150 | 8 | 5000 | 38.7 |
| | 150 | 9 | 14150 | 15.7 |
| | 150 | 16 | 5750 | 66.6 |
| | 150 | 16 | 6750 | 56.7 |
| NiCu(Cu$15\,\mathrm{mM}$) | 136 | 1 | 2900 | 9.3 |
| | 136 | 3 | 2500 | 29.8 |

Table 2.4: Table of the computed bilayer thicknesses $l_{bl}$ of the seven multilayered samples prepared with solution NiCu(Cu$7.5\,\mathrm{mM}$) and the two samples with NiCu(Cu$15\,\mathrm{mM}$). The calculation was made based on the electrodeposition times of Ni $t_{Ni}$ and Cu $t_{Cu}$ as well as the overfill time $t_{OF}$ required to completely fill the pores.

In the end, the only sample showing the desired thickness is the one deposited for $6\,\mathrm{s}$ of Cu layers with solution NiCu(Cu$7.5\,\mathrm{mM}$) with a bilayer thickness of $22.4\,\mathrm{nm}$. Nevertheless, the estimation of the bilayer thickness does not ensure the deposition of a uniform layer and that they all measure $10\,\mathrm{nm}$. Indeed, a lot of parameters influence the deposition, such as the electrodeposition time, the solution, the reference electrode, the temperature or the potentiostat. If the right conditions are not implemented, instead of having uniform layers, clusters might rather be formed (Fig. 2.3a).

In addition, when multilayers are deposited, two ways of deposition could be imagined. Either the interfaces of the layers could be perpendicular to the length of the wire (Fig. 2.3c) or parallel to the membrane surface (Fig. 2.3b). Nevertheless, a study by da Câmara Santa Clara Gomes *et al.* (2016) demonstrated that the first possibility is correct [45]. Moreover, the way the materials are deposited in the crossing zones is unclear. A mix of materials rather than multilayers or non well defined layers

could be deposited. For those reasons, measurements on low porosity are expected to give better magneto-transport results.

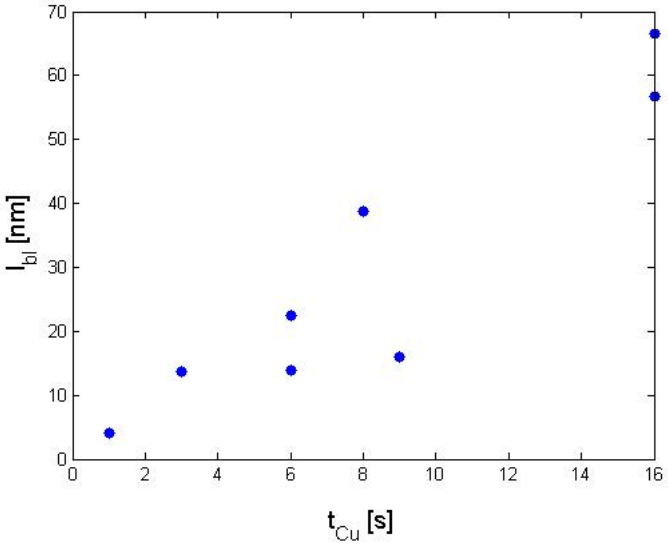


Figure 2.2: Evolution of the bilayer thickness $l_{bl}$ as a function of the electrodeposition time of Cu $t_{Cu}$ [s].

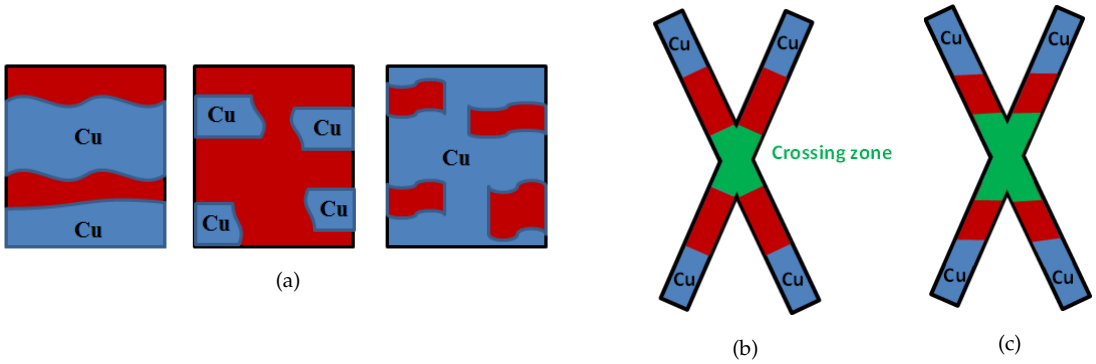


Figure 2.3: a) Sketch of the possible configurations obtained during electrodeposition. The first one is the ideal case of uniform layers whereas the two others can be obtained when the species are not correctly deposit. b-c) Schematic of the possible growth of multilayers CNWs during electrodeposition. The magnetic material is presented in red and the Cu in blue.

## 2.2 Morphology and composition characterisation

In order to analyse the morphology and the composition of the samples, a JEOL FEG SEM 7600F field-emission scanning electron microscope (FE-SEM) equipped with a JEOL JSM2300 energy-dispersive X-ray spectroscopy (EDX or EDS) has been used. The SEM allows to obtain images and so, determine the morphology of the samples, while the EDX gives qualitative and quantitative information on their composition, with a resolution that is lower than 129 eV [60].

A schema of a FE-SEM is presented on Figure 2.4a. The working principle of the SEM is the following: at the top of a column, electrons are produced by a field emission gun, accelerated and passed through lenses and apertures to obtain a focused beam. When the primary electrons hit the sample, elastic and inelastic interactions take place. Elastic interactions means that there is no energy transfer between the primary electrons whereas in inelastic interactions, there is a transfer of energy between the incident electrons and the sample. The high-energy electrons interacting elastically with the sample are called *backscattered electrons*. As far as electrons emitted from inelastic scattering are concerned, they are called *secondary electrons*. As is shown on Figure 2.4b, the electrons can come

from different depths in the sample. During the SEM process, the two previously mentioned types of electron are detected and the signal is transformed into images. Depending on whether they come from a depth close to the sample surface or from deeper, the difference in intensity creates a contrast in the image related to the composition, which allows to see the morphology of the sample. For instance, materials with a high atomic number, such as polymers, will appear brighter on the display monitor [61, 62, 63].

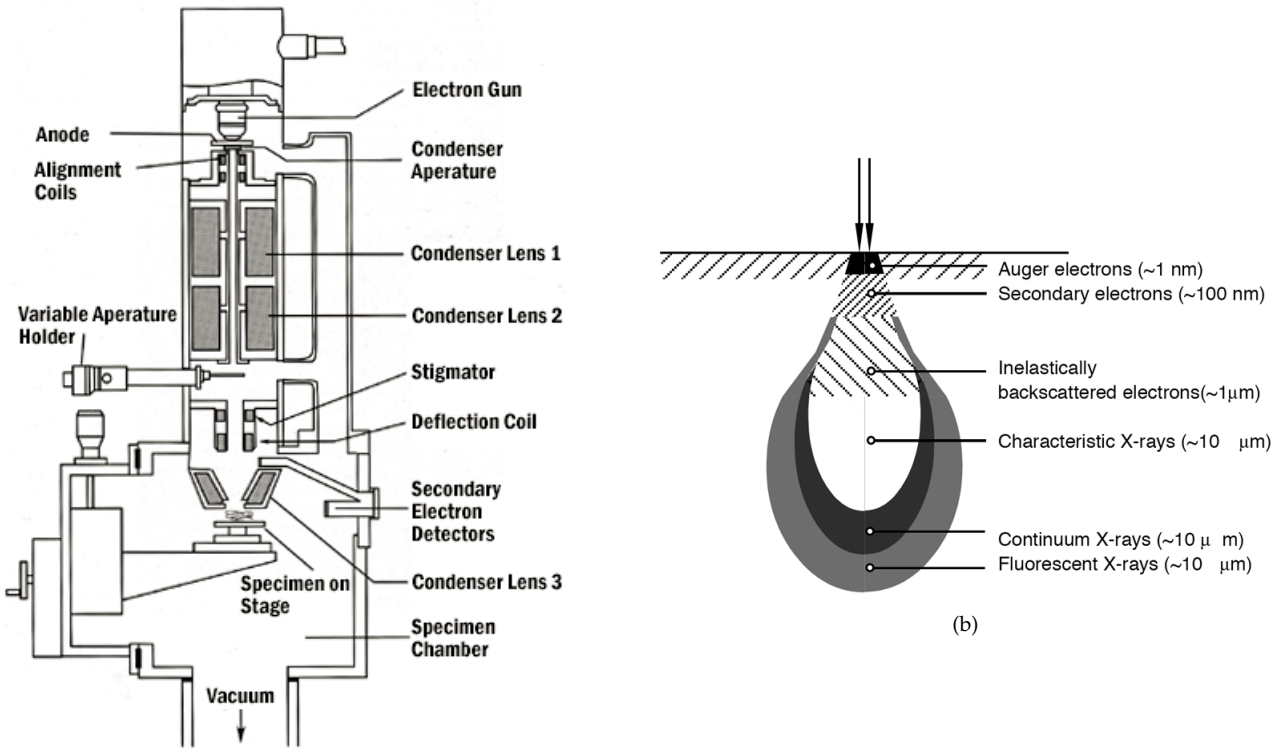


Figure 2.4: a) Schema of a field-emission scanning electron microscope (FE-SEM) used to image the NWs and characterise their morphology [62]. b) Illustration of the interaction peer when primary electrons hit a sample surface [64].

Before doing the SEM measurements, the sample had to be prepared. First, it was cut in pieces, which were placed in dichloromethane to dissolve the membrane. Then, after the complete dissolution of the polymer, the NWs arrays were taken and attached to a Si sample holder using a carbon tape. Let's notice that the cathode was not removed, which was inconvenient when the amount of Cu had to be measured seeing that it increases the error bar of the measurements. Then, the sample was mounted on a $12.5\,\mathrm{mm}$ sample holder before being introduced in a pre-chamber, which was pumped in order not to break the vacuum in the experimental chamber. After this step, the sample was introduced in the experimental chamber, and placed at a working distance of about $8\,\mathrm{mm}$ in our case. To start the observation, a low magnification mode is first chosen in order to find and to focus the spot of the sample to be analysed. Thereafter, the SEM mode is switched on, which allows to see the network of NWs at higher magnifications. For instance, two SEM images taken at different magnifications of CNWS networks are presented on Figure 2.5. As can be seen on Figure 2.5a the network is interconnected, which make it self-standing. Besides, the density of the wires is higher for the template C 20% (Fig. 2.5a) than the C 3% (Fig. 2.5b).

EDX is a chemical analysis that detects the X-rays emitted from deeper in the sample. After the bombardment, electrons are ejected from the atoms, creating vacancies that are filled by electrons in a higher energy state. As a result, X-rays are emitted and their energy comes from the energy difference between the levels concerned during the transition. They also depend on the atomic number of the element they come from. The X-ray detectors measure the relative abundances of X-rays as a function

of their energy. Then, the displayed spectrum, which represents the counts as a function of the energy, helps determine the atomic composition [65, 66].

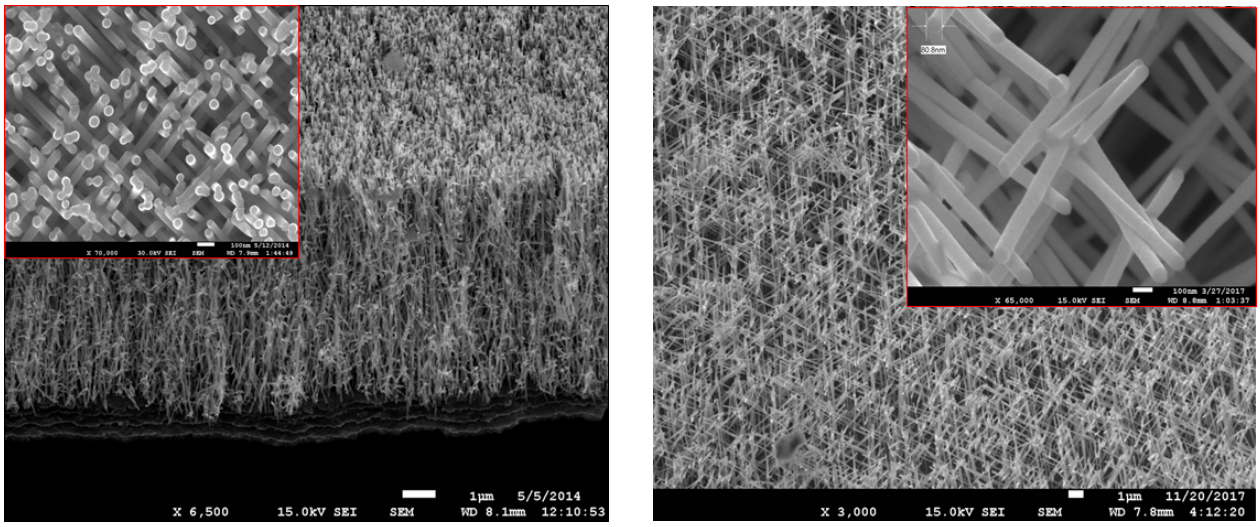


(a) (b)

Figure 2.5: SEM images of CNWs network. a) Lateral and top view of a CNWs network grown in a the template C 20%. C) Top views of a CNWs network grown in a the template C 3%.

In order to obtain the compositions of the specimens, the same procedure as for SEM measurements takes place. The only difference is that after focusing on a desired spot, the image is frozen and the SEM/EDX is switched on. Thereafter, a spectrum of the sample, such as on Figure 2.6, is obtained. The information allows to calculate the atomic percentages of the different species. As can be seen, the peaks of Ni, Cu and Co are very close to each other, which may result in imprecise atomic percentage.

The obtained atomic percentages of different samples are gathered in Tables 2.5 for NiCu alloy and 2.6 for NiCoCu alloy. As can be seen, the first solution gives different compositions depending on the applied potential: about $Ni_{90}Cu_{10}$, $Ni_{95}Cu_5$ and pure Ni for the respective potentials of $-1\,\mathrm{V}$, $-1.1\,\mathrm{V}$ and $-1.9\,\mathrm{V}$. When the potential is decreased, the deposition rate increases, and at $-1.9\,\mathrm{V}$, Ni deposits so fast than no Cu is found. Then, two times more Cu was added in the solution in order to see its influence on the composition. As a result, a composition close to $Ni_{85}Cu_{15}$ was obtained with the same potential of $-1\,\mathrm{V}$, whereas the composition increased by five percent when the potential was switched to $-1.1\,\mathrm{V}$. Then, multilayered CNWs revealed a large amount of Cu, which indicates that the NW layers are thicker than the ferromagnetic ones. That is why, the amount of Cu was reduced to a very low molarity of $2.5\,\mathrm{mM}$. However, the quantity was so low that pure Ni NWs were found. When the amount of Nickel Sulfamate was reduced to $1\,\mathrm{M}$, the atomic percentage of Ni did not drastically changed, only by less than 3%, while the molarity was reduced by a factor of 2.3.

When comparing the two different sources of Ni, for Ni Sulfamate, a very small quantity of Cu was found, and for Ni Sulfate, the content in Cu exceeded 25%. This unexpected results may have been caused by the Cu cathode that was not removed. Afterwards, a new approach consisted in preparing two new solutions with $7.5\,\mathrm{mM}$ and $15\,\mathrm{mM}$ of Cu and compare their results. Regarding the atomic percentage of the samples prepared with those electrolytes, homogeneous CNWs of Ni contains 99% and 97% of Ni. Thus, it can be seen that the composition did not significantly changed, whereas the molarity of Cu doubled. In the case of Cu CNWs, it seems that some Ni is depositing into Cu CNWs, even though the potential is $-0.5\,\mathrm{V}$, at which the sample should be constituted of pure Cu. This may have been caused by a contamination of the solution, which was trapped during the electrodeposition. Moreover, the resolution of the EDX and the proximity of the Cu and Ni peaks may have led to inaccuracies.

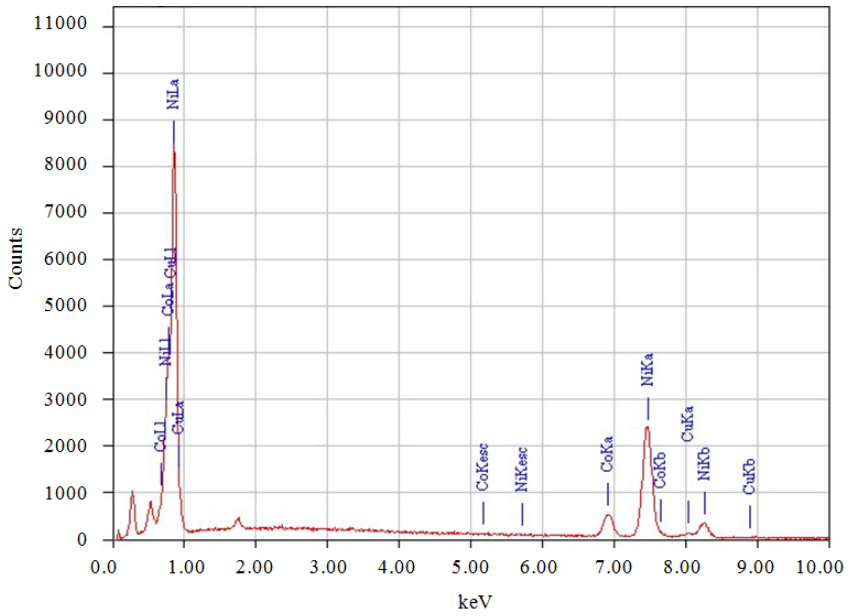


Figure 2.6: Graph of the number of counts as a function of the energy [keV] of a NiCo homogeneous sample obtained during SEM/EDX measurements.

| Electrolyte label | Sample | atomic % of Ni | Template |
|---|---|---|---|
| NiCu(NiSfmt2.3 M Cu25 mM) | Ni ( −1 V) | $90.6 \pm 0.6$ | P 10.1% |
| | Ni (−1.1 V) | $94.8 \pm 1.9$ | |
| | Ni (−1.9 V) | 100 | |
| NiCu(NiSfmt2.3 M Cu50 mM) | Ni (−1 V) | $82.4 \pm 5.5$ | P 10.1% |
| | Ni (−1.1 V) | $90.55 \pm 0.8$ | P 10.1% |
| | NiCu(200ms)/Cu(10s) | $20.85 \pm 2.6$ | C 20% |
| NiCu(NiSfmt2.3 M Cu2.5 mM) | Ni (−1.1 V) | 100 | C 20% |
| NiCu (NiSfmt 1 M Cu 2.5 mM) | Ni(−1.1 V) | $98.7 \pm 1.6$ | C 20% |
| NiCu(Cu2.5 mM) | Ni (−1.1 V) | $72.7 \pm 2$ | C 20% |
| NiCu(Cu7.5 mM) | Ni (−1.1 V) | $98.9 \pm 0.6$ | C 3% |
| | Cu (−0.4 V) | 0 | |
| | Cu (−0.5 V) | 0 | |
| | NiCu(150ms)/Cu(1s) | $92.5 \pm 6.2$ | |
| | NiCu(150ms)/Cu(3s) | $79.1 \pm 2.7$ | |
| | NiCu(150ms)/Cu(6s) | $59.8 \pm 1.2$ | |
| | NiCu(150ms)/Cu(9s) | $64.7 \pm 4.7$ | |
| NiCu(Cu15 mM) | Ni (−1.1 V) | $96.84 \pm 1.1$ | C 3% |
| | Cu (−0.5 V) | $2.8 \pm 0.3$ | |
| | NiCu(136ms)/Cu(1s) | $87.3 \pm 5.3$ | |
| | NiCu(136ms)/Cu(3s) | $68.6 \pm 3.2$ | |

Table 2.5: Atomic percentage of the composition of the NiCu samples obtained with EDX.

The EDX results on multilayered CNWs prepared with the solution NiCu(Cu15 mM) indicate a decrease in the amount of Ni when the electrodeposition time of Cu is gradually increased. As is presented on Figure 2.7, the samples prepared with solution NiCu(Cu7.5 mM) surprisingly indicate a

linear decrease of the Cu deposition times from 1 s to 6 s, followed by an increase. This behaviour is unusual as Cu is deposited during a longer time. It is important to notice too that EDX only gives information on the overall composition and cannot ensure the presence of multilayers. For instance, clusters of Cu or non well defined interfaces may have been formed during the electrodeposition. That is the reason why it cannot be concluded that thicker NM layers are present, even if an electrodeposition time of Cu of 6 s or 9 s is close to what was expected with solution NiCu(Cu7.5 mM). It rather gives an idea about what was deposited in the NWs.

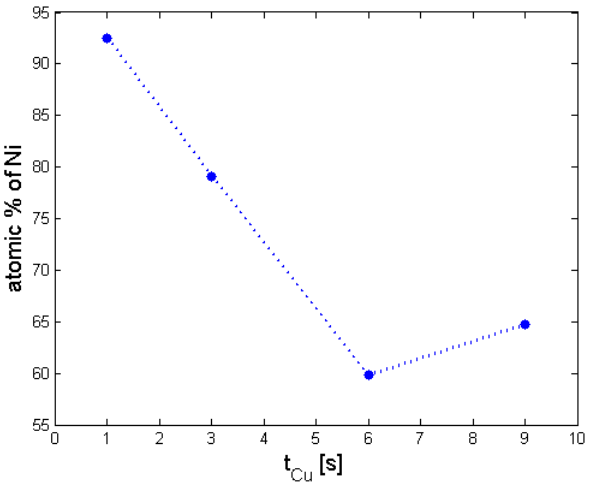


Figure 2.7: Evolution of the atomic percentage of Ni provided by EDX as a function of the electrodeposition time of Cu ($t_{Cu}$ [s]) of the samples prepared with solution NiCu(Cu7.5 mM) on the template C 3%.

Regarding the results of NiCoCu electrolytes, they revealed a low quantity of Cu, comprised between 2% and 5% as well as about six and three times more Co than Ni. Therefore, the composition can be approximated to $Ni_{75}Co_{25}$ and $Ni_{85}Co_{15}$ respectively, which correspond to the desired compositions of NiCo alloys.

| Electrolyte label | atomic % of Ni | atomic % of Cu | atomic % of Co | Template |
|---|---|---|---|---|
| NiCoCu(Co50 mM) | $70.9 \pm 1.2$ | $5.1 \pm 0.4$ | $24 \pm 0.8$ | C20% |
| NiCoCu(Co25 mM) | $84.1 \pm 0.3$ | $2.5 \pm 0.5$ | $13.4 \pm 0.5$ | C20% |

Table 2.6: Atomic percentage of the composition of the NiCoCu samples obtained with EDX.

## 2.3 Magnetic and magneto-transport characterisation techniques

### 2.3.1 Alternating gradient magnetometer (AGM)

The magnetic properties of the samples have been measured by using a MicroMag 2900 Alternating Gradient Magnetometer (AGM) from Princeton Measurement Corporation (PMC), as is shown on Figure 2.8a. The sample is mounted on a rod, the top of which being attached to a piezoelectric element and is placed between two electromagnets poles (Fig. 2.8d). It is therefore subjected to a magnetic field of variable intensity $H$ between $+14$ kHz and $-14$ kHz. In addition, gradient coils produce an alternating excitation field $\frac{dh}{dx}$ of about $40$ Oe/cm and of frequency $\omega$ that reacts with the own magnetic field of the sample (Fig. 2.8e). The operating frequency of the device is between $100$ kHz and $1000$ kHz. The presence of this gradient induces a force $\underline{F_x}$ on the sample, proportional to the amplitude of the gradient and to the magnetisation $\underline{M}$ of the sample and that is given by

$$\underline{F_x} = \underline{M_x}\frac{d\underline{h_x}}{dx} = -\underline{h_x}sin(\omega t). \tag{2.4}$$

The deflection of the cantilever rod is measured by the piezoelectric sensor as an alternating voltage that is recorded (Fig. 2.8b) [67, 68].

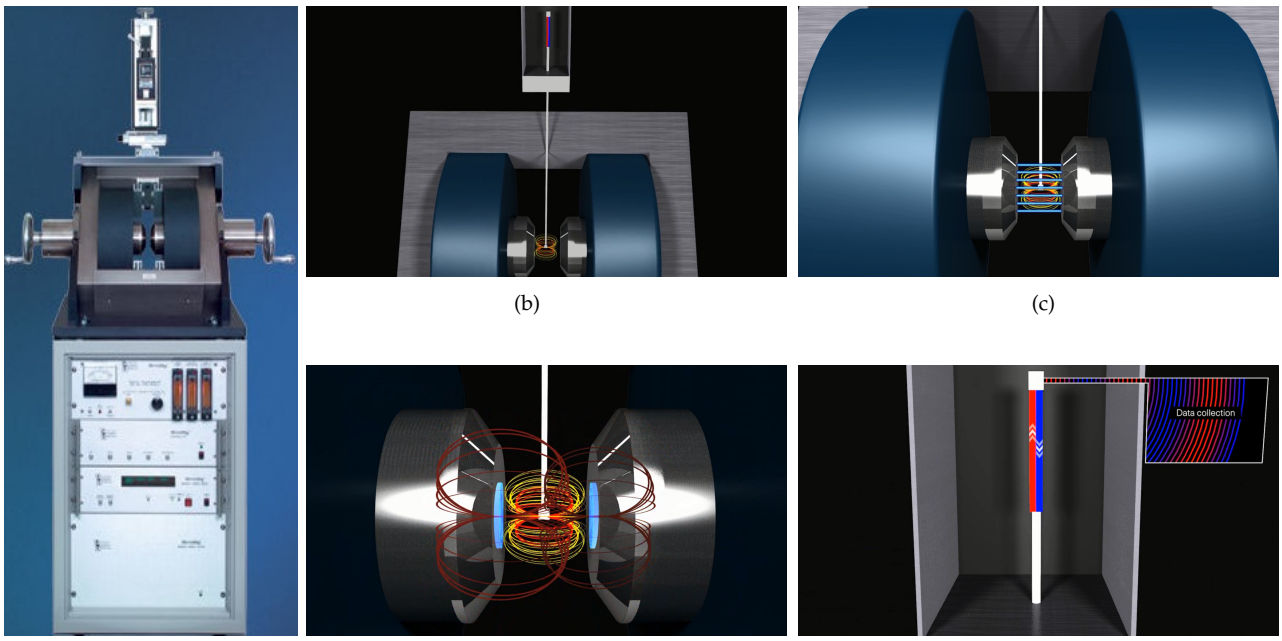


Figure 2.8: MicroMag 2900 alternating gradient magnetometer (AGM) from Princeton Measurement Corporation: a) illustration and working principle. b) The machine is composed of two electromagnets, a sample holder and a piezoelectric bimorph inside a box. c) The sample is located in between the electromagnets, generating a uniform field. d) Two gradient coils in light blue create alternating excitation fields in red, that interact with the magnetic field of the sample in yellow and orange and make the sample oscillate laterally. e) This motion is measured by the piezoelectric sensor as a voltage and the data are collected[69]

The AGM measurements allows to obtain hysteresis loops, first-order reversal curves (FORCs) as well as different remanent magnetisation curves, such as isothermal remanent magnetisation (IRM) and direct-current demagnetisation (DCD). In this case, hysteresis curves were chosen and different pieces of information can be extracted from a measurement, such as the magnetisation curves, the saturation magnetisation, the coercivity, the remanent magnetisation, the squareness ratio and the switching field distribution [70].

In this case, the magnetometer was used at room temperature to obtain the hysteresis loops with its corresponding initial curve, the coercivity and the remanence of the samples. For the measurements, two different probes, which are composed of a piezoelectric bimorph, a polyimide capillary and a glass, were used. The orientation of the glass on which the sample is stuck using a silicon grease allows the measurement in the IP and in the OOP directions. Before any measurement, each probe had to be calibrated with a small Fe ball of a known magnetic moment of $76.2\,\mathrm{memu}$. Then, the samples were cut of the size of the glass without removing the cathode. Indeed, Cu or Au are non magnetic materials and therefore, they will not influence the analysis. During the measurement, the sample is first demagnetised, which means that the magnetic field is progressively lowered until reaching zero. Then, the sample was first magnetised, by increasing the field from $0\,\mathrm{Oe}$ up to a field $H_{max} = 10\,\mathrm{kOe}$. After the first magnetisation, the field is switched from $+H_{max}$ to $-H_{max}$ and then, from $-H_{max}$ to $+H_{max}$.

### 2.3.2 Magneto-transport measurements

For the purpose of measuring the magneto-transport properties, the resistance of the samples was measured under a varying magnetic field, from $10\,\mathrm{kOe}$ to $-10\,\mathrm{kOe}$ and then back to $10\,\mathrm{kOe}$. This latter was generated by a Lake Shore electromagnet and measured thanks to a Lake Shore Hall probe. As for the sample, it was crossed by an alternating current, generated by an alternating voltage and an external resistance that has to be typically 1000 times larger than the resistance of the sample. This is to measure the variation of the sample resistance and not the variation of the current. Besides, that current has to be low, in order not to damage the sample. The current flowing through the sample

is controlled by a Lock-in amplifier from Signal Recovery and the output voltage is measured by a Keithley Multimeter. The circuit is presented on Figure 2.9.

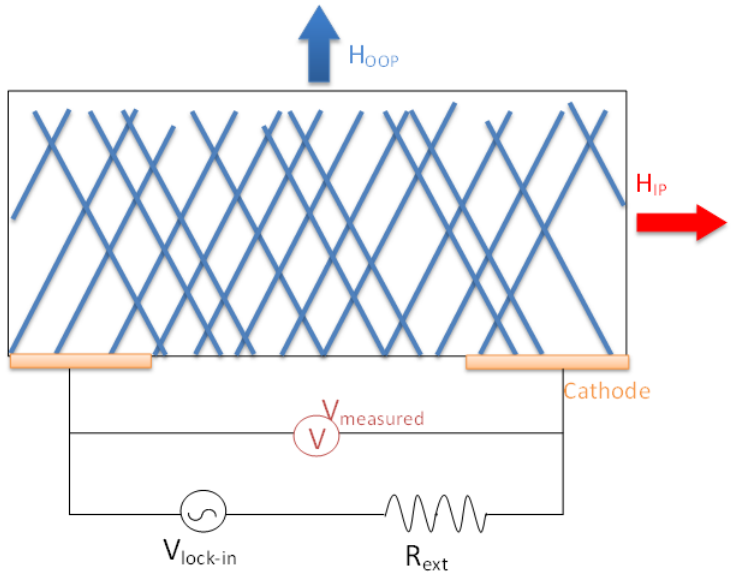


Figure 2.9: Illustration of the circuit to perform the mangeto-transport measurements. After the etching of the sample, which removed a strip of the cathode, the alternating current is injected by a lock-in. It enters the sample by one side of the etched cathode and goes out by the other side. The current is generated by the coupling of an alternating voltage $V_{lock-in}$ and an external resistance $R_{ext}$, the value of which being 1000 larger than the sample resistance. A voltmeter is connected in parallel to measure the difference of potential $V_{meas}$ at the terminals of the sample. The IP and OOP directions of the external magnetic field are represented by the red and blue arrows respectively.

The measurements were performed at room temperature and ambient pressure and also at low temperature. To work at low temperatures, the system had first to be cooled. The first step was to pump the air inside the column for ten minutes. Then, overpressurised Helium (He) was injected to mix it with air before pumping one last time for 15 minutes. The mixing is performed to ensure that all the air is removed. Indeed, when cooling down the system, it is preferable to avoid any formation of ice. After the vacuum is created inside the chamber, an overpressurised He is once again injected in the chamber and a CTI-Cryogenics 8200 Compressor is used to cool down the system. The He inside the chamber is successively compressed and expanded to reduce the temperature of a cold finger. A heating resistance regulates the temperature with a proportional–integral–derivative (PID) controller. The cold finger is in contact with the metallic sample holder and the temperature of these two elements is measured. Once a stable value of about $12\,\mathrm{K}$ is reached, the same measurement procedure can be performed.

Before any measurement, the samples had to be connected. For that purpose, two different configurations have been used. For the first one, half a piece of a circular sample was placed under a mask (Fig. 2.10a) and etched via an Argon (Ar) plasma etching under $5\,\mathrm{mTorr}$ and an acceleration power of 80 Watt that removed a part of the cathode. The template C 20% was etched during 26 minutes and two to five additional minutes were added if the cathode was not effectively removed. For the template C 3%, different cycles of etching spaced by resting were needed to avoid damaging the samples: first, two cycles of ten minutes of etching and ten minutes of resting, followed by two cycles of five minutes and perhaps three to five minutes of additional etching time. At the end, a thin opening was etched, as is shown on Figure 2.10b. The etching allowed to create a circuit in which a current can flow from one side of the cathode to the other and go through the NW networks, as can be observed on Figure 2.9. In the second configuration, the sample was not etched but the wires were grown until overfilling and then connected by the top of the sample by depositing a small Cr/Au cathode, which is much smaller than the sample size. With this configuration, the current arrives at the top of the CNWs, go through the network and leaves at the bottom cathode.

(a)

(b)

Figure 2.10: Pictures of a) the mask used to etch the samples and b) half an electrodeposited sample before (left) and after etching (right).

Then, the sample was mounted on a sample holder and stuck to it using an isolating grease. Additionally, Cu wires were welded to chip nodes and connected on each side of the opening for the first configuration (Fig. 2.11b) or on the top of the deposited cathode (Fig. 2.11a) with Ag paint. Afterwards, the chip was placed on the sample holder at the end of a rod and introduced in a chamber placed between the electromagnets. The rod can be rotated so that the sample can be measured in IP and in OOP directions. The assembly allows to perform a pseudo four-contacts measurement. This correctly evaluates the resistance because the sample resistance is much larger than the one of the Ag paint and the Cu wires.

(a)

(b)

Figure 2.11: Pictures of the two different ways used to mount the samples on a chip: a) or b) by the top or the sample.

As was already explained for PNWs, the OOP direction is well defined. Indeed, it is perpendicular to the membrane surface, and is therefore orientated with an angle of $\pm 25^{\circ}$ with respect to the length of the wires. However, this is not similar for the IP direction which can take any orientation parallel to the sample surface. Besides, before etching, the samples were randomly cut and afterwards, they were not attached to the chip the exact same way. Thus, the measured orientation differs from one sample to the other.

During the magneto-transport measurements of CNWs, different elements may cause a diminution of the GMR. The first one is a residual cathode that could not be successfully removed during the etching. Indeed, the verification of the cathode removal is performed with the human eyes, so that a thin layer may remain without noticing. As is shown on Figure 2.12, in this case the current will flow through the CNWs network as well as through the cathode. As a result, a parallel circuit is obtained, for which the resistance is given by

$$\frac{1}{R_{sple}} = \frac{1}{R_{CNWs}} + \frac{1}{R_{cath}} \tag{2.5}$$

where $R_{sple}$ is the resistance of the sample, $R_{CNWs}$ is the resistance of the CNWs arrays and $R_{cath}$ is the resistance of the residual cathode. When the residual layer in not removed, $R_{cath}$ is not infinite anymore, which cause $R_{sple}$ to go down. In addition, if instead of having an alloy in the NWs, core-shells are presents, another parallel current is added.

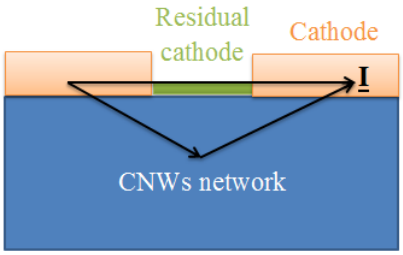


Figure 2.12: Schema of a sample for which a residual cathode remains after the etching.

The second source that can be responsible for a diminution of the GMR is an additional resistance due to crossing zones, defects, contacts between the wires and the cathode, contacts between the cathode and the NWs and splits of wires. Crossing zone effect can be reduced by decreasing the porosity, as already discussed in Section 2.1.1, while defects are unavoidable in electrodeposited nanowires and can lead to GMR ratio reduction. In contrast, the CNW network architecture allows an easy measurements where the cathode serves as electrodes for the electrical measurement and ensure low contact resistances, in contrast with PNWs.

# Chapter 3

# Results and discussion

The objective of this work is to find systems showing the most isotropic magnetic behaviour coupled with the highest GMR ratio. Therefore, the influence of changing the electrodeposition conditions will be examined for each series. In this chapter, the results of the magnetic and magneto-transport measurements will be presented and discussed. First, Ni/Cu multilayered CNWs will be looked at and then, the study will be focused on NiCo/Cu multilayered CNWs.

## 3.1 Ni/Cu multilayered nanowires

In order to study Ni/Cu NW arrays, a PC template with parallel pores has been used. The reason is that PNWs have well defined easy and hard magnetic directions. Then, switching from a parallel to a crossed template should reduced the anisotropic behaviour of a sample prepared with identical parameters. This is because the wire axis of CNWs is neither parallel nor perpendicular to the applied magnetic field $\underline{H}$ (see section 2.3.2).

### 3.1.1 Study of parallel nanowires

As was mentioned in Section 2.1.2, this thesis started with the calibration of the solution NiCu(NiSfmt2.3 M Cu25 mM) on PNWs. After finding the potential of $-1\,\mathrm{V}$ for Ni that gives a composition of $Ni_{90}Cu_{10}$, multilayered were prepared. To deposit Cu, a potential of $-0.5\,\mathrm{V}$ was used and fixed to $10\,\mathrm{s}$. As for Ni, its electrodeposition time was varied between $100\,\mathrm{ms}$ and $500\,\mathrm{ms}$.

The hysteresis loops of the homogeneous sample as well as three of the multilayered PNWs are presented on Figure 3.1. As can be observed, the OOP direction is the easy direction of the homogeneous PNWs ( Fig. 3.1a). Then, when Ni layers are deposited for $500\,\mathrm{ms}$, the curves get less tilted and more squared, especially for the OOP direction (Fig. 3.1b). Thus, the system tends to be more isotropic. This is due to the fact that the formation of multilayers generates and additional interaction between the layers, besides the shape anisotropy and the interaction between NWs. That is the reason why when $t_{Ni}$ is reduced, the IP and the OOP curves get closer to each other and the system is more isotropic, as is presented on Figure 3.1c. At some point, the size of the magnetic layers are such that their diameter is larger than their length. Consequently, the easy axis switches from the OOP direction to the IP direction. This phenomenon is depicted on Figure 3.1d and the evolution of the system towards a more isotropic behaviour should be marked by increasing values of normalised remanence and coercivity. As is shown on Figure 3.2, this is the case for the IP direction but not for the OOP direction . However, the values are in the same range and therefore, the evolution is not significant. It can be concluded that the parameters giving the most isotropic system proved to be an electrodeposition of Ni of $100\,\mathrm{ms}$.

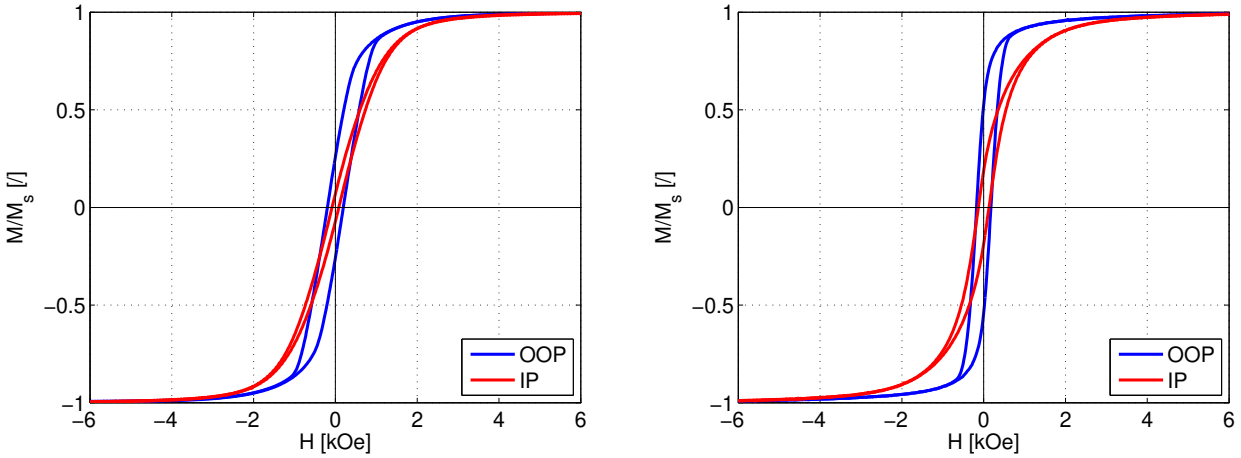


(a) HCNW

(b) Ni(500 ms)/Cu(10 s)

(c) Ni(300 ms)/Cu(10 s)

(d) Ni(100 ms)/Cu(10 s)

Figure 3.1: Hysteresis loops of the reference sample and multilayered PNWs prepared with solution NiCu(NiSfmt2.3 M Cu25 mM) on the template P 10.1%. The magnetic field was applied in the IP (red) and in the OOP (blue) directions.

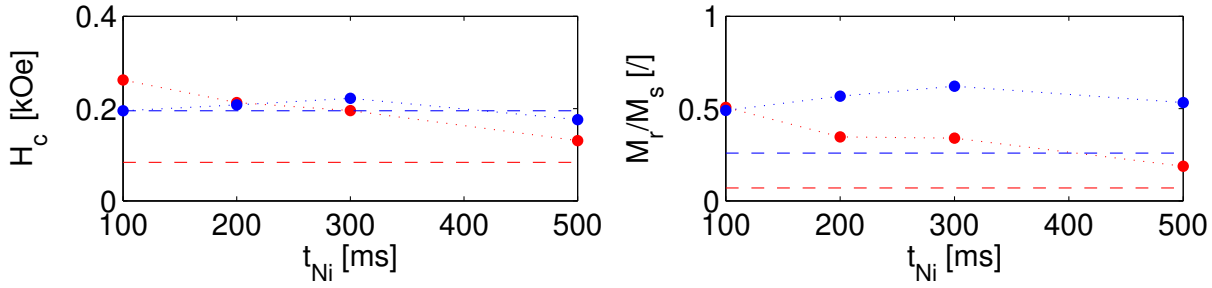


Figure 3.2: Evolution of the coercivity ($H_c$ [kOe]) and normalised remanence ($M_r/M_s$ [/]) with the electrodeposition time of Ni ($t_{Ni}$ [ms]). The homogeneous and multilayered PNWs were prepared with solution NiCu(NiSfmt2.3 M Cu25 mM) on the template P 10.1% and $t_{Cu}$ was fixed to 10 s. The horizontal dashed lines represent the values of the homogeneous sample. The samples were measured in the IP (red) and the OOP (blue) directions.

Then, when two times more Cu was added in the solution, two different potentials were tried on PNWs and a multilayered sample was prepared too. This latter has Ni and Cu layers respectively deposited for 100 ms and 10 s. The magnetic measurement reveals a similar behaviour compared to the equivalent sample prepared with the solution NiCu(NiSfmt 2.3 MCu 25 mM). As is indicated in Table 3.1, the two Ni(100 ms)/Cu(10 s) samples have the same normalised remanence and in both directions. Besides, the coercivity of this sample is slightly higher. However, the difference between the values is negligible. Furthermore, the behaviour of the hysteresis loop is similar to the curve of the

sample Ni(100 ms)/Cu(10 s) with less Cu in the alloy on Figure 3.1d. Thus, doubling the amount of Cu in the solution does not impact the isotropic behaviour of the sample. Therefore, the same parameters were tested on CNWs arrays.

| Solution | $\frac{M_{r,IP}}{M_s}$ [%] | $H_{c,IP}$ [kOe] | $\frac{M_{r,OOP}}{M_s}$[%] | $H_{c,OOP}$ [kOe] |
|---|---|---|---|---|
| NiCu(NiSfmt2.3 M Cu25 mM) | 0.51 | 0.26 | 0.49 | 0.2 |
| NiCu(NiSfmt2.3 M Cu50 mM) | 0.54 | 0.36 | 0.46 | 0.28 |

Table 3.1: Normalised remanence $M_r/M_s$ [/] and coercivity $H_c$ [kOe] of NiCu(100 ms)/Cu(30 s) samples prepared by means of solutions NiCu(NiSfmt2.3 M Cu25 mM) and NiCu(NiSfmt2.3 M Cu50 mM) on the template P 10.1%. The magnetic field was applied in the IP and in the OOP directions.

### 3.1.2 Study of crossed nanowires on a high porosity template (20%)

**Optimisation of the solution NiCu(NiSfmt2.3 M Cu50 mM)**

When switching to the template C 20%, the solution NiCu(NiSfmt2.3 M Cu50 mM) was used and the electrodeposition times for Ni and for Cu were $t_{Ni} = 100, 200, 300$ ms and $t_{Cu} = 10$ s, respectively. As is shown, the system is anisotropic when the Ni layers are deposited during 300 ms (Fig. 3.3a) and the easy direction is the IP direction. Then, when the electrodeposition time is lowered by 100 ms, the loops in IP and OOP directions overlap (Fig. 3.3b). If $t_{Ni}$ is further decreased, the system is slightly less isotropic and the IP direction is still the easy axis. The obtained magnetisation curve of this sample is similar to Ni(100 ms)/Cu(10 s) deposited on a parallel template on Figure 3.1d. The only difference is that the IP normalised remanence is slightly lower and equals 0.46. This evolution is unexpected. Indeed, it could initially be conceived that the OOP direction would have been the easy direction of thicker magnetic layers. Then, decreasing the electrodeposition time of Ni would induce a switch of easy axis. Or, another possibility could be the observation of a system getting more and more anisotropic in IP direction, because of dominant shape anisotropy of the thinner layers. However, what is observed is an isotropic behaviour but no switch in the easy direction.

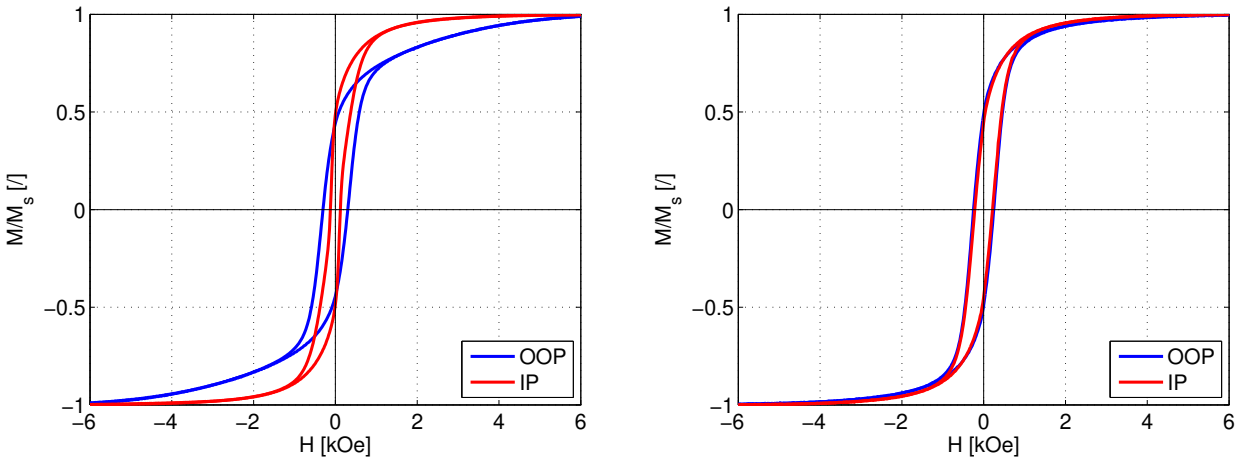


(a) Ni(300 ms)/Cu(10 s)

(b) Ni(200 ms)/Cu(10 s)

Figure 3.3: Hysteresis loops of multilayered CNWS prepared with solution NiCu(NiSfmt2.3 M Cu50 mM) on the template C 20%. The samples were measure in the IP (red) and in the OOP direction (blue) directions.

It can be seen on Figure 3.4 that the normalised remanence lays between 0.43 and 0.49. Besides, lower deposition times for Ni show that the coercivity is the same for both directions and that a longer $t_{Ni}$ increases the difference between $H_c$. Thus, a decrease of the electrodeposition time of Ni favours an isotropic behaviour.

Although isotropy is observed in the magnetic measurements, the transport measurements denies the formation of multilayers and rather indicate the presence of Ni clusters, which are marked by an

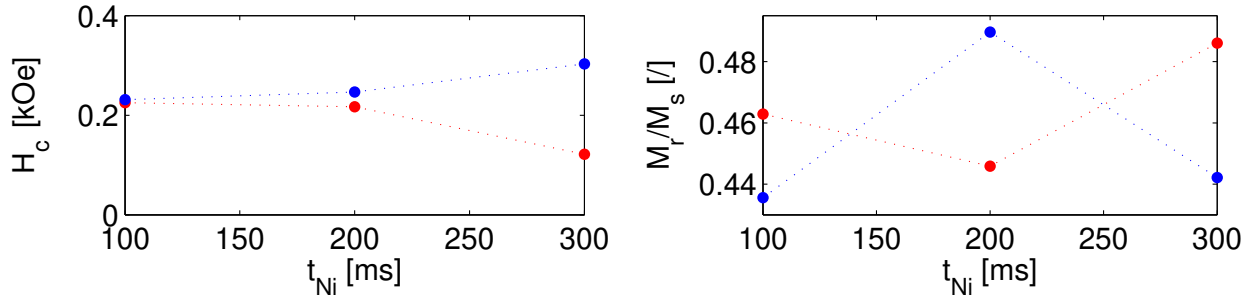


Figure 3.4: Evolution of the coercivity ($H_c$) and normalized remanence ($M_r/M_s$) with the electrodeposition time of Ni ($t_{Ni}$). The reference sample and multilayered CNWs were prepared with solution NiCu(NiSfmt2.3 M Cu50 mM) on the template C 20% and $t_{Cu}$ was fixed to 10 s. The samples were measure in the IP direction (red) and in the OOP direction (blue).

almost isotropic and quite large resistance curve. This could be caused by the larger quantity of Cu in the solution than the previous electrolyte. So, Cu deposits faster and thicker non-magnetic layers are formed, as well as less defined FM layers. As a result, a combination of high Cu content in the solution with smaller electrodeposition time of Ni reinforces the formation of clusters over multilayers. This might be the reason why first, the AGM indicates the formation of multilayers when Ni is deposited for 300 ms. And then, a further decrease of the size of the FM layers generates an isotropic behaviour whereas the layers are thinner. Thus, because of the encountered phase separation issues as well as the SEM results indicating a greater amount of Cu rather than Ni, the amount of Cu was declined to a content of 2.5 mM of Cu.

**Optimisation of the solution NiCu(NiSfmt2.3 M Cu2.5 mM)**

During the electrodepositions with the electrolyte NiCu(NiSfmt2.3 M Cu2.5 mM), the time of the Ni layers was increased to 300 ms to ensure the formation of multilayers. In addition, the drop in Cu content causes a slower deposition of this specie and therefore, $t_{Cu}$ was risen and varied between 20 s and 30 s.

The AGM results for the homogeneous sample and a multilayered CNW sample are presented on Figure 3.5a and 3.5c. They show that forming multilayers makes the system less anisotropic. So, the system saturates faster when multilayers are formed, which is due to the dipolar interaction between layers leading to an additional contribution to the magnetostatic energy along the NW axis.

The coercivity and normalised remanence for both directions are shown in Table 3.2. The coercivity of both multilayers is almost the half of the one of the homogeneous CNW (HCNW) sample in both directions. Besides, $H_c$ does not significantly vary between an electrodeposition time of 20 s and 30 s. As for the normalised remanence, the values are similar in IP and rise in OOP. The fact that there is so little difference when the electrodeposition time of Cu is increased may be explained by the concentration of Cu in the solution. Indeed, the molarity of Copper Sulfate was drastically dropped, so that Cu deposits very slowly and has not enough time to significantly thickens the NM layers.

| Sample | ΔMR[%] | $\frac{M_{r,IP}}{M_s}$ [%] | $H_{c,IP}$ [kOe] | $\frac{M_{r,OOP}}{M_s}$[%] | $H_{c,OOP}$ [kOe] |
|---|---|---|---|---|---|
| HCNW | 0.71 | 0.42 | 0.48 | 0.59 | 0.49 |
| Ni(300ms)/Cu(20s) | 1.1 | 0.35 | 0.24 | 0.47 | 0.26 |
| Ni(300ms)/Cu(30s) | 0.99 | 0.32 | 0.22 | 0.55 | 0.26 |

Table 3.2: Normalised remanence $M_r/M_s$ [/], coercivity $H_c$ [kOe] and ΔMR [%] of the reference sample and the CNWs samples prepared using solution NiCu(NiSfmt2.3 M Cu2.5 mM) on the template C 20%. The magnetic field was applied in the IP and the OOP directions.

When analysing the resistance curves of the homogeneous sample and a multilayered sample on Figures 3.5b and 3.5d, it can be seen that, at saturation, the resistance is minimum. This is due

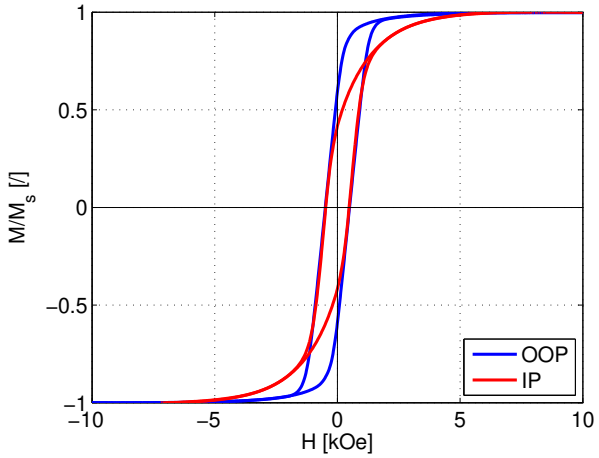


(a) HCNW

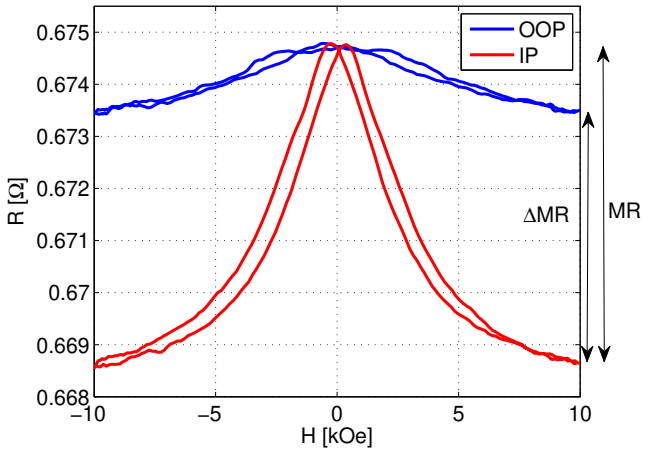


(b) HCNW

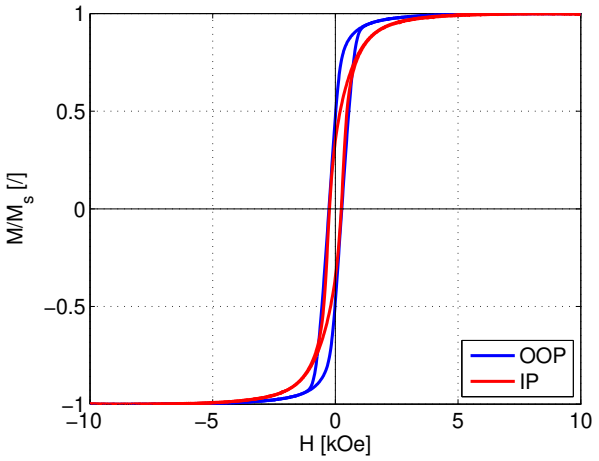


(c) NiCu(300 ms)/Cu(20 s)

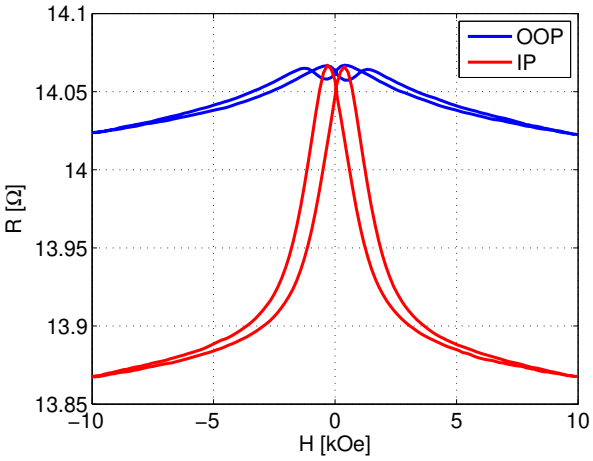


(d) NiCu(300 ms)/Cu(20 s)

Figure 3.5: a, c) Hysteresis loops and b, d) resistance curves of a homogeneous and multilayered CNW networks prepared with solution NiCu(NiSfmt2.3 M Cu2.5 mM) on the template C 20%. The electrodeposition times of the multilayers were 300 ms for Ni and 20 s for Cu. The MR of the homogeneous sample is equal to 0.92% and the ΔMR is equal to 0.71%. For the multilayered CNW sample, ΔMR is equal to 1.1%. The samples were measure in the IP direction (red) and in the OOP direction (blue).

to the parallel alignment of the multilayer magnetisation, as was explained in Section 1.2. Then, the resistance in the IP direction increases to reach a maximum when the magnetisation of the sample reaches a larger degree of anti-parallelism. This corresponds to a magnetic field with a value close to $H_c$. Moreover, further decreasing the external field, the resistance again decreases and reaches the minimum. The behaviour is symmetric when the field goes from $-10\,\mathrm{kOe}$ to $10\,\mathrm{kOe}$. In the OOP direction, the resistance starts to increase and then drops, when reaching a value close to $H_c$. Afterwards, the resistance increases, reaches a maximum and then again goes towards the minimum of resistance. This behaviour corresponds to AMR, as was detailed in Section 1.4.2. Besides, a gap can be seen between the values of minimum of resistance in the IP ($R_{min,IP}$) and OOP ($R_{min,OOP}$) directions on Figure 3.5b. This difference is also due to the AMR effect. Therefore, it could be interesting to compare this contribution between the reference sample and the multilayers because a dominant AMR effect is observed for the multilayered sample (Fig. 3.5d). However, the MR calculated for the homogeneous sample by Equation 1.29 can not be used. Indeed, the value of $R_{max}$ for the multilayers is due to the GMR effect. Therefore, to compare the samples, a factor that is independent of the GMR must be considered. One way to do that is by approximating $R_{max}$ by $R_{min,OOP}$ and defining a ΔMR by

$$\Delta MR = \frac{R_{min,OOP} - R_{min,IP}}{R_{min,OOP}}. \tag{3.1}$$

As can be seen on Figure 3.5b, the difference between $R_{max}$ and $R_{min,OOP}$ is really small, of about $0.001\,\Omega$. Therefore, ΔMR approximates the MR of the reference sample, following the same tendency, but still slightly underestimates it.

The values of the ΔMR are gathered in Table 3.2. The MR of the homogeneous sample is equal to 0.92%. Therefore, it can be seen that the ΔMR of the homogeneous sample is lower than its MR. Moreover, the values of ΔMR for the multilayered CNW samples are closer to the MR of the reference sample rather than its ΔMR. This is surprising as these values are expected to be lower than the ΔMR of the reference sample. This can be due to a low quality of the homogeneous sample, as is shown by a noisy curve on Figure 3.5b. It might indicate damages of the sample during the fabrication or a residual cathode. However, the values indicate dominant AMR in the multilayered CNW arrays, which is observed on Figure 3.5d.

So, it can be concluded that increasing the electrodeposition time of Cu results in similar magnetic and magneto-transport properties. Besides, the observation of dominant AMR indicates that the multilayers are not well defined, maybe because of the very low quantity of Cu in the solution, and that clusters of Cu are rather found in the NWs.

**Comparison between Nickel Sulfamate and Nickel sulfate**

Because of the hypothetical presence of clusters, it was decided to investigate the difference between Nickel Sulfamate and Nickel Sulfate. Indeed, both solutions are found in the literature to deposit Ni. However, researchers usually make use of Nickel Sulfamate in order to fabricate core-shell nanowires. This is because of the phase separation of the two species and the fact that Ni is stabilised, allowing the synthesis of nanotubes. Moreover, the concentration in Ni was reduced to $1\,\mathrm{M}$ to avoid instabilities of the solution whereas the one of Cu was kept to $2.5\,\mathrm{mM}$ to try to avoid the formation of Ni clusters. In addition, following the magneto-transport results with the previous electrolyte, the electrodeposition time of Ni was decreased from $300\,\mathrm{ms}$ to $75\,\mathrm{ms}$ in order to reduce the AMR ratio and have dominant GMR. Besides, $t_{Cu}$ was fixed to $30\,\mathrm{s}$ because it gave slightly lower ΔMR, although there is no significant difference decreasing this time.

First, if the magnetisation curves of the homogeneous samples prepared with the two electrolytes NiCu(NiSfmt$2.3\,\mathrm{M}$ Cu$2.5\,\mathrm{mM}$) (Fig. 3.5a) and NiCu(NiSfmt$1\,\mathrm{M}$ Cu$2.5\,\mathrm{mM}$) (Fig. 3.6a) are compared, no difference is seen in the overall behaviour of the curve. The easy direction remains the OOP direction and the values of the remanence and the coercivity are really similar. So, there is no difference in the magnetic behaviour of homogeneous CNWs arrays when the concentration of Ni goes from $2.3\,\mathrm{M}$ to $1\,\mathrm{M}$.

Then, the hysteresis loops of the two homogeneous samples prepared with Nickel Sulfamate and Nickel Sulfate are presented on Figures 3.6a and 3.6c. It is shown that both curves are anisotropic. However, a slight difference can be seen between the coercivity in the IP direction. This is demonstrated on Figure 3.7 by the horizontal dashed lines. The difference between the IP and OOP direction of the homogeneous samples is larger with the solution NiCu(Cu$2.5\,\mathrm{mM}$). Different possibilities could justify this behaviour. First, because of the random distribution of the pores, the porosity of the measured pieces may be different. Therefore, the interaction between wires is impacted and changes the magnetostatic anisotropy. Another possible reason might be because of phase separation. As a result, some clusters might be deposited inside the Ni wires but differently in each solution.

The resistance curves of the homogeneous samples are presented on Figures 3.6b for Nickel Sulfamate and 3.6d for Nickel Sulfate. The behaviour of the resistance is similar to Fig. 3.5b and shows AMR. This is normal because there are no multilayers. The MR has been calculated for both samples. It is equal to 0.68% for Nickel Sulfamate and 1.7% for Nickel Sulfate. Unsurprisingly, lower values are obtained for the ΔMR and are equal to 0.46% and 1.31%, respectively. So, both the magnetic and magneto-transport measurements show discrepancies between the two solutions. In this case, the

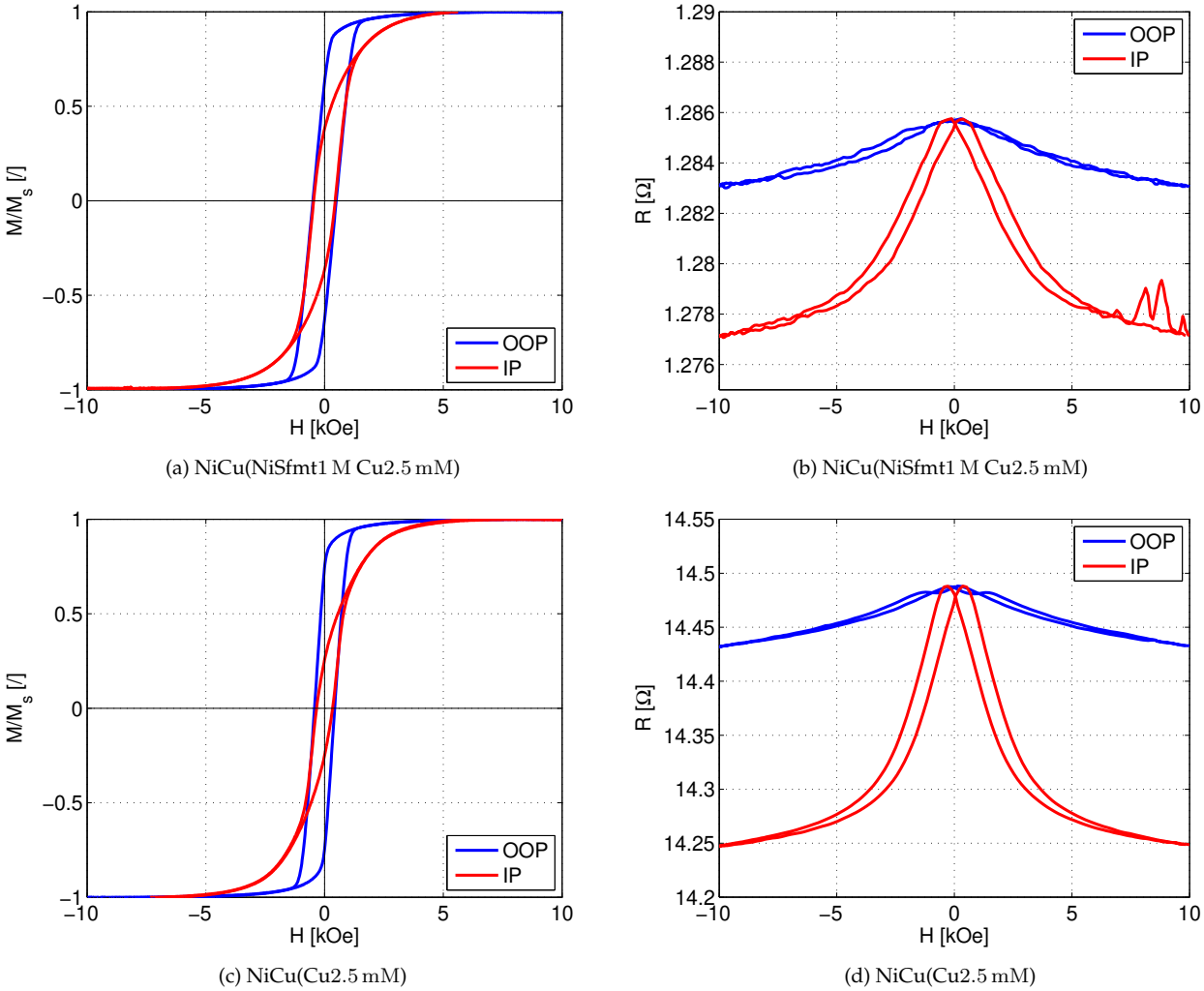


(a) NiCu(NiSfmt1 M Cu2.5 mM)

(b) NiCu(NiSfmt1 M Cu2.5 mM)

(c) NiCu(Cu2.5 mM)

(d) NiCu(Cu2.5 mM)

Figure 3.6: a, c) Hysteresis loops and b, d) resistance curves of homogeneous CNWs prepared with solutions NiCu(NiSfmt1 M Cu2.5 mM) and NiCu(Cu2.5 mM) on the template C 20%. The samples have a MR of b) 0.68% and d) 1.7% and a ΔMR of b) 0.46% and d) 1.31%. The magnetic field was applied in the IP direction (red) and in the OOP direction (blue).

difference may be due to the fact that one sample has been damaged during etching. Besides, the etching is not always perfectly performed. For one sample, the cathode may have been completely removed whereas for the other, a residual layer may still be present. This might also explain why the resistance of both sample is different whereas they should give the same values.

When multilayers are formed, it can be seen on Figure 3.8a that the magnetic curves show a more isotropic behaviour in comparison with the homogeneous samples and that the easy axis stays the OOP direction. This is indicated on Figure 3.7 by higher values of normalised remanence and coercivity for the homogeneous arrays. This tendency is observed for both samples NiCu(300ms)/Cu(30s) deposited with the solutions NiCu(NiSfmt1 M Cu2.5 mM) and NiCu(Cu2.5 mM) as they have the same hysteresis loop. Next, Ni layers deposited for half this time show a different behaviour. On the one hand, the easy axis switches from the OOP to the IP direction with Nickel Sulfate (Fig. 3.9a), which is marked by the overtaking of the normalised remanence in IP direction (Fig. 3.7). On the other hand, the system is isotropic with Nickel Sulfamate (Fig. 3.8c). This should be indicated by a decrease of the normalised remanence and coercivity. Although this is not observed, the values stay in the same range and that is why this can be considered as insignificant. Thus, these observations might indicate that the thickness and diameter of the multilayers would be of the same size on Figure 3.8c whereas the thickness would be smaller on Figure 3.9a. Therefore, multilayers could be formed for both solutions and Ni deposits more slowly when Nickel Sulfate is used rather than Nickel Sulfamate. It has to be mentioned that the samples deposited for 75 ms were measured. However, the hysteresis loop could only be obtained for

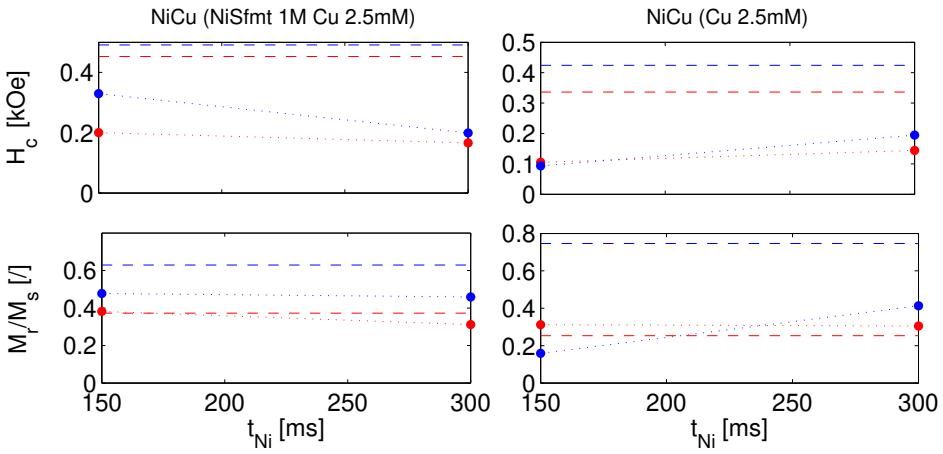


Figure 3.7: Evolution of the coercivity ($H_c$ [kOe]) and normalised remanence ($M_r/M_s$ [/]) with the electrodeposition time of Ni ($t_{Ni}$ [ms]). The reference sample and multilayered CNWs were prepared with solutions NiCu(NiSfmt1 M Cu2.5 mM) and NiCu(Cu2.5 mM) on the template C 20% and $t_{Cu}$ was fixed to 10 s. The horizontal dashed lines represent the values of the homogeneous sample. The samples were measure in the IP (red) and in the OOP directions (blue).

Nickel Sulfate and a very noisy isotropic resistance curve was found, indicating very few amount of magnetic materials in these samples.

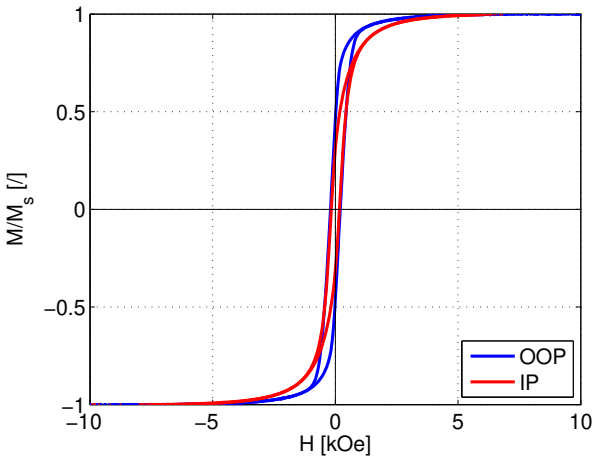


(a) Ni(300ms)/Cu(30s)

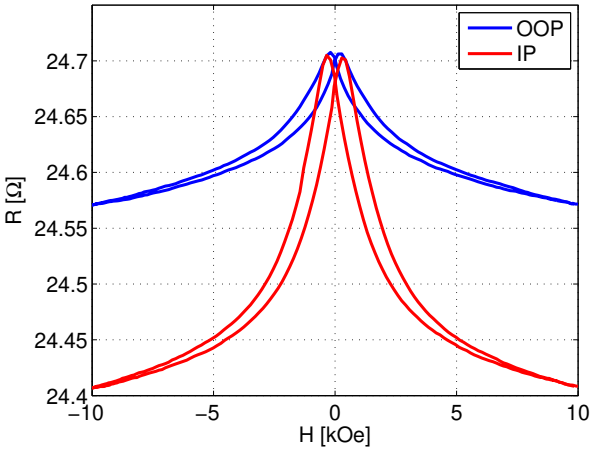


(b) Ni(300ms)/Cu(30s)

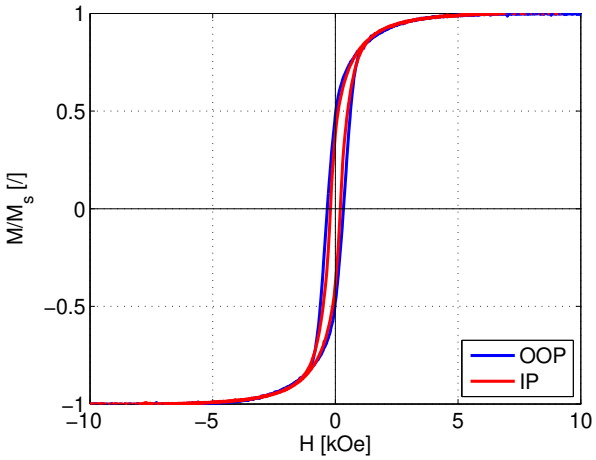


(c) Ni(150ms)/Cu(30s)

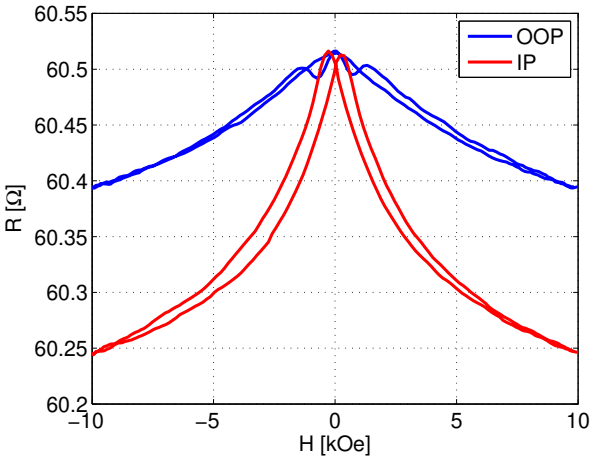


(d) Ni(150ms)/Cu(30s)

Figure 3.8: a, c) Hysteresis loops of multilayered CNWs and b, d) the corresponding resistance curves prepared with solution NiCu(NiSfmt1 M Cu2.5 mM) on the template C 20%. The ΔMR is equal to b) 0.65%, d) 0.25%. The magnetic field was applied in the IP (red) and in the OOP directions (blue).

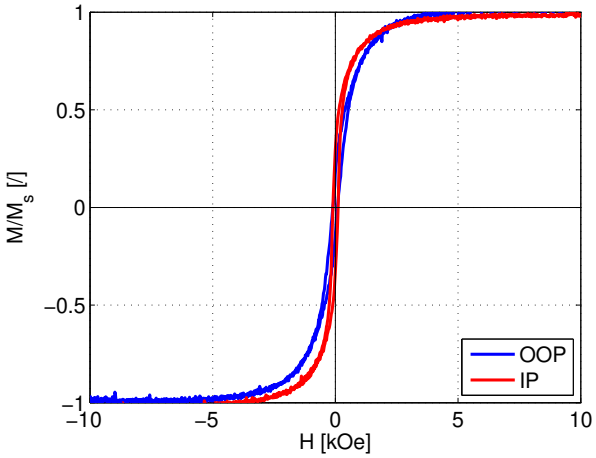


(a) Ni(150ms)/Cu(30s)

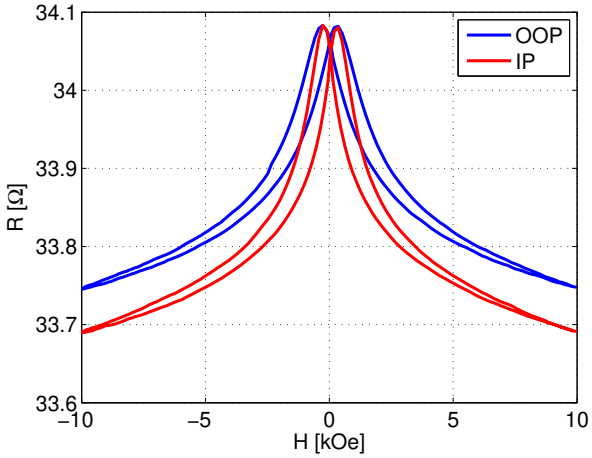


(b) Ni(150ms)/Cu(30s)

Figure 3.9: a) Hysteresis loop and b) the corresponding resistance curve of a multilayered CNW sample prepared with solution NiCu(Cu2.5 mM) on the template C 20%. The GMR is equal to 1.16% and the ΔMR is equal to 0.17%. The magnetic field was applied in the IP direction (red) and in the OOP direction (blue).

Regarding the resistance curves for Nickel Sulfamate on Figures 3.8b and 3.8d and for Nickel Sulfate on Figure 3.9b, it can be seen that the only sample showing dominant GMR is the sample NiCu(150 ms)/Cu(30 s) obtained with Nickel Sulfate. Indeed, a peak is seen in both directions and the difference between $R_{min,OOP}$ and $R_{min,IP}$ is small. The value of the GMR measured in the IP direction ($GMR_{IP}$) is equal to 1.16% and it gives a upper limit to the GMR ratio. For the rest of this work, the value of the GMR ratio will be given for the IP direction. As was previously observed, the other samples show dominant AMR. Regarding the sample deposited for 75 ms with Nickel Sulfate, a typical curve of clusters was obtained. Therefore, it is shown that the GMR is really sensitive to the FM layers thickness of the solution containing Nickel Sulfate.

The results of the transport measurements of the multilayers are presented in Table 3.3. As was expected, when $t_{Ni}$ increases, ΔMR follows the same trend and gets closer to the MR of the homogeneous samples. This is logical because the higher the electrodeposition time of Ni is, the closer the behaviour gets to the homogeneous sample. Surprisingly, the ΔMR of the HCNW sample prepared with Nickel Sulfamate is lower than the value of multilayers deposited for 300 ms of Ni. As previously mentioned, this could be due to damages of the sample during the etching or a residual cathode.

| Sample | ΔMR [%] Nickel Sulfamate | ΔMR [%] Nickel Sulfate |
|---|---|---|
| HCNW | 0.46 | 1.31 |
| Ni(300ms)/Cu(30s) | 0.65 | 0.38 |
| Ni(150ms)/Cu(30s) | 0.25 | 0.17 |
| Ni(75ms)/Cu(30s) | 0.02 | 0.02 |

Table 3.3: Comparison of the ΔMR for the samples prepared with solutions NiCu(NiSfmt1 M Cu2.5 mM) and NiCu(Cu2.5 mM) on the template C 20%. The electrodeposition of Ni was varied between 75 ms and 300 ms whereas the one of Cu was fixed to 30 s.

To conclude, it appears that no parameter proves to be the best for both solutions and the most efficient solution can not be determined when adjusting the electrodeposition time of the FM layers. Indeed, the solution containing Nickel Sulfate only indicates dominant GMR for a deposition time of 150 ms of Ni. It is also shown that the an isotropic magnetic behaviour does not always go along with the highest GMR. A possible reason for the isotropic behaviour of NiCu(150ms)/Cu(30s) on Figure 3.8c coupled with dominant AMR is the formation of Cu clusters. Finally, it has been demonstrated that the formation of well-defined multilayers is really complicated for both solutions.

After calibrating the electrodeposition time of Ni layers, the depositing time of Cu will now be looked at. For solution NiCu(NiSfmt1 M Cu2.5 mM), $t_{Cu}$ was raised by 10 s as EDX revealed that very few Cu was found in homogeneous wires. The characteristics of this sample are presented in Table 3.4. Regarding the magnetic properties, no significant difference occurs when adjusting the Cu layer. The only difference takes place in OOP, in which direction the coercivity and normalised remanence slightly increase. The same behaviour was obtained when $t_{Cu}$ was increased with the previous solution. Therefore, it reinforces the idea that Cu deposits really slowly as no noticeable difference appears after a deposition of 40 s. Regarding the magneto-transport properties, the ΔMR decreases for thicker NM layers as is expected. Thus, the optimal Cu deposition time is 30 s.

| Sample | ΔMR [%] | $\frac{M_{r,IP}}{M_s}$ [/] | $H_{c,IP}$ [kOe] | $\frac{M_{r,OOP}}{M_s}$ [/] | $H_{c,OOP}$ [kOe] |
|---|---|---|---|---|---|
| Ni(300ms)/Cu(30s) | 0.65 | 31.2 | 0.17 | 45.9 | 0.2 |
| Ni(300ms)/Cu(40s) | 0.52 | 28.3 | 0.17 | 54.9 | 0.27 |

Table 3.4: Normalised remanence $M_r/M_s[/]$, coercivity $H_c$ [kOe] and $\Delta MR[\%]$ of the CNWs samples prepared by means of solutions NiCu(NiSfmt1 M Cu2.5 mM) and NiCu(Cu2.5 mM) on the template C 20%. The magnetic field was applied in the IP and in the OOP directions.

For solution NiCu(Cu2.5 mM), $t_{Cu}$ was lowered by steps of 5 s as the EDX measurements revealed a larger amount of Cu in homogeneous Ni wires prepared with Nickel Sulfate rather than Nickel Sulfamate. When the time of Cu layers goes from 30 s to 25 s, the easy direction becomes again the OOP direction (Fig. 3.10a). It may indicate that at 30 s, the Cu layers are very long compared to the Ni layers, hence the dipolar coupling between multilayers is weak.This is why shape anisotropy dominates and the easy axis is the IP direction. This is depicted on Figure 3.11 by a peak of the coercivity at 25 s. Then, reducing the size of the non-magnetic layers increases the isotropy of the system. This behaviour is coherent when looking at the evolution of the normalised remanence and coercivity (Fig. 3.11). However, for the last reduction of the deposition time to 6 s, the system is isotropic as shown on Figure 3.10b but the normalised remanence and coercivity increase. This might be due to the fact that the Cu layers are too thin and that the behaviour gets closer to the one of a homogeneous sample.

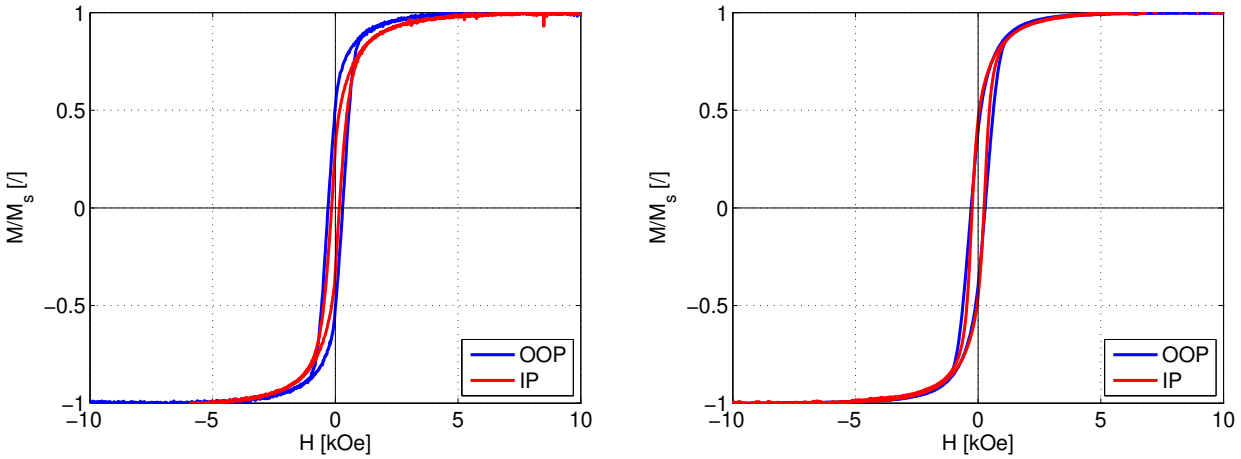


(a) Ni(150ms)/Cu(25s)

(b) Ni(150ms)/Cu(6s)

Figure 3.10: Hysteresis loops of multilayered CNWs prepared with solutions NiCu(Cu2.5 mM) on the template C 20%. The magnetic field was applied in the IP (red) and in the OOP directions (blue).

Although the system tends to be more isotropic when decreasing the deposition time of Cu, the magneto-transport measurements revealed dominant AMR for each sample. Unfortunately, it was impossible to measure the sample Ni(150ms)/Cu(6s) because of very thin and fragile magnetic layers. Regarding the evolution of the ΔMR on Figure 3.11, it first dramatically decreases when switching from the homogeneous sample to a multilayered CNW network. Then, the diminution goes from 0.17% to 0.7% before increasing to 0.1% and finally almost doubling. This behaviour is unexpected,

indeed, the expected behaviour of the AMR is a rise when the size of the non-magnetic layers are increased. However, the sample NiCu(150ms)/Cu(30s) almost reaches the same value as the sample deposited for the half the electrodeposition time. Another explanation could be that this sample was a very good sample in which the additional resistances are very low compared to the resistance of the network. For the others, the etching might have damaged the sample or some problems might have been encountered during the electrodeposition, such as no switch of potentials.

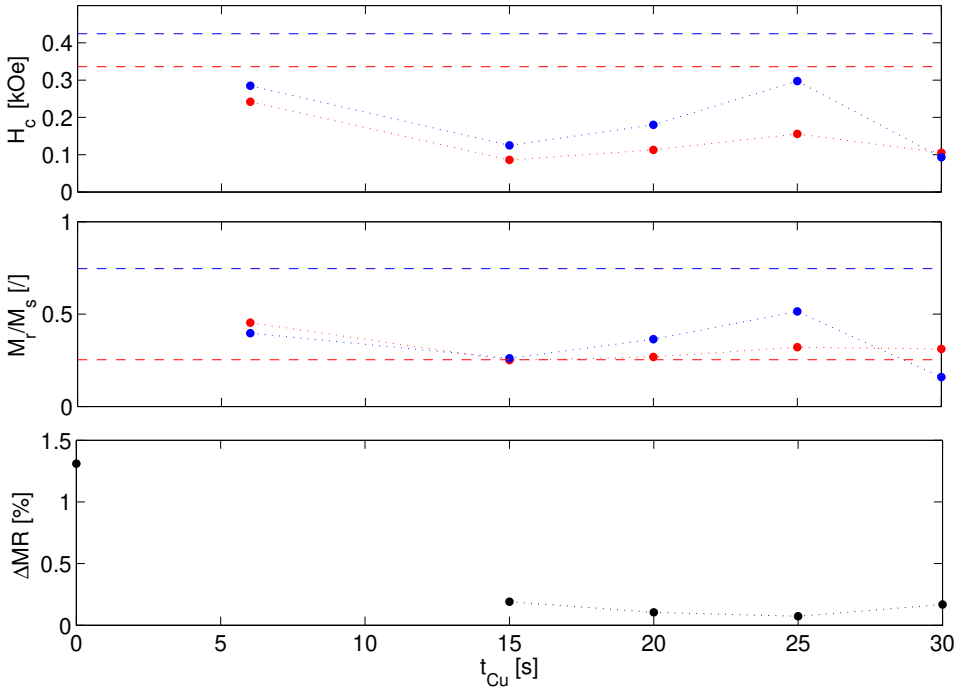


Figure 3.11: Evolution of the coercivity ($H_c$) [kOe], normalised remanence ($M_r/M_s$) [/] and $\Delta$MR [%] with the electrodeposition time of Cu ($t_{Cu}$). The multilayered CNWs were prepared with solution NiCu(Cu$2.5\,\mathrm{mM}$) on the template C 20% and $t_{NiCu}$ was fixed to $150\,\mathrm{ms}$. The horizontal dashed lines represent the values of the homogeneous sample. The samples were measure in the IP (red) and in the OOP directions (blue).

### 3.1.3 Study of crossed nanowires on a low porosity template (3%)

#### Optimisation of the solution NiCu(Cu$2.5\,\mathrm{mM}$)

As the sample NiCu(150ms)/Cu(30s) presents the best behaviour among all the previous samples, the same parameters were reiterated on a low porosity template to investigate the effect of the crossing zones. Three multilayered CNWs were prepared and different electrodeposition time were performed on each of them. The two first ones are multilayered samples deposited for $150\,\mathrm{ms}$ of Ni and $30\,\mathrm{s}$ of Cu. The last sample was deposited with longer electrodeposition times. The reason for that is the switch of template from C 20% to C 3% accompanied by an increase of the pore diameter from $40\,\mathrm{nm}$ to $80\,\mathrm{nm}$. Therefore, the times must be increased in order to balance the change of diameter and keep the same aspect ratio.

The magnetic results of the homogeneous sample on Figure 3.12a are similar to the equivalent sample prepared on a higher porosity template (Fig. 3.6c), where the hysteresis loop shows an anisotropic behaviour with the OOP direction as easy axis. Nevertheless, the OOP curve has become squarer with an increase of the normalised remanence and the coercivity. This is due to the fact that the dipolar interaction between wires is reduced when the porosity of the template decreases. Therefore, the magnetostatic anisotropy is higher for the template C 3% than C 20%. As for magneto-transport, the MR and $\Delta$MR have a value of 1.68% and 1.42% respectively. The resistance curve is shown on Figure 3.12b. So, no major changes are observed regarding the transport measurements, when changing the template. This is coherent because the configuration and the angles of the NWs is the

same on both template. The only difference is the lower number of contacts between the NWs and the cathode. However, this effect is negligible, and the resistance of the wires are mainly measured.

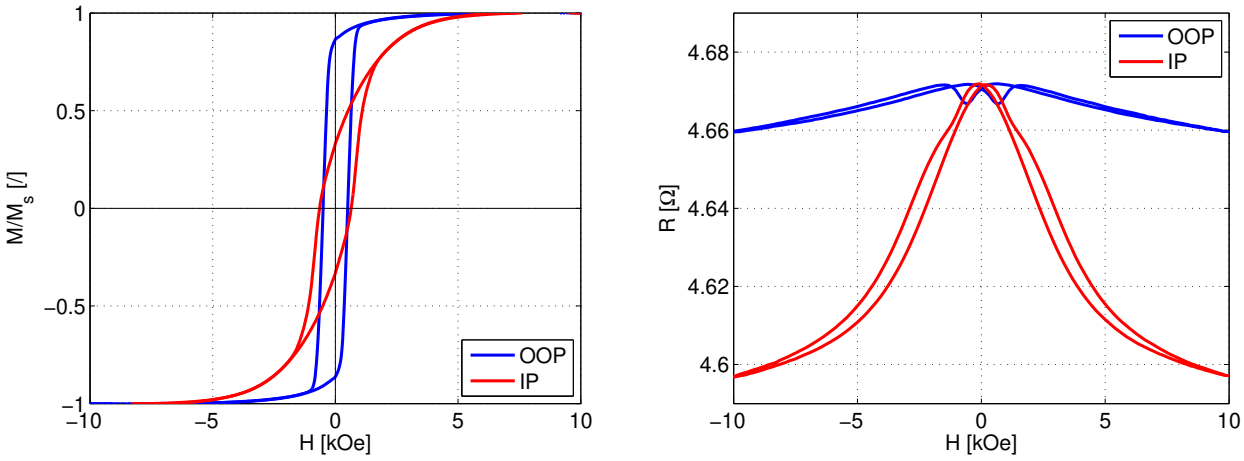


(a) (b)

Figure 3.12: Hysteresis loops and resistance curves of homogeneous CNWs prepared with solutions NiCu(Cu2.5 mM) on the template C 3%. The sample has a MR=1.68% and ΔMR=1.42%. The magnetic field was applied in the IP (red) and in the OOP directions (blue).

The hysteresis loops and the corresponding resistance curves of the CNWs samples are shown on Figure 3.13. First, the two samples Ni(150ms)/Cu(30s) have the same magnetic properties. Their coercivities do not change for both directions and are very small, around 0.12 kOe and the normalised remanence is around 0.22 in IP and more than doubles in OOP (Fig. 3.13a). So, the isotropic behaviour is no more found and the easy direction also switches compared to the sample with the same parameters on a lower porosity template (Fig. 3.9a). This behaviour might be explained by the fact that the interaction between NWs is lower and therefore, the magnetostatic anisotropy increases. Regarding the sample deposited for longer electrodeposition times, the only difference is a higher remanence in OOP, marked by a squarer hysteresis loop as is observed on Figure 3.13c. This could indicate that thicker layers are formed due to a deposition of 40 s. Therefore, the interaction between layers decreases because of the NM layers and the shape anisotropy is favoured because of thicker FM layers.

The same Ni(150ms)/Cu(30s) sample was cut in different parts that were etched and the results are presented in Table 3.5. They first indicate no reproducibility of the measurements and very low percentages compared to the reference sample, at least ten times lower. Moreover, the big difference of ΔMR with the sample A could be caused by the fact that each etched piece had a different resistance, 1 MΩ and 3 kΩ. This might indicate that the resistance of wires were not exclusively measured but also other resistances such as the resistance of contact or damages. For sample B, the resistance was smaller and of the same order of magnitude, between 38 Ω and 52 Ω, for each piece. For larger deposition times, the ΔMR is very low and its diminution is attributed to a larger amount of Cu. Surprisingly, Figures 3.13b and 3.13d do not show the GMR effect whereas a very low ΔMR should indicate a weak AMR effect and so dominant GMR in the multilayered systems. Moreover, it is illustrated that the GMR disappeared, when changing the template (Fig. 3.13b). This is unexpected because a reduction of the crossing zones should favour the measurement of the resistance of the wires. These results may be caused by imprecision during the electrodeposition or damages during the etching, which weakens

| Sample | Ni(150ms)/Cu(30s) A | Ni(150ms)/Cu(30s) B | Ni(200ms)/Cu(40s) |
|---|---|---|---|
| ΔMR [%] | 0.05<br>0.02 | 0.003<br>0.12<br>0.12 | 0.07 |

Table 3.5: ΔMR [%] of multilayered samples prepared with solution NiCu(Cu2.5 mM) on the template C 3%.

the sample.

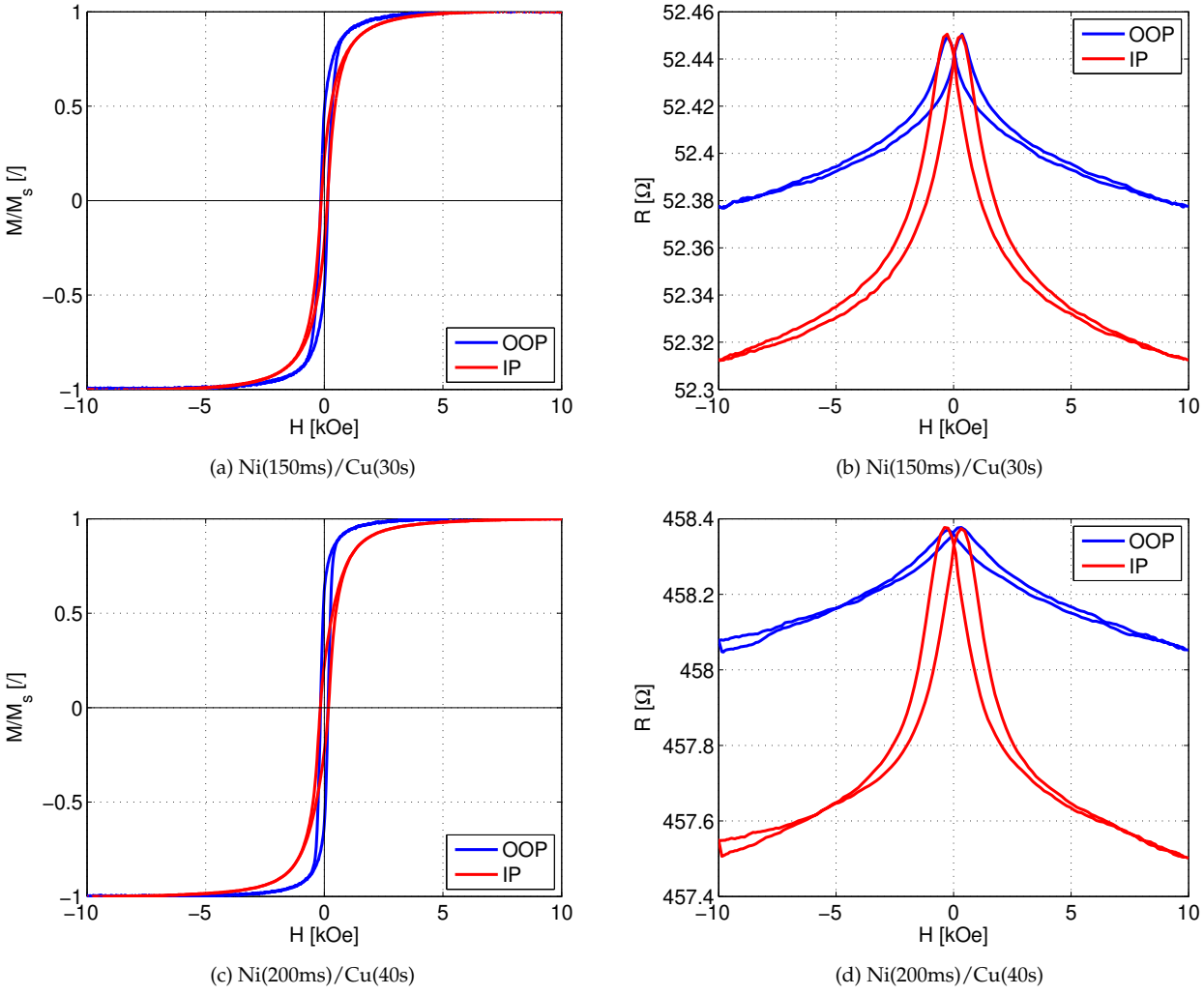


(a) Ni(150ms)/Cu(30s)

(b) Ni(150ms)/Cu(30s)

(c) Ni(200ms)/Cu(40s)

(d) Ni(200ms)/Cu(40s)

Figure 3.13: a, c) Hysteresis loops and b, d) resistance curves of the multilayered CNWs prepared with solutions NiCu(Cu2.5 mM) on the template C 3%. The ΔMR is equal to b) 0.12% and 0.07%. The magnetic field was applied in the IP (red) and in the OOP directions (blue).

Because no sample showing dominant GMR is found despite no peak reversal on the resistance curves, it means that the layers may not be well defined. Moreover, the larger pore diameter of this template has increases the space to do phase separation. Because a very low trace of Cu was detected in the previous electrolytes containing $2.5\,\mathrm{mM}$ of Cu, a new approach was to increase the amount of Cu and in that way, obtain an alloy with less than 10% of Cu should be obtained. The two new solutions, one with $7.5\,\mathrm{mM}$ of Cu and the other with $15\,\mathrm{mM}$ of Cu were prepared and studied in parallel.

**Optimisation of the solution NiCu(Cu$7.5\,\mathrm{mM}$)**

For a higher Cu content in the solution, the electrodeposition times were calibrated to reach a same thickness of $10\,\mathrm{nm}$ for each bilayer. As a result, $t_{Ni} = 150\,\mathrm{ms}$ and different electrodeposition times of Cu were tested : $t_{Cu} = 1, 3, 6, 9,$ and $16\,\mathrm{s}$. Moreover, the very large resistance obtained for the samples prepared with solution NiCu(Cu$2.5\,\mathrm{mM}$) motivated the will of trying a different technique to contact the NWs. That is the reason why, each specimen was cut in two pieces, one part to be etched and the other to be contacted by the top.

The hysteresis loop corresponding to the homogeneous sample has once again, an anisotropic behaviour and the OOP direction stays the easy axis. Regarding the values of the coercivity and the normalised remanence, they are similar to the corresponding sample with three times less Cu in the solution (Fig. 3.12a). Therefore, there is no change in the magnetic properties when more Cu is added to the electrolyte. Concerning the resistance curve, its evolution is similar to the homogeneous sample deposited with three time less Cu on Figure 3.12b and the MR and $\Delta$MR are equal to 1.86% and 1.58%, respectively. Thus, they increased when the Cu content was increased.

The hysteresis curve of two of the multilayered samples are presented on Figure 3.14. When multilayers were formed, the hysteresis loops becomes more isotropic than the homogeneous sample. This is normal because dipolar interaction between each layer is added and the shape anisotropy is lower. Secondly, a decrease of the electrodeposition of Cu does not considerably change the magnetisation curves of the sample. Indeed, all the hysteresis loops are similar to the one depicted on Figure 3.14c and some of them are slightly more isotropic. However, the sample with Cu layers deposited for $6\,\mathrm{s}$ is really particular. This latter is presented on Figure 3.14a. The first measurement indicates an isotropic behaviour, which is not consistent with the other samples. Furthermore, this sample has the highest GMR ratio of the whole series. That is why a second sample, with the same parameters has been prepared. Surprisingly, the magnetic behaviour has changed and is similar to the other samples (Figure 3.14c).

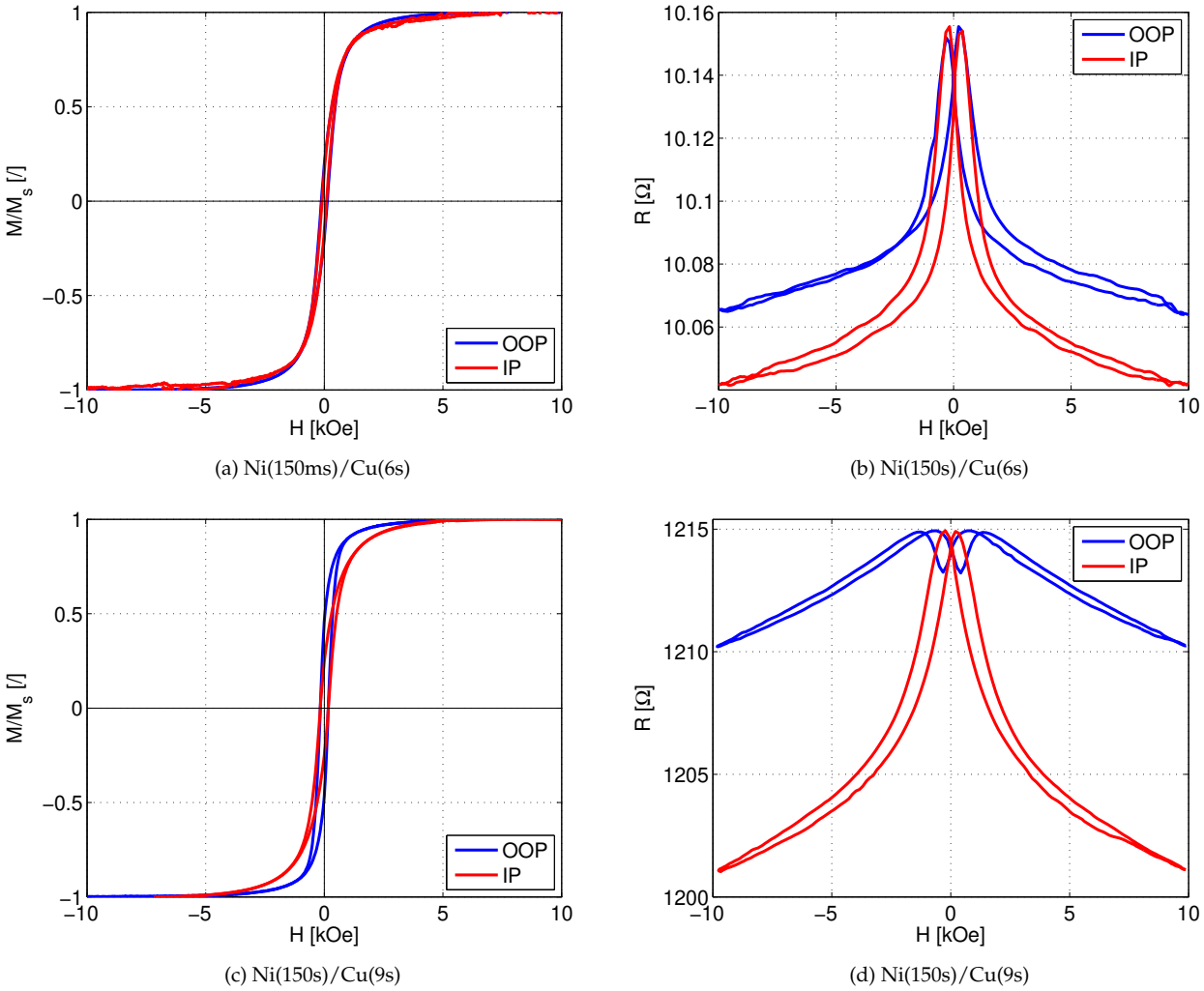


(a) Ni(150ms)/Cu(6s)

(b) Ni(150s)/Cu(6s)

(c) Ni(150s)/Cu(9s)

(d) Ni(150s)/Cu(9s)

Figure 3.14: a, c) Hysteresis loops and b, d) resistance curves of multilayered CNWs prepared with solutions NiCu(Cu7.5 mM) on the template C 3% and the corresponding resistance curves. The GMR is equal to b) 1.46%. The $\Delta$MR is equal to b) 0.45% and d) 0.75%. The magnetic field was applied in the IP (red) and in the OOP directions (blue).

If the evolution of the remanence and the coercivity are now looked at on Figure 3.15, a minimum is clearly indicated for the first sample Ni(150ms)/Cu(6s), whereas all the values are similar if the second one is considered. While the values of the coercivity are equal for both directions, the normalised remanence is higher in the OOP direction. It seems that changing the electrodeposition time of the NM layers has no effect on the magnetic properties.

Regarding the magneto-transport properties, a peak of GMR is obtained for the isotropic sample and the corresponding resistance curve is depicted on Figure 3.14b. A sharp peak is presented, which is the signature of GMR, as well as a small ΔMR. The values were obtained after etching and are 1.46% of GMR and 0.45% for the ΔMR, which clearly indicate the dominance of GMR. For the other samples, dominant AMR is obtained and the resistance curves looks like Figure 3.14d. Surprisingly, the evolution of ΔMR shows a peak for etched samples and gently increases for top contacts (Figure 3.15). These results are unusual. Indeed, when the non-magnetic layers are thicker, the AMR is expected to decrease. This may indicate imperfect samples for which the guideline during the electrodeposition has not exactly been followed. Or the contacts with the top cathode may have been positioned on spots under which few and/or damaged NWs were connected. Indeed, the porosity of the template is very low and the distribution is not uniform. Unfortunately, the second Ni(150ms)/Cu(6s) sample measurement was not conclusive for both top contacting and etching seeing that the signal was very noisy. This may be due to damages during the etching or poor contacts with the top cathode.

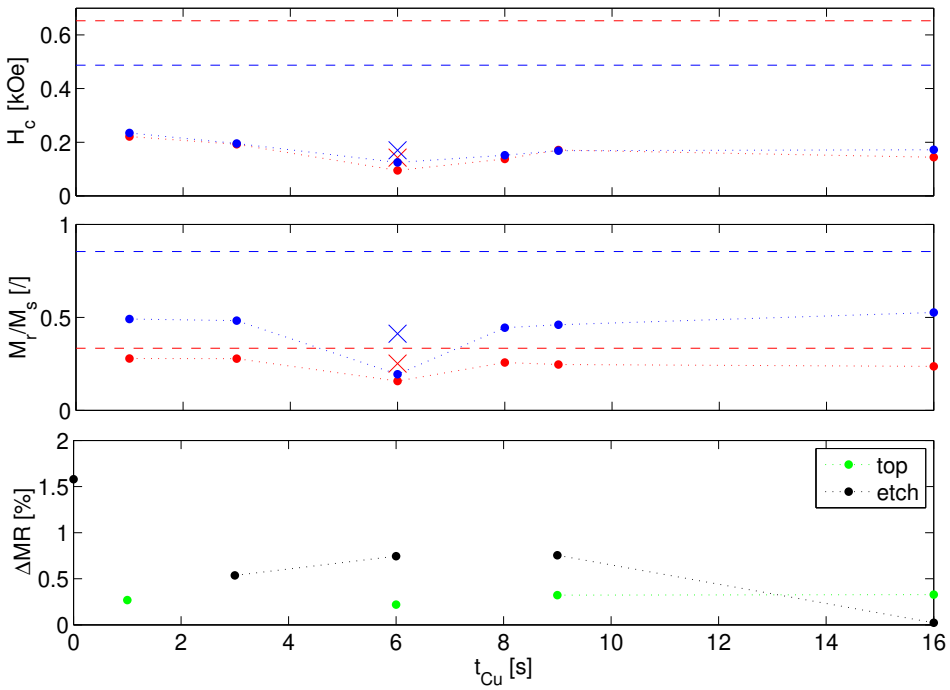


Figure 3.15: Evolution of the coercivity ($H_c$) [kOe], normalised remanence ($M_r/M_s$) [/] and ΔMR [%] with the electrodeposition time of Cu ($t_{Cu}$). The multilayered CNWs were prepared with solution NiCu(Cu7.5 mM) on the template C 3% and $t_{NiCu}$ was fixed to 150 ms. The horizontal dashed lines represent the values of the homogeneous sample. The crosses show the values obtained after deposition of a new sample with the same parameters. The samples were measured in the IP (red) and in the OOP directions (blue). To measure the magneto-transport properties, the samples were etched (etch) or put into contact by the top of the cathode (top).

To conclude, following the AGM measurements, it could seem that Cu deposits very slowly, even though its concentration had tripled, and that multilayers may not be formed. That is why very low GMR is obtained. This makes sense because the EDX results indicated about the same atomic percentage of Cu in HCNW array for 2.5mM and 7.5mM of Cu. In addition, the measurements also revealed larger quantity of Cu when the electrodeposition time of Cu increases. The attempt of calculating the size of the bilayers also indicated a thickening of the layers when $t_{Cu}$ increases

(Table 2.4). Nonetheless, it has to be reminded that EDX gives the overall percentage of the measured spot and the calculation is inexact and rather informative. Therefore, multilayers may not always be formed and some Cu clusters may be present too, which would justify why some GMR is still observed and why the magnetic properties are so less influenced.

### Optimisation of the solution NiCu(Cu$15\,\mathrm{mM}$)

For the solution NiCu(Cu$15\,\mathrm{mM}$), the electrodeposition time of Ni was calibrated to $136\,\mathrm{ms}$ and the one of Cu to $1\,\mathrm{s}$. Nevertheless, after deposition, it was noticed that approximately the double of bilayers were effectively grown compared to a previous estimation. This indicates that instead of growing 20-$\mathrm{nm}$ bilayers, the size is actually the half. This corresponds to what was calculated and is gathered in Table 2.4.

The hysteresis loops of the homogeneous sample are the same as the one prepared with $2.5\,\mathrm{mM}$ of Cu on Figure 3.12a. The normalised remanence and coercivity are similar too. Thus, no change in the magnetic properties are observed, when the amount of Cu is increased by a factor two. Regarding its MR, this latter is equal to 1.11%, and the ΔMR is equal to 0.94%, which indicates that the ratio decreases when more Cu is present. The opposite trend was observed when comparing compositions of $2.5\,\mathrm{mM}$ and $7.5\,\mathrm{mM}$ of Cu.

The magnetic properties of this series is gathered in Table 3.6. Regarding the coercivity of the multilayered samples, the values are similar for both directions and for both samples whereas for the normalised remanence, the values are similar for the IP direction and doubles when switching to the OOP direction. Besides, the shape of the curve is similar to the magnetisation curves obtained for two times less Cu in the solution on Figure 3.14c and the values are in the same range. Thus, the measurements indicate no big change in the magnetic properties, when changing the electrodeposition time of Cu. This is surprising because the EDX measurements revealed an increase in the Cu content.

| Sample | $\frac{M_{r,IP}}{M_s}[\%]$ | $H_{c,IP}$ [kOe] | $\frac{M_{r,OOP}}{M_s}[\%]$ | $H_{c,OOP}$ [kOe] |
|---|---|---|---|---|
| NiCu(136ms)/Cu(1s) | 27.3 | 0.215 | 53.7 | 0.225 |
| NiCu(136ms)/Cu(3s) | 25.6 | 0.172 | 53.2 | 0.175 |

Table 3.6: Normalised remanence $M_r/M_s[/]$ and coercivity $H_c$ [kOe] of the CNWs samples prepared by means of solution NiCu(Cu$15\,\mathrm{mM}$) on the template C 3%. The magnetic field was applied in IP and in OOP.

To measure the magneto-transport properties of this series, a cathode was deposited on four different spots at the top of the same sample. The results are shown in Table 3.7. As is shown, the ΔMR is very low compared to the homogeneous sample. Additionally, the signature of AMR is present in their resistance curve. This is behaviour is similar to what was obtained with the solution containing two times less Cu.

| Samples | NiCu(136ms)/Cu(1s) | NiCu(136ms)/Cu(3s) |
|---|---|---|
| ΔMR [%] | 0.24 | 0.01 |
| | 0.27 | 0.31 |
| | 0.09 | |
| | 0.33 | |

Table 3.7: ΔMR [%] of multilayered samples prepared with solution NiCu(Cu$15\,\mathrm{mM}$) on the template C 3%.

To conclude, it was observed that there is no striking difference between the two samples, although the amount of Cu had a concentration of $15\,\mathrm{mM}$ and therefore, should deposits faster. On top of that, the transport measurement might indicate that the layers were not correctly formed and phase separation occured.

### 3.1.4 Study of crossed nanowires on a very low porosity template (0.75%)

The best sample of all the attempts to obtain a high GMR ratio was the sample Ni(150ms)/Cu(30s) obtained with solution NiCu(Cu2.5 mM) on the template C 20%. For this reason, these electrodeposition parameters have been used on a template with a porosity of 0.75% and smaller pore diameter, which should restrain the phase separation. A homogeneous sample had first been prepared to determine whether or not the sample was too fragile to be measured. Indeed, the crossing zone are so few that the network easily breaks. Additionally, multilayers are more fragile than homogeneous samples.

The hysteresis loop and the resistance curve of the homogeneous sample are shown on Figure 3.16. As the previous reference samples, the system is anisotropic. Besides, the coercivity has increased, which is consistent because the interaction between wires is very low. As for the resistance curve, the shape is also the same, and the only difference is the MR that is equal to 0.94%. So, there is a big change when switching to a very low porosity template, whereas the results should be similar for each template. This is probably due to the fragility of the template C 0.75% inducing a lot of damages during the etching.

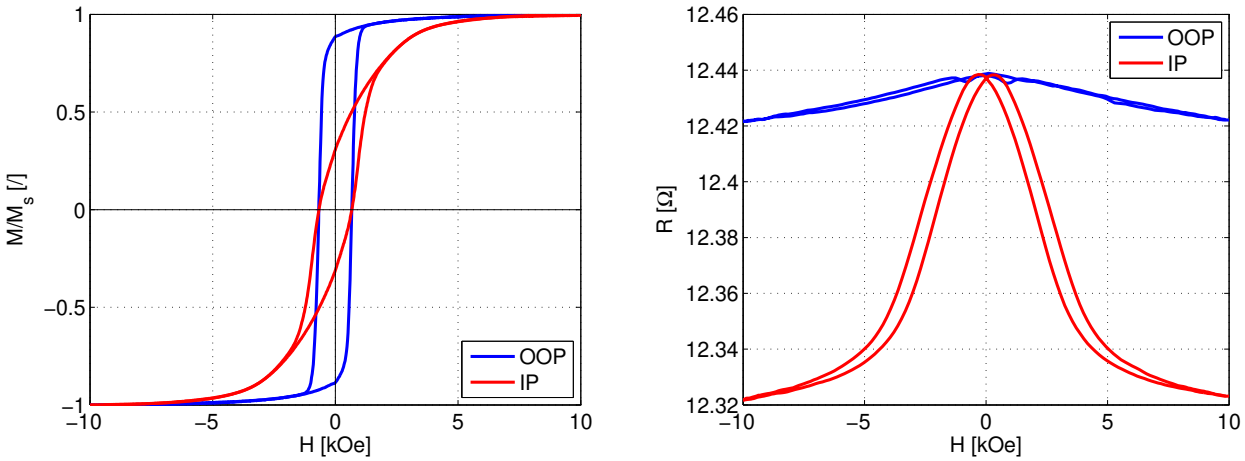


(a) (b)

Figure 3.16: Hysteresis loop and resistance curve of a homogeneous CNW sample prepared with solutions NiCu(Cu2.5 mM) on the template C 0.75%. The sample has a MR= 0.94% and ΔMR=0.8%. The magnetic field was applied in the IP (red) and in the OOP directions (blue).

Regarding the multilayered network, different parts of the deposited sample were cut and etched. Unfortunately, the resistance was too high to be measured, which indicated that the sample had been damaged. So, it can be concluded that it is extremely complicated to measure multilayered NWs on a very low density template because the sample is so fragile.

### 3.1.5 Conclusions for Ni/Cu multilayered NWs

As a conclusion, the many attempts to obtain a GMR ratio close to 5% with Ni/Cu CNWs arrays has highlighted the difficulty to form multilayers. Indeed, after changing the electrodeposition conditions, very few samples showed dominant GMR. On the template C 20%, the highest obtained values were 1.22% for Nickel Sulfamate and 1.16% for Nickel Sulfate whereas 1.45% was reached on the lower porosity template but for a higher amount of Cu. Although it was thought that Nickel Sulfamate favours core-shell systems compared to Nickel Sulfate, this latter did not stand out on the lower porosity template. The reason for these results is actually linked to the affinity of the two species. As can be seen on the phase diagram in Figure 3.17a, a very low percentage of Cu can be added in Ni at room temperature, otherwise phase separation occurs. Therefore, the composition must be precisely controlled to avoid any phase separation. Furthermore, a larger pore diameter was also found to facilitate phase separation. Indeed, as is shown on Figure 3.17b, the resistance curve shows the similar behaviour than the one of crossed nanotubes that are currently being studied at UCL.

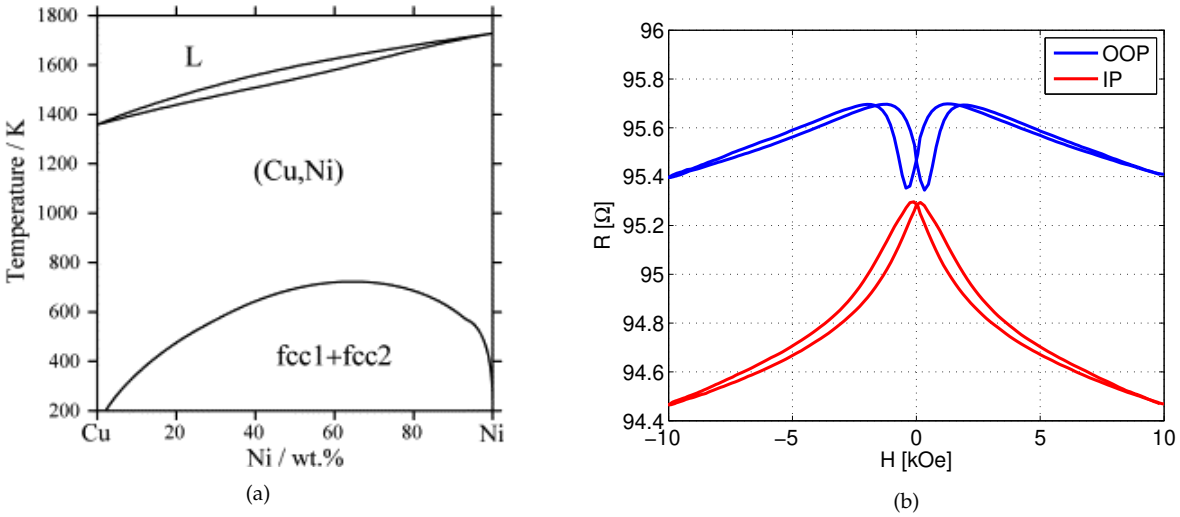


Figure 3.17: a) Phase diagram of Cu-Ni system [71]. b) Resistance curves of multilayered CNWs prepared with solutions NiCu(Cu7.5 mM) on the template C 3%. The Ni and Cu layers deposited for 150 ms and 30 s, respectively. The magnetic field was applied in the IP (red) and in the OOP directions (blue).

## 3.2 NiCo/Cu multilayered nanowires

In this section, the influence of adding Co in NiCu alloys on the magnetic and magneto-transport properties will be observed. For that purpose, the two solutions NiCoCu(Co25 mM) and NiCoCu(Co50 mM) were prepared in order to obtain two different percentages of Co lower than 30%. Two templates will be used to fabricate crossed nanowires: C 20% and C 3% and the properties will be examined on a reference sample as well as multilayers. Besides, the template with the high packing factor will be first used in order to calibrate the parameters of the electrodeposition that will give us the highest GMR ratio. Then, switching to the second template, a higher GMR ratio is expected.

### 3.2.1 Study of crossed nanowires on a high porosity template (20%)

#### Calibration of the solution NiCoCu(Co50 mM)

After the preparation of an homogeneous sample with an obtained composition of about **25%** of Co, the first multilayers were prepared. The electrodeposition times were chosen after calibrating each layer to 10 nm, which gave 600 ms for NiCo and 30 s for Cu. As a result, higher and lower electrodeposition times were used in order to see its influence on their magnetic and magneto-transport properties.

First, the properties of the homogeneous network is presented on Figure 3.18. As can be seen on Figure 3.18a, the system is anisotropic and the easy axis is oriented along the OOP direction. Moreover, the coercivity is similar in both direction whereas the normalised remanence goes from 0.4 in the IP to 0.64 in OOP directions. As for the resistance curve, a typical curve of AMR is indicated on Figure 3.18b and the value of the MR and $\Delta$MR are equal to 3.1% and 2.58%, respectively. This value is about two times superior to the values obtained for the sample fabricated with the solution NiCu(Cu2.5mM). Besides, a previous study obtained 2% of AMR with the same composition [45]. Therefore it can be concluded that these results are in agreement with each other.

Secondly, five multilayered CNWs arrays were prepared with the following parameters $t_{NiCo} = 300, 500, 600, 700, 1000$ s and $t_{Cu} = 30$ s. Three hysteresis loops are presented on Figure 3.19. As is observed on Figure 3.19a, the easy direction is the OOP direction and the system becomes more isotropic compared to the homogeneous sample (Fig. 3.18a). Then, decreasing the size of the magnetic layers induces less isotropic behaviour (Fig. 3.19c). The remanence in IP and OOP directions starts to move away from each other and the coercivity increases in the OOP direction. Increasing even more the NiCo deposition time to 1 s, the system is anisotropic (Fig. 3.19e). However, the loops are not as

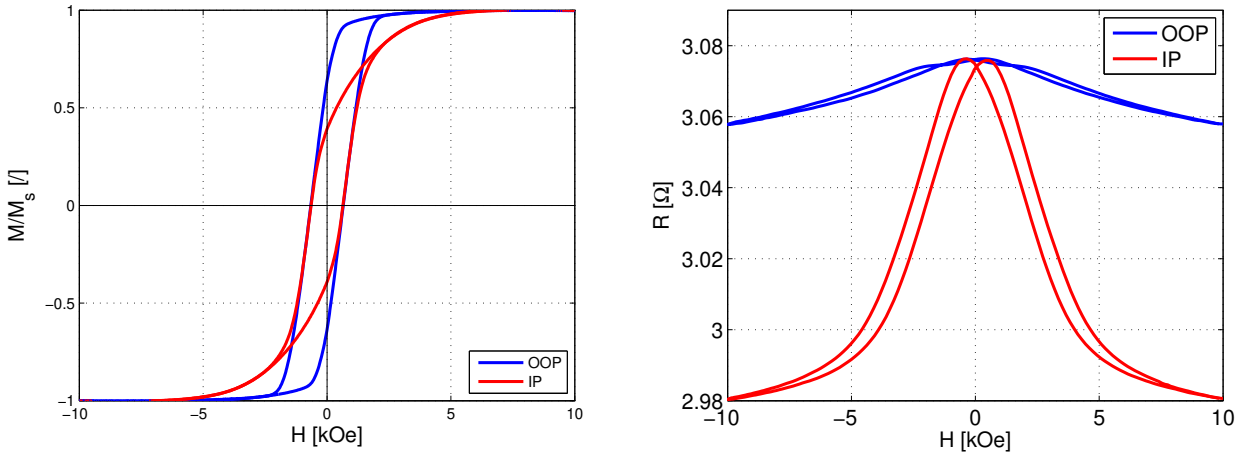


(a) HCNW

(b) HCNW

Figure 3.18: a) Hysteresis loop and b) resistance curve of a homogeneous CNW sample prepared with the solution NiCoCu(Co50 mM) on the template C 20%. The sample has a MR=3.1% and a ΔMR= 2.57%. The magnetic field was applied in the IP (red) and in the OOP (blue) directions.

squared as the reference sample. This evolution is correctly depicted on Figure 3.20. Furthermore, the values of normalised remanence and coercivity of the sample deposited for 300 ms are really close to the ones corresponding to the homogeneous sample (Figure 3.18a). This could be caused by the fact that thinner layers induces interaction between more magnetic layers because they are closer to each other. Therefore, these interactions overcome the shape anisotropy and so, the behaviour is similar to homogeneous samples. Nevertheless, the formation of layers is related to the fact that curves are not squared. This is clearly shown by the increase of the normalised remanence and coercivity for thinner FM layers in the OOP direction. In the other direction, the values are constant. This may be due to undetermined IP direction as was explained in Section 2.3.2.

In the case of magneto-transport properties, it can be observed on Figure 3.20 that the increase of the electrodeposition time of NiCo generates an enhancement of the GMR ratio from 2% up to a maximum of 6.82% for the sample NiCoCu(600ms)/Cu(30s). Then the percentage gradually decreases to 4.75%. Besides, as expected the ΔMR increases and gets closer to the value of the reference sample for thicker NiCo layers. Moreover, it is lower than the values of the GMR, therefore, GMR is dominant. This is effectively observed on the resistance curves on Figure 3.19. Indeed, all of the three curves show no peak reversal in OOP direction. Furthermore, it is seen that the sharpness of the peak goes along with higher GMR ratio.

To conclude, this series showed that the optimum parameters are a deposition time of 600 ms for the NiCo layers. However, the highest GMR ratio is not paired with the most isotropic behaviour. It has been demonstrated that adding 25% of Co in NiCu almost generated an increase by a factor 6 of the GMR ratio.

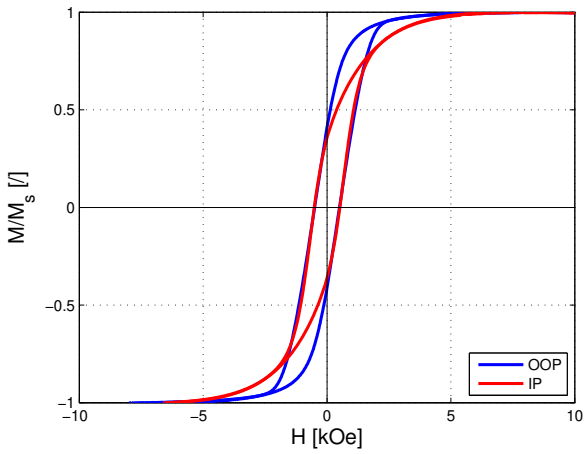


(a) NiCo(1s)/Cu(30s)

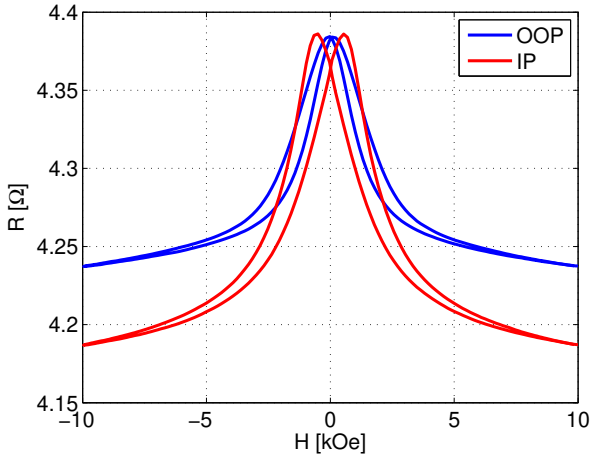


(b) NiCo(1s)/Cu(30s)

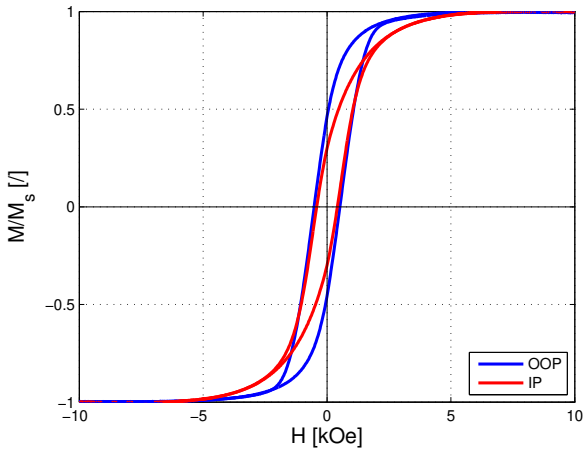


(c) NiCo(600ms)/Cu(30s)

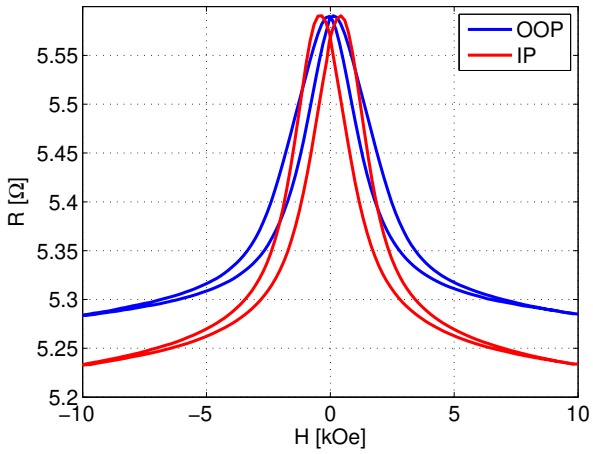


(d) NiCo(600ms)/Cu(30s)

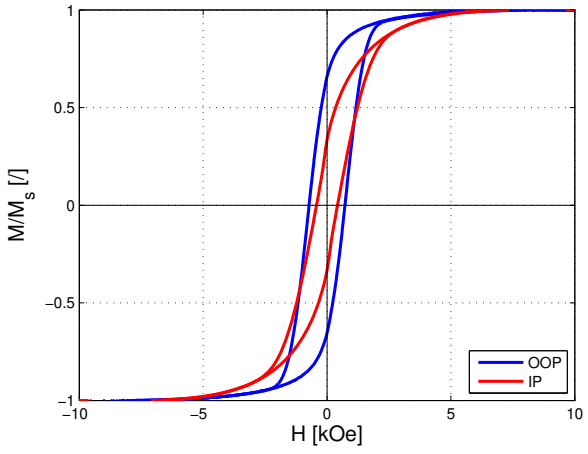


(e) NiCo(300ms)/Cu(30s)

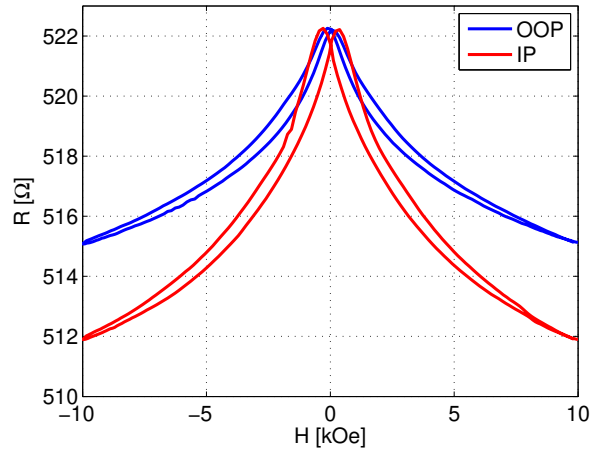


(f) NiCo(300ms)/Cu(30s)

Figure 3.19: a, c, e) Hysteresis loops and b, d, f) resistance curves of multilayered CNW samples prepared with the solution NiCoCu(Co50 mM) on the template C 20%. The samples b, d and f have respectively a GMR=4.75, 6.82%, 2% and a ΔMR=1.2%, 0.96% and 0.63%. The magnetic field was applied in IP direction (red) and in the OOP directions (blue).

Since it was found that the sample NiCoCu(600ms)/Cu(30s) gives a GMR percentage of 6.82%, it was chosen to change the electrodeposition time of Cu by a step of 10 s, between 10 s and 40 s. The magnetisation curves of two samples of the series are presented on Figure 3.21. First, the sample deposited with Cu layer pulse of 40 s has a similar curve to the one corresponding to a Cu deposition of 20 s on Figure 3.21a. Then, another reduction of the deposition time to 10 s generates an anisotropic magnetisation curves. This behaviour is really surprising. Indeed, normally, thicker Cu

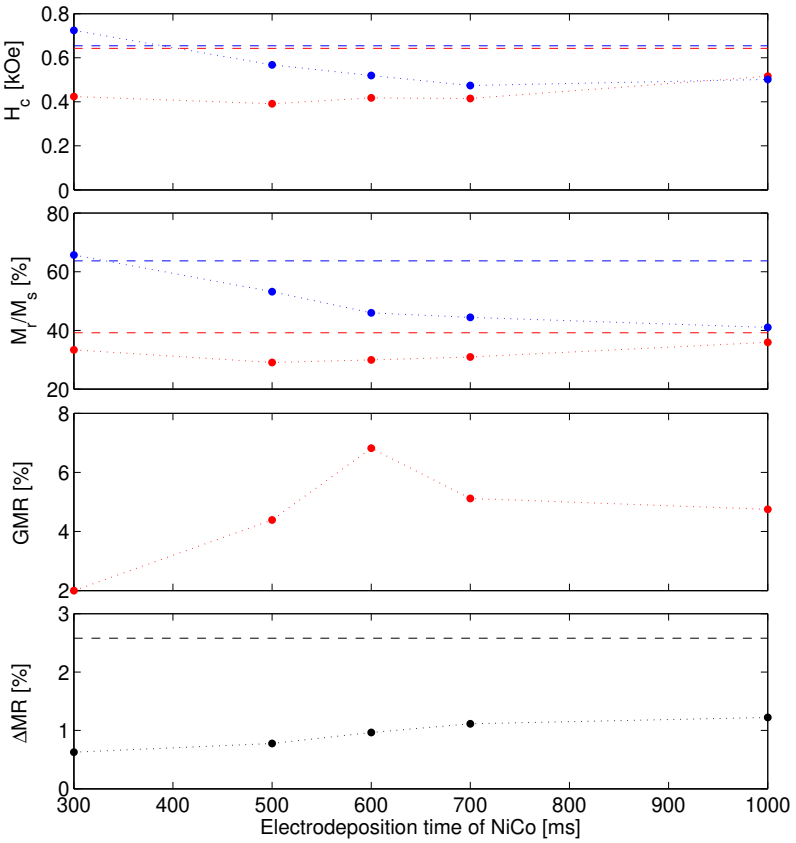


Figure 3.20: Evolution of the coercivity ($H_c$), normalised remanence ($M_r/M_s$), GMR [%] and the $\Delta$MR [%] with the electrodeposition time of NiCo ($t_{NiCo}$). The multilayered samples were prepared with solution NiCoCu(Co50 mM) on the template C 20% and the electrodeposition time of Cu was fixed to 30 s. The values of the reference sample are indicated by the horizontal dashed lines. The colours blue and red respectively corresponds the values in the OOP and the IP directions.

layers generates a reduction of the dipolar interaction between multilayers because they are further separated. Therefore, shape anisotropy dominates. Then, reducing the non-magnetic layers induces a rapprochement between the magnetic layers, the dipolar coupling between layers increases. Due to the fact that this contribution is negative, the hysteresis loop should switch from an anisotropic to an isotropic behaviour and increasing even more the dipolar coupling, the easy axis could switch.

If the evolution of the normalised remanence and coercivity are looked at (Fig. 3.22), it is shown that they both oscillate and that the difference between the IP and OOP direction reduces with decreasing $t_{Cu}$. This is logical because the system should get more isotropic when the thickness of the layers is reduced. Moreover, it is seen that for the sample NiCo(600ms)/Cu(10s), AMR dominates and the $\Delta$MR is close to the value of the reference sample (Fig. 3.21d), which means that the layers may have been too thin, so that they were not well defined. Then, increasing $t_{Cu}$ shows that the GMR going from 6.27% to 6.82% and finally going down to 5.1%. These values are the highest obtained for the moment and are clearly shown by a sharp peak of the resistance around $H_c$. As for the $\Delta$MR, an expected decrease of the difference can be seen for thicker Cu layers. In addition, the samples NiCo(600ms)/Cu(30s) and NiCo(600ms)/Cu(20s) have really close results, which might indicate that one of the them is not a good sample. It can be due to damages during the etching or a residual cathode layer that has not been etched.

To conclude, the best sample remains the one that was initially calibrated. Therefore, these parameters will be tried on the lower porosity template.

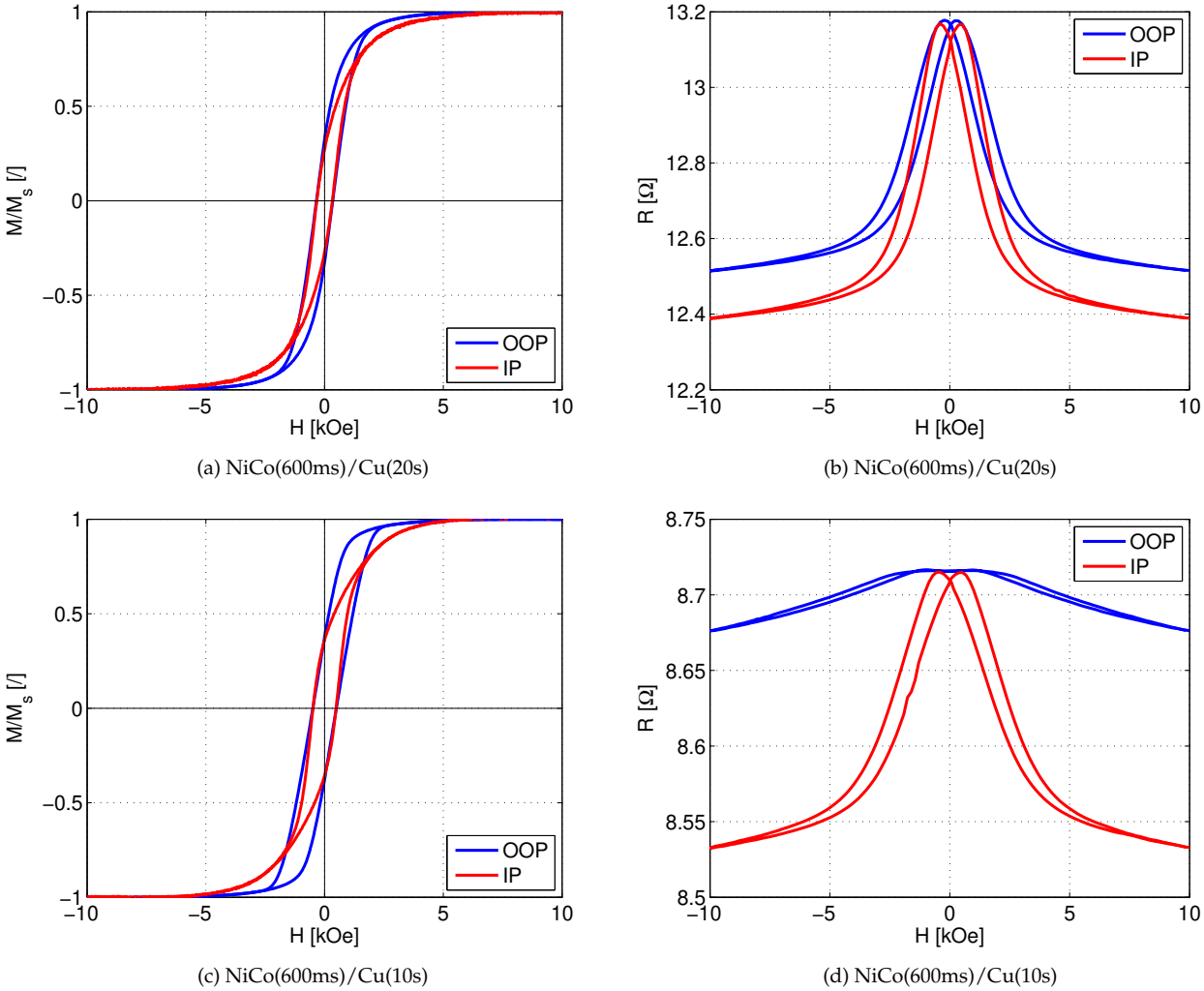


(a) NiCo(600ms)/Cu(20s)

(b) NiCo(600ms)/Cu(20s)

(c) NiCo(600ms)/Cu(10s)

(d) NiCo(600ms)/Cu(10s)

Figure 3.21: a, c) Hysteresis loops and b, d) resistance curves of a multilayered CNWs sample prepared with the solution NiCoCu(Co50 mM) on the template C 20%. The sample NiCo(600ms)/Cu(20s) has a of GMR= 6.27% and a ΔMR=0.94% while the sample NiCo(600ms)/Cu(10s) has a ΔMR=1.66%. The magnetic field was applied in the IP direction (red) and in the OOP direction (blue).

### Calibration of the solution NiCoCu(Co25 mM)

As far as solution NiCoCu(Co25 mM) is concerned, the EDX results indicated that the Co composition was around 15%. For this parameters, $t_{NiCo}$ has been calibrated to 700 ms and $t_{Cu}$ to 30 s.

To start, the hysteresis loop of the homogeneous sample shows really similar magnetisation curve compared to $Ni_{75}Co_{25}$ HCNWs (Fig. 3.18a). Nevertheless, the coercivity, which is also identical in both directions, is slightly lower and is equal to 0.54 kOe instead of 0.64 kOe for the other solution. This is logical because the magnetostatic energy is higher when more Co is present in the magnetic layers. Moreover, the resistance curve on 3.18b also has the same shape and the ΔMR is similar and has a value of 2.57%. The only difference is the MR ratio which increased to 3.03% for lower Co content, which is unexpected and disagrees with AMR evolution in the literature [45].

Among the three prepared multilayered CNW networks with a composition of 15% of Co, the most isotropic hysteresis loop is found for the sample deposited during 700 ms of NiCo and its magnetisation curve is shown on Figure 3.23a. If the evolution of the normalised remanence and coercivity are now examined on Figure 3.24, the same trend is observed for $Ni_{75}Co_{25}/Cu$ and $Ni_{85}Co_{15}/Cu$ multilayers, which is an increase of the difference between the values in the IP and the OOP directions when $t_{NiCo}$ goes down. Furthermore, a more anisotropic behaviour than the reference samples is obtained. Thicker layers result in a less isotropic system compared to Figure 3.23a, marked by the IP

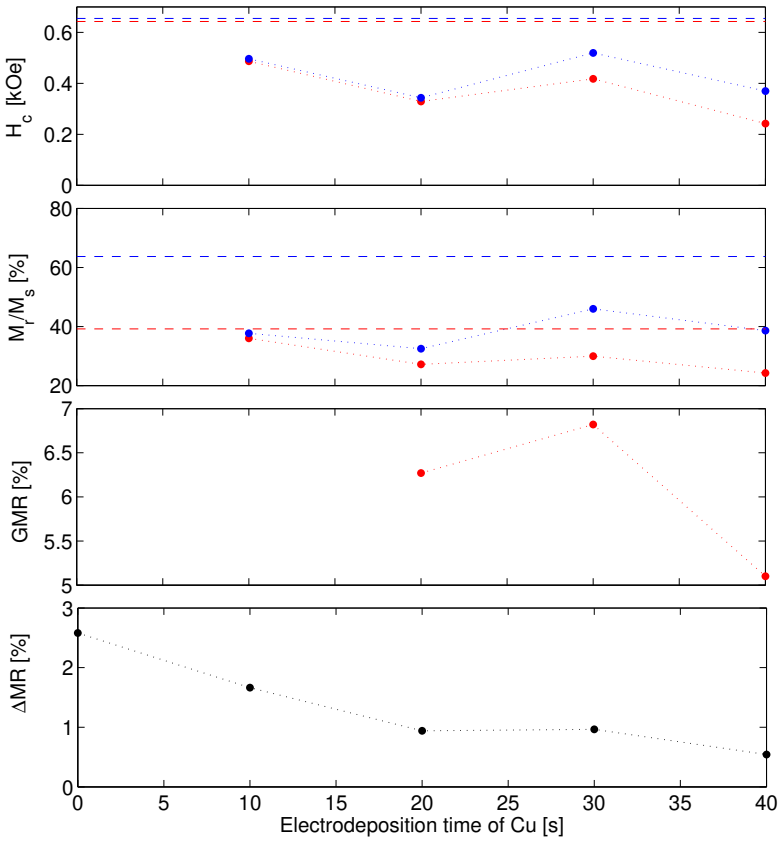


Figure 3.22: Evolution of the coercivity ($H_c$)[kOe], normalised remanence ($M_r/M_s$)[/], GMR [%] and the $\Delta$MR [%] with the electrodeposition time of Cu ($t_{Cu}$). The multilayered samples were prepared with solution NiCoCu(Co50 mM) on the template C 20% and the electrodeposition time of NiCo was fixed to 600 ms. The values of the reference sample are indicated by the horizontal dashed lines. The colours blue and red respectively corresponds the values in the OOP and the IP directions.

and OOP curve moving away from each other. This is coherent and is due to the fact that the magnetic layers are further apart and so, their interaction is lessened. That is why the behaviour gets closer to the reference sample. For thinner layers, the magnetisation curve is anisotropic and is similar to Figure 3.19e. The same reasoning as detailed for the solution containing more Co applies to explain this behaviour.

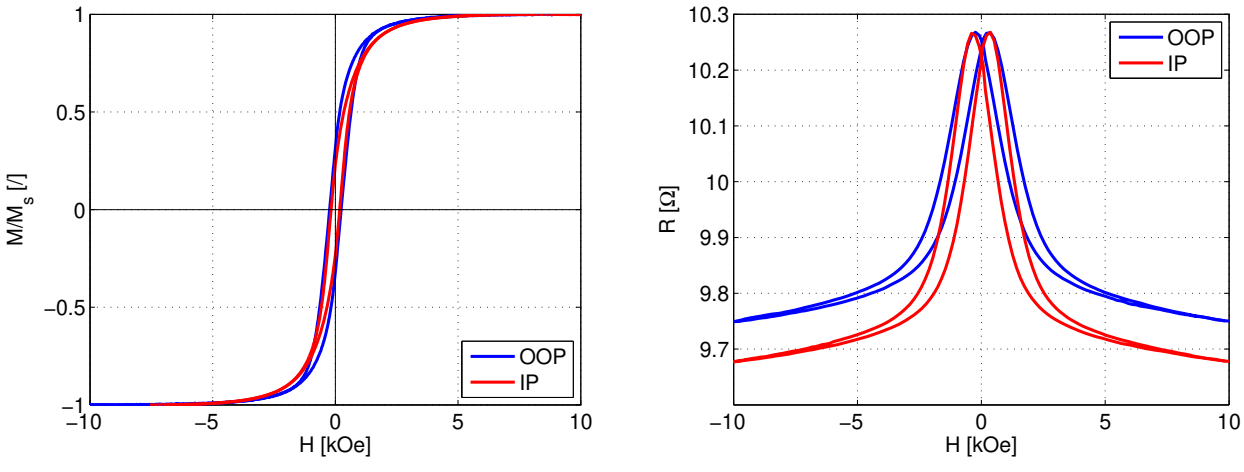


(a) (b)

Figure 3.23: a) Hysteresis loop and b) resistance curve of a multilayered sample NiCo(700ms)/Cu(30s) prepared with solution NiCoCu(Co25 mM) on the template C 20%. The sample has a GMR= 4.46% and a $\Delta$MR=0.76%. The magnetic field was applied in the IP (red) and OOP direction (blue) directions.

Figure 3.23b shows the resistance curve of the most isotropic system and giving the highest GMR ratio. This curve is similar to the equivalent sample $Ni_{75}Co_{25}/Cu$ on Figure 3.19c and dominant GMR is observed. As is demonstrated in Figure 3.24, the ratio is equal to 6.1% for this sample and plummets to 2.54% for thinner layers and to 4.46% for thicker ones. As for the ΔMR, it slightly increases with longer electrodeposition times but remains lower than 1%, as expected.

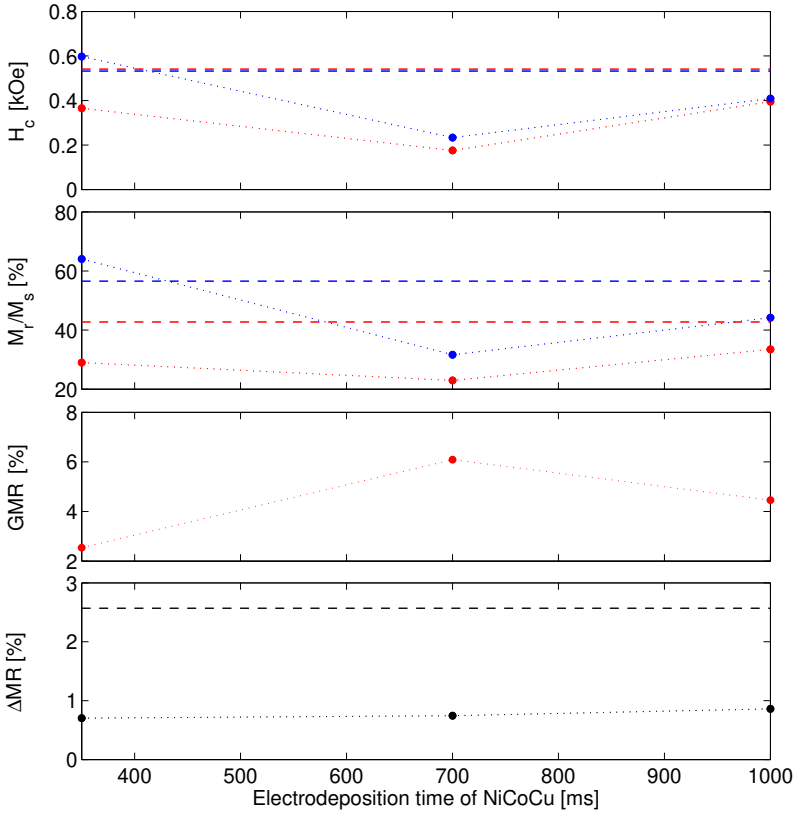


Figure 3.24: Evolution of the coercivity ($H_c$) [kOe], normalised remanence ($M_r/M_s$) [/], GMR [%] and ΔMR [%] with the electrodeposition time of NiCo ($t_{NiCo}$). The multilayered samples were prepared with solution NiCoCu(Co25 mM) on the template C 20% and the electrodeposition time of Cu was fixed to 30 s. The values of the reference sample are indicated by the horizontal dashed lines. The colours blue and red stands for the values in the OOP and IP directions respectively.

After calibrating the electrodeposition time of the magnetic layers, the evolution of the non-magnetic layer was studied, changing its electrodeposition time. Similarly to the same study performed on the solution containing 25% of Co, the magnetic measurements revealed the same conclusions as is shown on Figure 3.25. Choosing an electrodeposition time of 20 s gives the most isotropic behaviour whereas a deposition of 10 s for the Cu results in increasing anisotropy, similarly to the samples NiCu(600 ms)/Cu(20 s) and NiCu(600 ms)/Cu(10 s) prepared with higher amount of Co in the solution on Figures 3.21a and 3.21c, respectively. Nevertheless, varying the thickness of the layer does not significantly change the magnetic behaviour of the samples NiCo(700ms)/Cu(30s) and NiCo(700ms)/Cu(20s). However, the thinnest NM layers does not show a big gap between each direction, but rather the same coercivity and normalised remanence, which are very close to the values of the homogeneous sample. When looking at the magneto-transport properties of this series, it is seen that the parameters previously calibrated unsurprisingly remains the best. Whereas a deposition of 10 s of Cu create too thin magnetic layers, inducing a fall of the GMR ratio. However, a slight difference compared to the other solution is the ratio of the sample NiCo(700ms)/Cu20s), which is closer to the sample with thinner magnetic layers. Moreover, as expected the ΔMR decreases when more Cu is present.

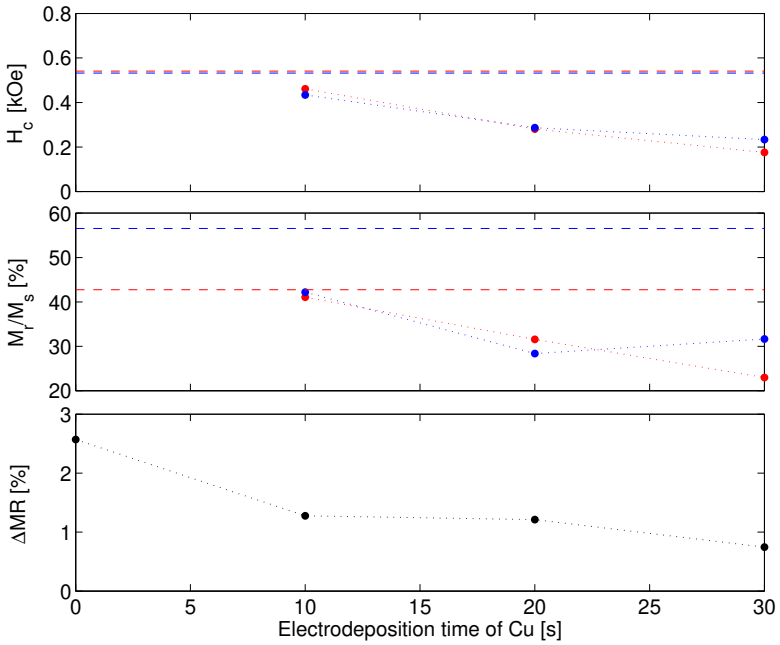


Figure 3.25: Evolution of the coercivity ($H_c$)[kOe], normalised remanence ($M_r/M_s$)[/], GMR [%] and the ΔMR [%] with the electrodeposition time of Cu ($t_{Cu}$). The multilayered samples were prepared with solution NiCoCu(Co25 mM) on the template C 20% and the electrodeposition time of NiCo was fixed to 700 ms. The values of the reference sample are indicated by the horizontal dashed lines. The colours blue and red respectively stands for the values in the OOP and in the IP directions.

A similarity can clearly be observed between the solutions with a composition of $Ni_{85}Co_{15}$ and $Ni_{75}Co_{25}$. Indeed, the calibrated samples gave the higher GMR ratio. In addition, very close values were obtained, between 6% and 7% for both systems, although lower amount of Co indicates slightly lower GMR. Moreover, changing the deposition times of NiCo by two or 0.5 and the ones of Cu by 10 s has globally the same effect on the specimen of both solutions, as well on their magnetic as their magneto-transport properties. That is why an additional sample of 40 s has not been prepared because it was observed, for the sample with a composition of $Ni_{75}Co_{25}$, that 30 s is the optimum deposition time for Cu layers.

### 3.2.2 Study of crossed nanowires on a low porosity template (3%)

**Calibration of the solution NiCoCu(Co50 mM)**

From the results on the first template, the sample NiCoCu(600ms)/Cu(30s) gives the highest GMR ratio. Therefore, the same parameters were tested on the template C 3% and other electrodeposition times were also analyzed.

The magnetic curves of the homogeneous sample is presented on Figure 3.26a and it is shown that the anisotropy rises when changing the template from high porosity to low porosity. The same behaviour took place for the solution NiCu(2.5mM) and the lowered interaction between wires due to the packing factor is again responsible. As for the MR, the percentage increases reaching 4.09% and 3.49% for ΔMR. As was mentioned for the NiCu study, changes in the MR should not be observed. However, the discrepancies may be related to the quality of the prepared sample.

As expected, the OOP direction remains the easy axis of the multilayers as is depicted on Figure 3.27a. Moreover, a diminution of the electrodeposition time of NiCo first creates an anisotropic behaviour for which $H_c$ decreases compared to the homogeneous sample. This indicates the formation of multilayers. Then, 200 ms less of NiCo per layer shows a big change as the system becomes more isotropic (Fig. 3.27c). When further decreasing $t_{NiCo}$ there is a small decrease of the isotropic behaviour (Fig. 3.27e). This is unexpected since a lowering of the size of the magnetic layers should induce a

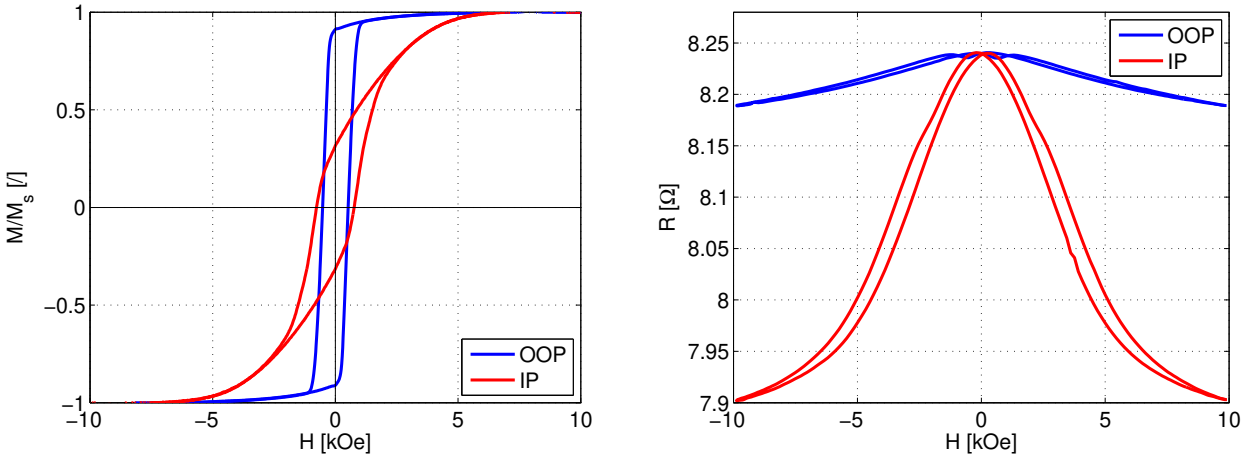


(a) (b)

Figure 3.26: Hysteresis loops and resistance curves of homogeneous CNWs prepared with solutions NiCoCu(Co50 mM) on the template C 3%. MR=4.09% and a ΔMR=3.49. The magnetic field was applied in the IP direction (red) and in the OOP direction (blue).

more isotropic behaviour or perhaps a switch of the axis. The evolution of the normalised remanence and coercivity are presented on Figure 3.28. As can be observed thicker layers generates at least a doubling of the values, getting closer to the one of the reference sample as expected. So it seems that decreasing the deposition time of the magnetic layers has no more impact below 1 s whereas the first decrease indicated that the magnetostatic anisotropy was affected. This unexpected behaviour may be due to random distribution of the pores. Because the porosity is already low, the measured species may not have the same number of pores and therefore, the interaction between wires is different.

Figure 3.28 also indicates that the more isotropic the system is, the higher the GMR ratio. Indeed, Figures 3.27d and 3.27d show a sharpest peak compared to Figure 3.27b, which show no more GMR. It is found that the sample NiCoCu(1s)/Cu(30s) gives the highest GMR ratio with 19.06% whereas the best sample on the template 20% presents a ratio of only 6.82%. Therefore, it is clearly seen that a lower porosity template increases the GMR. Moreover, the ΔMR increases when more magnetic material is added. This is logical because thicker layers means that the structure gets closer to the reference sample and can be observed on Figure 3.27. Finally, a gap can be seen between the ΔMR of the sample deposited for 1.2 s and the MR of the reference sample. This is due the fact that the magnetisation and resistance curves are really different from the homogeneous sample, although both curves are anisotropic.

After calibration of the magnetic layers, the Cu layers were optimised. Figure 3.29 shows the evolution of the magnetic and magneto-transport properties as a function of the electrodeposition time of the Cu layers. Exactly as the previous studies, a deposition of 30 s of Cu remains the most isotropic sample. On top of that, it is indicated that thinner Cu layers generate a more anisotropic system. This is due to the fact that a reduction of these layers generate a higher interaction between each magnetic layer and therefore, the magnetisation is favoured along the axis of the NWs.

The magneto-transport results show that the sample NiCoCu(1s)/Cu(30s) stays the best (Fig. 3.29), although increasing the electredeposition time of the NM layer gives a very close result of 18.65%. Furthermore, the less isotropic sample presents the disappearance of GMR and its value of ΔMR is very close to the homogeneous sample. This shows that the best conditions for having high GMR is a system being magnetically isotropic. Surprisingly, the ΔMR does not decrease when more Cu is present in the NWs. This is probably due to lower quality samples, which would explained why two similar GMR values are obtained, as well as increasing ΔMR for more non-magnetic material.

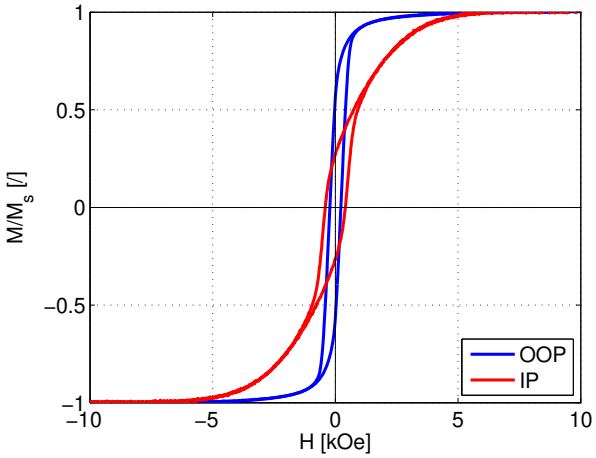


(a) NiCo(1.2s)/Cu(30s)

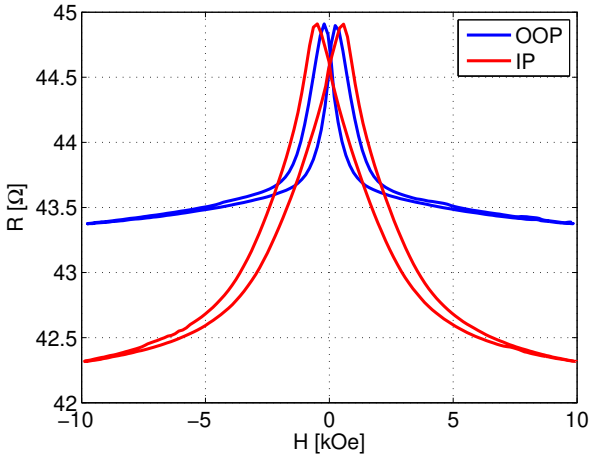


(b) NiCo(1.2s)/Cu(30s)

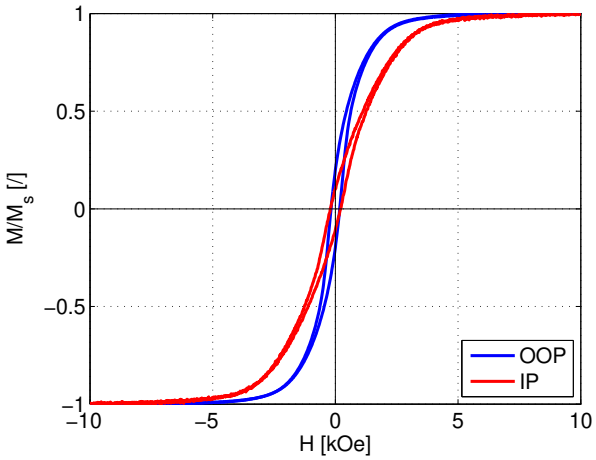


(c) NiCo(1s)/Cu(30s)

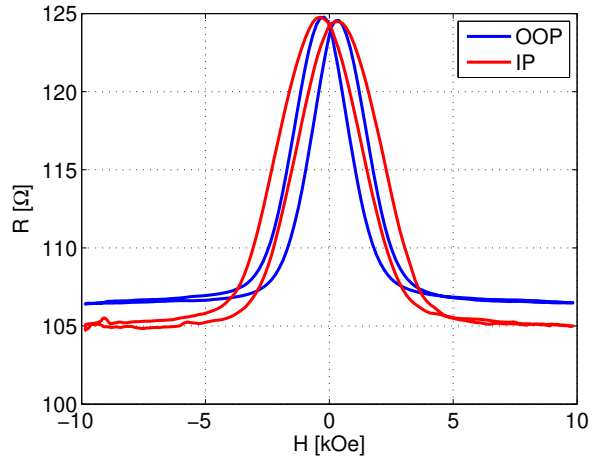


(d) NiCo(1s)/Cu(30s)

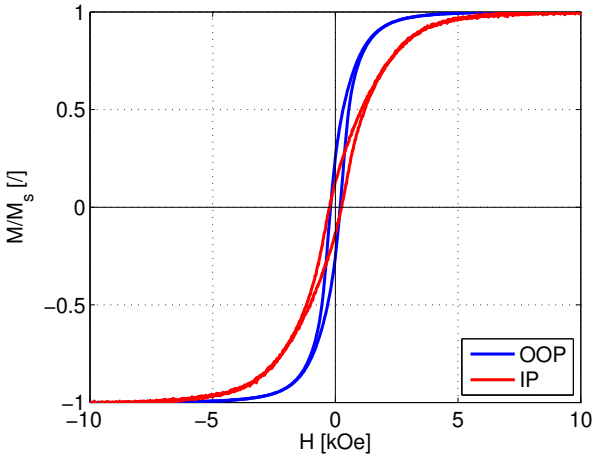


(e) NiCo(600ms)/Cu(30s)

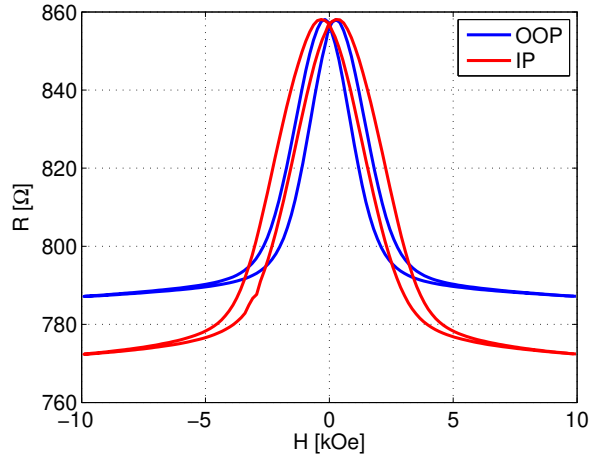


(f) NiCo(600ms)/Cu(30s)

Figure 3.27: a, c, e) Hysteresis loops and b, d, f) resistance curves of a multilayered CNW sample prepared with the solution NiCoCu(Co50 mM) on the template C 3%. The sample NiCo(1.2s)/Cu(30s) has a ΔMR=2.45% while NiCo(1s)/Cu(30s) has a of GMR= 19.06 % and a ΔMR=2.07%. The sample NiCo(600ms)/Cu(30s) has a GMR ratio of 11.08% and a ΔMR=1.9%. The magnetic field was applied in the IP (red) and in the OOP (blue) directions.

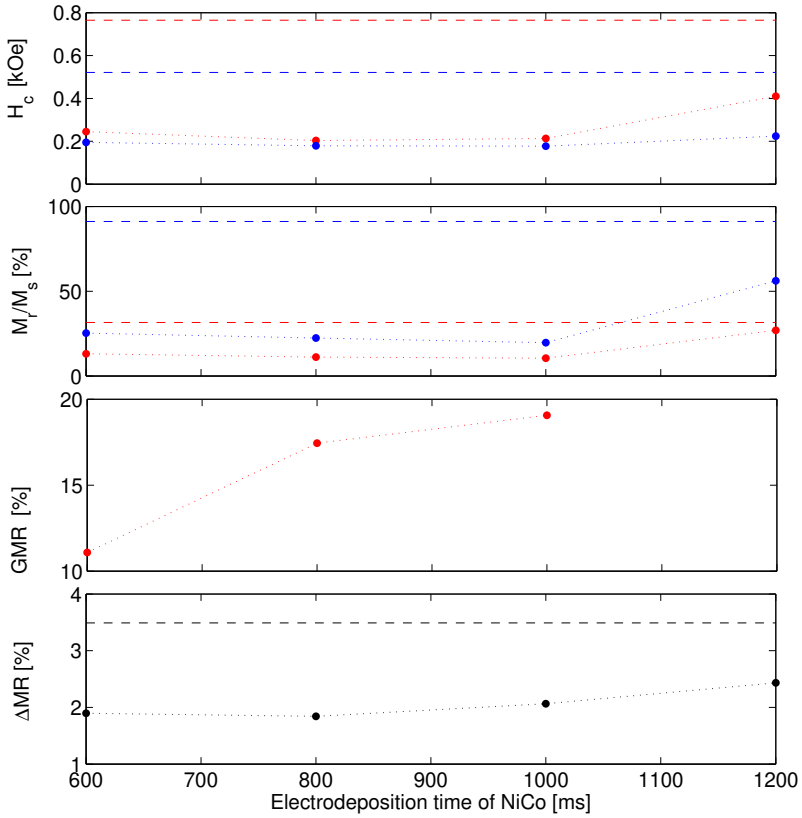


Figure 3.28: Evolution of the coercivity ($H_c$)[kOe], normalised remanence ($M_r/M_s$)[/], GMR [%] and the $\Delta$MR [%] with the electrodeposition time of NiCo ($t_{NiCo}$). The multilayered samples were prepared with solution NiCoCu(Co50 mM) on the template C 3% and the electrodeposition time of Cu was fixed to 30 s. The values of the reference sample are indicated by the horizontal dashed lines. The colours blue and red respectively stands for the values in the OOP and in the IP directions.

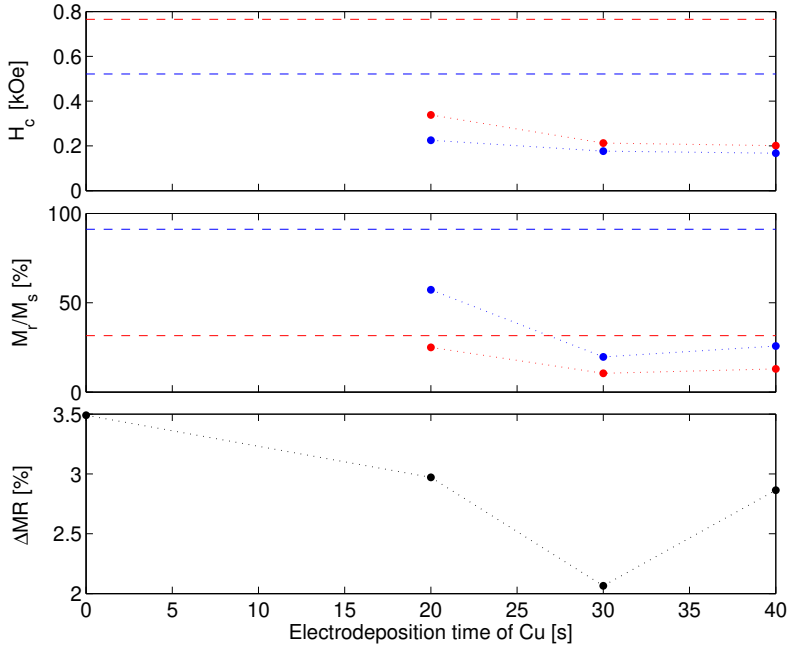


Figure 3.29: Evolution of the coercivity ($H_c$)[kOe], normalised remanence ($M_r/M_s$)[/] and the $\Delta$MR [%] with the electrodeposition time of Cu ($t_{Cu}$). The multilayered samples were prepared with solution NiCoCu(Co50 mM) on the template C 3% and the electrodeposition time of NiCo was fixed to 1 s. The values of the reference sample are indicated by the horizontal dashed lines. The colours blue and red respectively stands for the values in OOP and in IP directions.

**Calibration of the solution NiCoCu(Co25 mM)**

Since the parameters of the best sample on the template C 20% was found, the parameters were once again calibrated on a lower density template. The tested electrodeposition times were the following $t_{NiCo} = 700, 900, 1000, 1200\,\mathrm{ms}$. For a lower amount of Co, the homogeneous sample is even more anisotropic and the values of the coercivity increases when comparing the OOP and IP direction. This is similar to the reference sample with more Co on Figure 3.26a and for the same reasons, this is due to the lower porosity of the template, impacting the magnetostatic anisotropy. Furthermore, the values of MR and ΔMR stays the same whatever the template and are equal to 3.05% and 2.57%, respectively. This is logical because the reference samples have the same configuration and the same angles.

Concerning the magnetic behaviour of this series, as expected similar results were obtained compared to the same study with the solution containing 25% of Co. When forming multilayers, the OOP direction remains the easy axis and the sample deposited for $1.2\,\mathrm{s}$ presents an anisotropic behaviour similar to Figure 3.27a. Then, reducing the deposition time by $200\,\mathrm{ms}$ makes the system more isotropic, as is observed on Figure 3.30a. For lower $t_{NiCo}$, the shape of the magnetisation curve does not vary but the coercivity slightly increases.

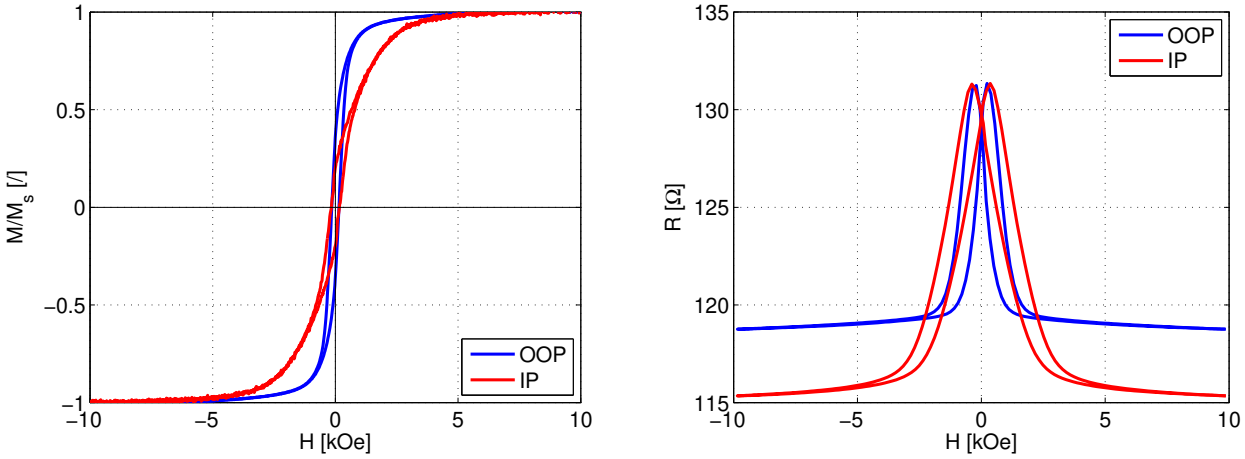


(a) (b)

Figure 3.30: Hysteresis loop and resistance curve of a multilayered CNWs sample prepared with solutions NiCoCu(Co25 mM) on the template C 3%. The sample was deposited for $900\,\mathrm{ms}$ of NiCo and for $30\,\mathrm{s}$ of Cu and has a GMR= 14.98% and a ΔMR=2.66%. The magnetic field was applied in the IP direction (red) and in the OOP direction (blue).

Regarding the evolution of the normalised remanence and coercivity on Figure 3.31, the coercivity of each sample is very similar for both directions. So, similarly to the series with a composition of 25% of NiCo, the three thinner magnetic layers presents similar magnetic properties as well as a small decrease of its isotropic behaviour for shorter deposition times whereas thicker layers get closer to the reference sample behaviour.

The GMR ratio indicates that the samples for which the electrodeposition times of NiCo are 700ms, 900ms and 1s give similar results: 13.87%, 14.98% and 14.58% respectively. Then, no more GMR is observed for a higher deposition time, which was also seen with the solution containing 25% of Co. So, the sample deposited for $900\,\mathrm{ms}$ (Figure 3.30a) is slightly more isotropic and has slightly higher GMR with respect to the other samples. For thicker NiCo layers, ΔMR dominates. Moreover, a very unusual behaviour of the ΔMR is depicted and presents a diminution of the ratio from $1\,\mathrm{s}$ to $1.2\,\mathrm{s}$. This can be justified similarly to the equivalent study with more Co by manufacturing defects, which could explain why three samples of the series have similar results.

Again, this study showed a lot of similarities compared to the solution containing more Co. First, most isotropic AGM curves are coupled with the highest GMR ratio. Besides, the reference samples

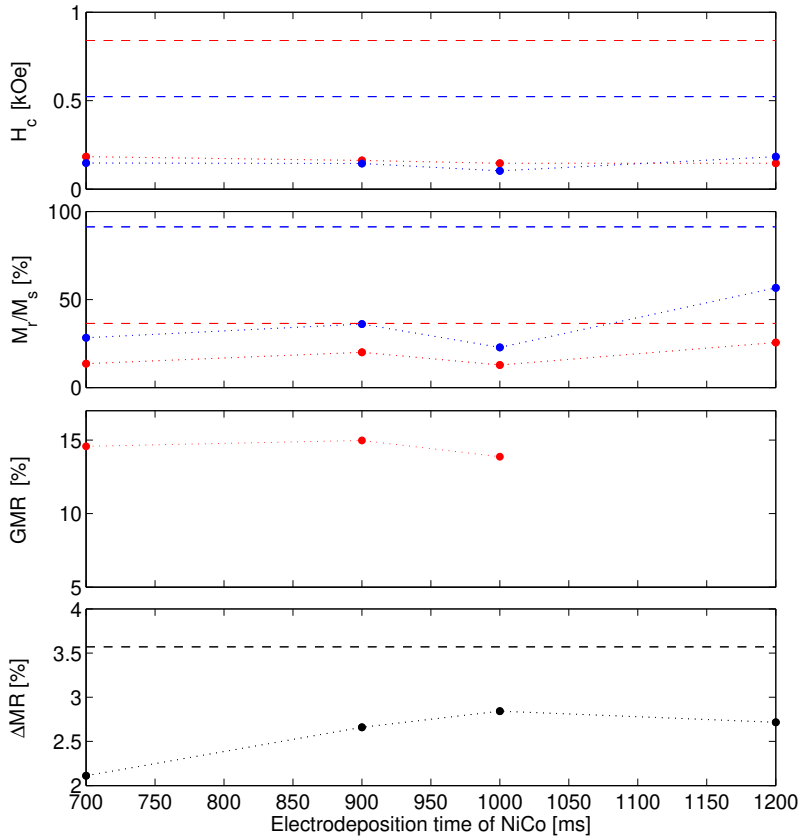


Figure 3.31: Evolution of the coercivity ($H_c$)[kOe], normalised remanence ($M_r/M_s$)[/], GMR [%] and the $\Delta$MR [%] with the electrodeposition time of NiCo ($t_{NiCo}$). The multilayered samples were prepared with solution NiCoCu(Co25 mM) on the template C 3% and the electrodeposition time of Cu was fixed to 30 s. The values of the reference sample are indicated by the horizontal dashed lines. The colours blue and red respectively stands for the values in OOP and in IP.

and equivalent electrodeposition times for multilayers give the same magnetisation curve. The evolution between the samples also goes in the same direction. Nevertheless, it appears that less Co gives a slightly lower GMR ratio, and especially on the lower porosity template.

Even though the evolution of the Cu layers thickness was tested on the 3% template for the alloy $Ni_{75}Co_{25}$, the analysis was not performed for this alloy $Ni_{85}Co_{15}$. The reason for that is the overall similar behaviour that was observed each time one parameter was varied for both alloys. That is why, it was assumed that a deposition of 30 s of Cu would once again give the best GMR ratio for the alloy $Ni_{75}Co_{25}$.

### Low temperature measurements

Once the best sample were found on the low porosity template, they were measured in IP at a low temperature of T=12K. A large increase is expected in NiCo/Cu multilayers.

First, because the sample NiCoCu(1s)/Cu(30s) presents the higher GMR ratio for $Ni_{75}Cu_{25}/Cu$ multilayers at room temperature, it was measured at 12K. The IP resistance curves at both temperatures are depicted on Figure 3.32. As can be seen, the resistance of the sample is reduced at low temperature, which is normal because of Matthiessen's law. Besides, the peaks are even sharpest when the temperature is lower, which is translated by about the double of the GMR percentage as indicated in Table 3.8. On top of that, the $\Delta$MR almost doubled at lower temperature similarly to the results presented in the literature showed for the AMR ratio [45]. So, an enhancement of the GMR is demonstrated as expected.

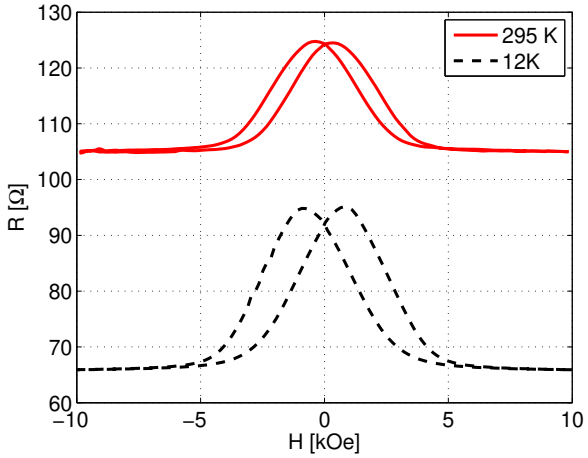


Figure 3.32: Comparison of the IP resistance curves at room and low temperatures of the sample NiCo(1s)/Cu(30s) prepared with the solution containing 25% of Co and deposited on the template C 3%. The GMR at 12K is 44.35% with a ΔMR of 4.53% while at room temperature, the GMR=19.06% and ΔMR=2.07%.

| Solution | Sample | T [K] | GMR [%] | ΔMR [%] |
|---|---|---|---|---|
| NiCoCu(Co50 mM) | NiCo(1s)/Cu(30s) | 295 | 19.06 | 2.07 |
| | | 12 | 44.35 | 4.53 |
| NiCoCu(Co25 mM) | NiCo(900ms)/Cu(30s) | 295 | 14.98 | 2.66 |
| | | 12 | 23.9 | 6.86 |
| NiCoCu(Co25 mM) | NiCo(1s)/Cu(30s) | 295 | 13.9 | 2.24 |
| | | 12 | 16.27 | 7.05 |

Table 3.8: Comparison of the GMR [%] and ΔMR [%] measured at 295K and at 12K.

Secondly, the two samples showing higher GMR for the solution containing 15% of Co were also measured at low temperature. At room temperature, their GMR ratio was 14.98% and 13.9% for the samples with NiCo layers deposited for 900 ms and 1 s. Then, lowering the temperature to 12K induces a GMR increase by a factor 1.5 for the best sample NiCo(1 s/Cu(30 s (Fig. 3.33b). In addition,

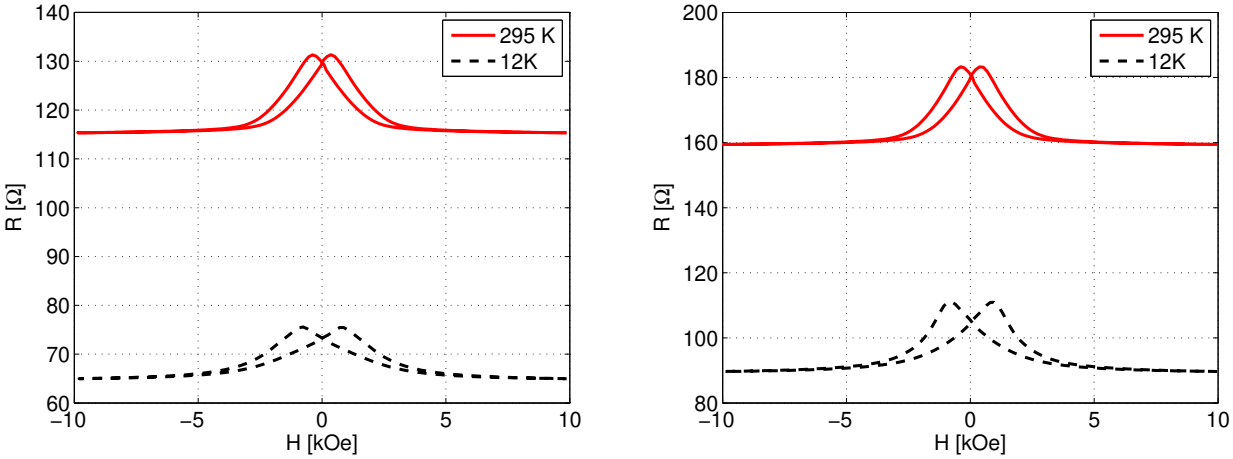


(a) NiCo(1s)/Cu(30s)

(b) NiCo(900ms)/Cu(30s)

Figure 3.33: Comparison of the IP resistance curves at room and low temperatures of the samples NiCo(1s)/Cu(30s) and NiCo(900ms)/Cu(30s) prepared with the solution containing 15% of Co and deposited on the template C 3%. The GMR at 12K is a) 16.27% with a ΔMR of 7.05% and b) 23.9% with a ΔMR of 6.86% while at room temperature, the GMR equals a) 13.9% and ΔMR=2.84% and b) 14.98% and ΔMR=2.66%

this increase is even less marked for the other sample as the percentage of GMR increases from 13.9% at room temperature to 16.28% at 12K (Fig. 3.33a). This is effectively shown on Figure 3.33, by a lower peak for the highest deposition time of NiCo. Therefore, for a solution containing 15% of Cu, the results indicated a less significant temperature effect, unlike for the sample with a higher amount of Co. Regarding the ΔMR, it also increased by a factor of around 3. This represents a higher temperature effect than what can be found in the literature for the AMR ratio [45].

## 3.3 Evolution of the GMR ratio with the composition in Co

To conclude this study, the best GMR results of the multilayers $Ni/Cu$, $Ni_{85}Co_{15}/Cu$ and $Ni_{75}Co_{25}/Cu$ will be presented. The evolution of the GMR ratio with the concentration of Co is presented on Figure 3.34. The results for larger amount of Co than 30% were studied in two other Master's Theses [12, 56].

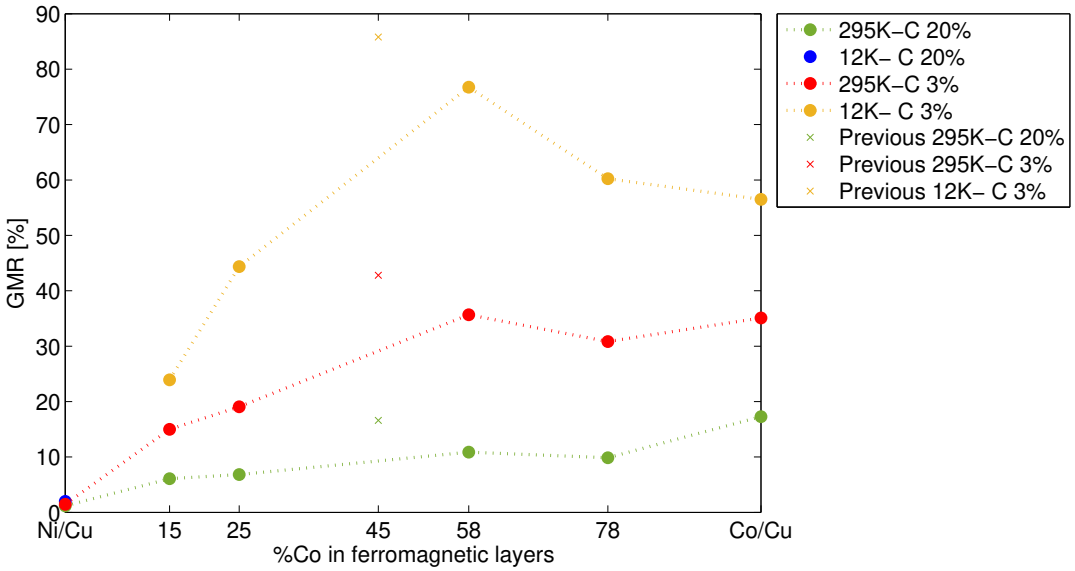


Figure 3.34: Evolution of the GMR [%] as a function of the percentage of Co in the ferromagnetic layers. The measurements on the template C 20% and 295K are presented in green and the ones on the template C3% in red for 295K and yellow for 12K.

As can be seen, on the template C 20% represented by a green curve, a very low percentage of GMR is obtained without adding any Co, which is equal to 1.16% at room temperature and 2% at 12K. Then, the addition of Co generates an increase of the GMR ratio by a factor of approximately five, reaching a value of 6.09%. Afterwards, the increase is lower and a ratio of 6.82% is obtained.

For the low porosity template in red, 1.46% was found for Ni/Cu multilayers. For NiCo/Cu arrays at room temperature, the GMR rises by 27% when the composition of Co goes from 15% to 25%. The measurements at low temperature in yellow indicate a more drastic increase. Indeed, the GMR goes from 24% up to 44%.

In addition, it can be observed that the difference of GMR at room temperature and at low temperature becomes larger when increasing the Co content. As a matter of fact, the GMR ratio more than doubles for 25% of Co whereas it increases by a factor 1.6 for 15% of Co.

To conclude, adding Co in a solution of NiCu dramatically increases the GMR and solves the encountered miscibility issues. Although the GMR ratio almost doubles at low temperature for Ni/Cu multilayers, the values remain low. Besides, the difference at room temperature and at low temperature is even more noticeable for a larger amount of Co. The negative effect of the crossing zones on the GMR ratio has also been highlighted.

# Conclusion and perspectives

This Master's Thesis has studied the magnetic and magneto-transport properties of multilayered CNW networks. In particular, Ni/Cu and $Ni_xCo_{1-x}/Cu$ CNWs with a lower Co composition than 30% were analysed. They were synthesised by electrodeposition in track-etched PC membranes of different porosities. After the dissolution of the membrane, SEM measurements confirmed the presence of a 3D interconnected network, which allowed to easily measure the magneto-transport properties. In addition, SEM/EDX analysis revealed the successful deposition of both the alloy and Cu in multilayered CNWs. In NiCu alloys, less than 10% of Cu was found whereas 15% and 25% of Co were present in the NiCoCu homogeneous samples. Finally, the effect of the deposition conditions on these properties have been observed.

The first study focused on Ni/Cu CNWs networks. The analysis of the magnetic properties indicated that thinner magnetic layers decreases the anisotropy of the system whereas this evolution is less pronounced when adjusting the Cu layers. Additionally, the magneto-transport measurements have highlighted the extreme difficulty to obtain a high GMR ratio. Indeed, the multiple attempts of changing the electrolyte composition, the electrodeposition parameters and the porosity of the templates showed a dominant AMR effect and only two samples presented dominant GMR. These two samples also presented the most magnetic isotropic behaviour. A maximum of 1.5% was reached on the low porosity template whereas 1.16% and 2% were obtained with high porosity at room temperature and 12K, respectively. Unfortunately, on the template with a porosity of 0.75%, the fragility of the multilayers and the very low interconnectivity prevented the magneto-transport measurements. When repeating the two best samples, no reproducibility was obtained. Although the etching process was thought to damage the samples and give rise to dominant AMR, it was revealed that the electrodeposition process was responsible for this behaviour. It has been found that both Nickel Sulfamate and Nickel Sulfate result in phase separation. The reason for this is that, at room temperature, only a very low percentage of Cu allows to form an alloy. Finally, evidence was shown that a larger pore diameter facilitates phase separation. Therefore, all these reasons explain the difficulty encountered to form multilayers.

Secondly, Co was added in NiCu alloy to enhance the GMR ratio, which showed less miscibility issues as well as well-defined multilayers. Regarding the magnetic properties, both solutions revealed similar results for equivalent samples. It has been shown that reducing the electrodeposition time of the NiCo layers leads to an anisotropic behaviour. In addition, varying the thickness of the Cu layers shows a more isotropic system for thinner layers. These behaviours were obtained on a high porosity template, whereas the opposite was observed for a low porosity. The transport measurements of the samples prepared with the two electrolytic solutions containing 15% and 25% of Co revealed a drastic increase of the GMR and especially for higher amounts of Co. On the higher porosity template, similar GMR ratios of 6% and 7% were obtained for $Ni_{85}Co_{15}/Cu$ and $Ni_{75}Co_{25}/Cu$ multilayers respectively. Then, measurements on a lower porosity template confirmed the negative influence of crossing zones on magneto-transport properties by showing more than a doubling of the GMR ratio. Finally, measurements at low temperature displayed a significant GMR enhancement, going from 15% to 24% and from 19% to 44% for lower and higher amounts of Co, respectively. These samples were accompanied by isotropic magnetic behaviour.

Therefore, the comparison between Ni/Cu and NiCo/Cu CNW arrays have shown that the GMR dramatically increases when more Co is added in the solution. Besides, this evolution is even more noticeable when using a lower porosity template and working at low temperature.

It is important to point out that very few samples were repeated for both Ni/Cu and NiCo/Cu multilayered CNWs. That is why multiple CNWs arrays with the same electrodeposition conditions should be deposited to increase the statistical significance of the measurements. Besides, new Co compositions could be prepared and optimised in order to have a more precise evolution of the GMR with the content in Co.

In a future work on Ni/Cu multilayers, it could be interesting to analyse the composition along a NW and measure the thickness of the layers using tunnelling electron microscopy (TEM). This would facilitate the analysis of targeting one parameter at a time, whether it is the template, electrodeposition times or potentials. Therefore, the issues related to phase separation in Ni/Cu CNWs arrays could be more easily controlled. Moreover, further study could focus on the influence of the temperature during the electrodeposition in order to increase the range of affinity between Ni and Cu. Another possibility could be to use a two-bath system so that the species are in separated electrolytes. Finally, the use of additives could also improve the formation of multilayers.

# Bibliography


[1] Locatelli, N. and Cros, V. (2016) *Introduction to Magnetic Random-Access Memory*, chap. 1. Basic Spintronic Transport Phenomena, pp. 1–28. Wiley-Blackwell.

[2] Kwon, O. S., Park, S. J., Yoon, H., and Jang, J. (2012) Highly sensitive and selective chemiresistive sensors based on multidimensional polypyrrole nanotubes. *Chemical Communications*, **48**, 10526–10528.

[3] Cox, B., Davis, D., and Crews, N. (2013) Creating magnetic field sensors from gmr nanowire networks. *Sensors and Actuators A: Physical*, **203**, 335–340.

[4] Wang, W., Tian, M., Abdulagatov, A., George, S. M., Lee, Y.-C., and Yang, R. (2012) Three-dimensional $Ni/TiO_2$ nanowire network for high areal capacity lithium ion microbattery applications. *Nano Letters*, **12**, 655–660.

[5] Crossland, E. J. W., et al. (2009) A bicontinuous double gyroid hybrid solar cell. *Nano Letters*, **9**, 2807–2812.

[6] Araujo, E., Encinas, A., Velázquez-Galván, Y., Martínez-Huerta, J. M., Hamoir, G., Ferain, E., and Piraux, L. (2015) Artificially modified magnetic anisotropy in interconnected nanowire networks. *Nanoscale Research Letters*, **7**, 1485–1490.

[7] Cojocaru, P., Leserri, A., Magagnin, L., Vázquez, M., and Carac, G. (2011) Electrodeposition of Ni/Cu multilayers nanowires using alumina template. *ECS Transactions*, **33**, 43–49.

[8] Fesharaki, M. J., Péter, L., Schucknecht, T., Rafaja, D., Dégi, J., Pogány, L., Neuróhr, K., Széles, E., Nabiyouni, G., and Bakonyi, I. (2012) Magnetoresistance and structural study of electrodeposited Ni-Cu/Cu multilayers. *Journal of The Electrochemical Society*, **159**, D162–D171.

[9] Tóth, J., Kiss, L., Tóth-Kádár, E., Dinia, A., Pierron-Bohnes, V., and Bakonyi, I. (1999) Giant magnetoresistance and magnetic properties of electrodeposited $Ni_{81}Cu_{19}/Cu$ multilayers. *Journal of magnetism and magnetic materials*, **198**, 243–245.

[10] Sato, H., Matsudai, T., Abdul-Razzaq, W., Fierz, C., and Schroeder, P. (1994) Transport properties of the Cu/Ni multilayer system. *Journal of Physics: Condensed Matter*, **6**, 6151.

[11] Serrano-Guisan, S., Gravier, L., Abid, M., and Ansermet, J.-P. (2006) Thermoelectrical study of ferromagnetic nanowire structures. *Journal of Applied Physics*, **99**, 08T108.

[12] Sopp, S. O. N. (2017) *Magnetotransport properties of interconnected magnetic nanowires and multilayers*. Master's thesis, Ecole polytechnique de Louvain, Université catholique de Louvain, prom. : Piraux, Luc.

[13] L.Piraux (2013) *MAPR1492 Physique des matériaux (seconde partie)*. SICI EPL.

[14] IEEE Magnetics, Magnetic units. Accessed May 7 2018, http://ieeemagnetics.org/index.php?option=com_content&view=article&id=118&Itemid=107.

[15] Stefanita, C.-G. (2012) *Magnetism: basics and applications*. Springer.

[16] Mohn, P. and Wohlfarth, E. P. (1987) The curie temperature of the ferromagnetic transition metals and their compounds. *Journal of Physics F: Metal Physics*, **17**, 2421.

[17] L. Piraux Mapr2471: Transport phenomena in solids and nanostructures, may 8 2018.

[18] Liu, Y., Sellmeyer, D. J., and Shindo, D. (2006) *Handbook of advanced magnetic materials*, vol. 1:Nanostructural effects. Springer.

[19] Tang, D. D. and Lee, Y.-J. (2010) *Magnetic memory: fundamentals and technology*. Cambridge University Press.

[20] Meyers, H. and Myers, H. (1997) *Introductory solid state physics*. CRC press.

[21] Bréchignac, C., Houdy, P., and Lahmani, M. (2008) *Nanomaterials and nanochemistry*. Springer.

[22] McGuire, T. and Potter, R. (1975) Anisotropic magnetoresistance in ferromagnetic 3d alloys. *IEEE Transactions on Magnetics*, **11**, 1018–1038.

[23] Zhang, X. and Butler, W. (2016) *Handbook of Spintronics*, chap. 1. Theory of Giant Magnetoresistance and Tunneling Magnetoresistance, pp. 3–69. Springer Netherlands.

[24] Valet, T. and Fert, A. (1993) Theory of the perpendicular magnetoresistance in magnetic multilayers. *Physical Review B*, **48**, 7099–7113.

[25] Pirota, K. R., Knobel, A., Hernandez-Velez, M., Nielsch, K., and Vázquez, M. (2017) *Oxford Handbook of Nanoscience and Technology*, vol. 2:Materials:Structures.

[26] Prida, V., García, J., Hernando, B., Bran, C., Vivas, L., and Vázquez, M. (2015) 2 - electrochemical synthesis of magnetic nanowires with controlled geometry and magnetic anisotropy. *Magnetic Nano- and Microwires*, pp. 41 – 104, Woodhead Publishing Series in Electronic and Optical Materials, Woodhead Publishing.

[27] El-Sherik, A. M. and Erb, U. (1995) Synthesis of bulk nanocrystalline nickel by pulsed electrodeposition. *Journal of Materials Science*, **30**, 5743–5749.

[28] Apel, P. (2001) Track etching technique in membrane technology. *Radiation Measurements*, **34**, 559–566.

[29] Zhu, X., Wang, C., Fu, Q., Jiao, Z., Wang, W., Qin, G., and Xue, J. (2015) Preparation of Ag/Cu janus nanowires: Electrodeposition in track-etched polymer templates. *Nuclear Instruments and Methods in Physics Research Section B: Beam Interactions with Materials and Atoms*, **356-357**, 57 – 61.

[30] Ferain, E. and Legras, R. (2003) Track-etch templates designed for micro- and nanofabrication. *Nuclear Instruments and Methods in Physics Research Section B: Beam Interactions with Materials and Atoms*, **208**, 115–122.

[31] it4ip, Track-etching technology. Accessed May 6 2018, https://www.it4ip.be/en/innovation/track-etching-technology/.

[32] Rauber, M., Alber, I., Müller, S., Neumann, R., Picht, O., Roth, C., Schökel, A., Toimil-Molares, M. E., and Ensinger, W. (2011) Highly-ordered supportless three-dimensional nanowire networks with tunable complexity and interwire connectivity for device integration. *Nano Letters*, **11**, 2304–2310.

[33] Piraux, L., George, J. M., Despres, J. F., Leroy, C., Ferain, E., Legras, R., Ounadjela, K., and Fert, A. (1994) Giant magnetoresistance in magnetic multilayered nanowires. *Applied Physics Letters*, **65**, 2484–2486.

[34] Prida, V., Vega, V., García, J., Iglesias, L., Hernando, B., and Minguez-Bacho, I. (2015) Magnetic nano- and microwires. chap. 1 - Electrochemical methods for template-assisted synthesis of nanostructured materials, pp. 3 – 39, Woodhead Publishing Series in Electronic and Optical Materials, Woodhead Publishing.

[35] Nasirpouri, F. (2017) *Electrodeposition of Nanostructured Materials*, chap. 5.Template Electrodeposition of Nanowires Arrays, pp. 187–259. Springer International Publishing.

[36] Pereira, A., Gallardo, C., Espejo, A. P., Briones, J., Vivas, L. G., Vázquez, M., Denardin, J. C., and Escrig, J. (2013) Tailoring the magnetic properties of ordered 50-nm-diameter coni nanowire arrays. *Journal of Nanoparticle Research*, **15**, 2041.

[37] Van Thiem, L., Tu, L. T., and Phan, M.-H. (2015) Magnetization reversal and magnetic anisotropy in ordered CoNiP nanowire arrays: Effects of wire diameter. *Sensors*, **15**, 5687–5696.

[38] De La Torre Medina, J., Darques, M., Blon, T., Piraux, L., and Encinas, A. (2008) Effects of layering on the magnetostatic interactions in microstructures of $Co_xCu_{1-x}/Cu$ nanowires. *Physical Review B*, **77**, 014417.

[39] Piraux, L., Dubois, S., Ferain, E., Legras, R., Ounadjela, K., George, J., Maurice, J., and Fert, A. (1997) Anisotropic transport and magnetic properties of arrays of sub-micron wires. *Journal of Magnetism and Magnetic Materials*, **165**, 352 – 355.

[40] Leven, B. and Dumpich, G. (2005) Resistance behavior and magnetization reversal analysis of individual Co nanowires. *Physical Review B*, **71**, 064411.

[41] Dumpich, G., Krome, T., and Hausmanns, B. (2002) Magnetoresistance of single Co nanowires. *Journal of Magnetism and Magnetic Materials*, **248**, 241 – 247.

[42] da Câmara Santa Clara Gomes, T. (2016) *Magnetic and magneto-transport properties of 3D networks of interconnected magnetic nanowires*. Master's thesis, Ecole polytechnique de Louvain, Université catholique de Louvain, prom. : Piraux, Luc.

[43] Evans, P., G.Yi, and Schwarzacher, W. (2000) Current perpendicular to plane giant magnetoresistance of multilayered nanowires electrodeposited in anodic aluminum oxide membranes. *Applied Physics Letters*, **76**, 481–483.

[44] Serrano-Guisan, S., Gravier, L., Abid, M., and Ansermet, J.-P. (2006) Thermoelectrical study of ferromagnetic nanowire structures. *Journal of Applied Physics*, **99**, 08T108.

[45] da Câmara Santa Clara Gomes, T., De La Torre Medina, J., Lemaitre, M., and Piraux, L. (2016) Magnetic and magnetoresistive properties of 3D interconnected NiCo nanowire networks. *Nanoscale Research Letters*, **11**, 466.

[46] da Câmara Santa Clara Gomes, T., De La Torre Medina, J., Velázquez-Galván, Y., M. Martinez-Huerta, J., Encinas, A., and Piraux, L. (2017) 3-D interconnected magnetic nanofiber networks with multifunctional properties. *IEEE Transactions on Magnetics*, **53**, 1–6.

[47] Samardak, A. S., Sukovatitsina, E. V., Ognev, A. V., Chebotkevich, L. A., Mahmoodi, R., Peighambari, S. M., Hosseini, M. G., and Nasirpouri, F. (2012) High-density nickel nanowire arrays for data storage applications. *Journal of Physics: Conference Series*, **345**, 012011.

[48] Ielmini, D., Cagli, C., Nardi, F., and Zhang, Y. (2013) Nanowire-based resistive switching memories: devices, operation and scaling. *Journal of Physics D: Applied Physics*, **46**, 074006.

[49] Wang, S., Xu, L.-P., wei Liang, H., Yu, S.-H., Wen, Y., Wang, S., and Zhang, X. (2015) Self-interconnecting Pt nanowire network electrode for electrochemical amperometric biosensor. *Nanoscale*, **7 26**, 11460–7.

[50] Rahong, S., et al. (2014) Ultrafast and wide range analysis of dna molecules using rigid network structure of solid nanowires. *Scientific reports*, **4**, 5252.

[51] Hamoir, G., Piraux, L., and Huynen, I. (2013) Control of microwave circulation using unbiased ferromagnetic nanowires arrays. *IEEE Transactions on Magnetics*, **49**, 4261–4264.

[52] Scherer, M. R. J. and Steiner, U. (2013) Efficient electrochromic devices made from 3D nanotubular gyroid networks. *Nano Letters*, **13**, 3005–3010.

[53] Toal, B., McMillen, M., Murphy, A., Hendren, W., Atkinson, R., and Pollard, R. (2014) Tuneable magneto-optical metamaterials based on photonic resonances in nickel nanorod arrays. *Materials Research Express*, **1**, 015801.

[54] Bakonyi, I., Tóth, J., Kiss, L., Tóth-Kádár, E., Péter, L., and Dinia, A. (2004) Origin of giant magnetoresistance contributions in electrodeposited Ni–Cu/Cu multilayers. *Journal of Magnetism and Magnetic Materials*, **269**, 156 – 167.

[55] da Câmara Santa Clara Gomes, T., Medina, J. D. L. T., Velázquez-Galván, Y. G., Martínez-Huerta, J. M., Encinas, A., and Piraux, L. (2016) Interplay between the magnetic and magneto-transport properties of 3D interconnected nanowire networks. *Journal of Applied Physics*, **120**, 043904.

[56] Lebrun, J. (2018) *Magnetic and magneto-transport properties of 3D interconnected NiCo/Cu and Co/Cu multilayered nanowire networks*. Master's thesis, Ecole polytechnique de Louvain, Université catholique de Louvain, prom. : Piraux, Luc.

[57] Kazeminezhad, I. and Schwarzacher, W. (2004) Giant magnetoresistance in electrodeposited Ni-Cu/Cu multilayers and anisotropic magnetoresistance in pulse-plated $Ni_xCu_{1-x}$ alloy films. *Journal of Solid State Electrochemistry*, **8**, 187–189.

[58] Kazeminezhad, I. and Schwarzacher, W. (2008) Electrodeposited Ni-Cu alloy nanowires with arbitrary composition. *Electrochemical and Solid-State Letters*, **11**, K24–K26.

[59] Palmero, E., Bran, C., del Real, R., Magén, C., and Vazquez, M. (2014) Magnetic behavior of NiCu nanowire arrays: Compositional, geometry and temperature dependence. *Journal of Applied Physics*, **116**, 033908–033908.

[60] Jeol Ltd, Jed-2300 analysis station plus. Accessed May 20 2018, https://www.jeol.co.jp/en/products/detail/JED-2300_2300F.html.

[61] Materials Evaluation and Engineering. INC, Scanning electron microscopy (SEM). Accessed April 24 2018, https://www.mee-inc.com/hamm/scanning-electron-microscopy-sem/.

[62] Central Microscopy Research Facility, Scanning electron microscopy. Accessed April 23 2018, https://cmrf.research.uiowa.edu/scanning-electron-microscopy.

[63] Australian Microscopy & Microanalysis Research Facility, Electron-matter interactions. Accessed April 24 2018, http://www.ammrf.org.au/myscope/sem/background/concepts/interactions.php#detail.

[64] Canadian Centre for Welding and Joining, Microscopy. Accessed April 22 2018, https://sites.ualberta.ca/c̃cwj/teaching/microscopy/#XWerner2012.

[65] Materials Evaluation and Engineering. INC, Energy dispersive X-Ray spectroscopy (EDX). Accessed April 24 2018, https://www.mee-inc.com/hamm/energy-dispersive-x-ray-spectroscopyeds/.

[66] Central Facility for Advanced Microscopy and Microanalysis, Introduction to energy dispersive x-ray spectrometry (EDX). Accessed April 24 2018, https://cfamm.ucr.edu/documents/eds-intro.pdf.

[67] Graham, C. (2000) High-sensitivity magnetization measurements. **16**, 97–101.

[68] Flanders, P. J. (1988) An alternating-gradient magnetometer (invited). *Journal of Applied Physics*, **63**, 3940–3945.

[69] Lake Shore Cryotronics, PMC MicroMag 2900 Series AGM. Accessed April 21 2018, https://www.lakeshore.com/products/Vibrating-Sample-Magnetometer/PMC-MicroMag-2900-Series-AGM/Pages/Overview.aspx.

[70] Institute for Micromanufacturing, Alternating grandient magnetometer. Accessed May 19 2018, http://www.ifm.latech.edu/resources/equipment/agm.php.

[71] Wang, C., Liu, X., Jiang, M., Ohnuma, I., Kainuma, R., and Ishida, K. (2005) Thermodynamic database of the phase diagrams in copper base alloy systems. *Journal of Physics and Chemistry of Solids*, **66**, 256 – 260.

Rue Archimède, 1 bte L6.11.01, 1348 Louvain-la-Neuve **www.uclouvain.be/epl**